SINGLE PIXEL HYPERSPECTRAL BIOLUMINESCENCE TOMOGRAPHY BASED ON COMPRESSIVE SENSING

by

ALEXANDER BENTLEY

A thesis submitted to

University of Birmingham

For the degree of

DOCTOR OF PHILOSOPHY

Physical Sciences for Health Doctoral Training Centre

College of Engineering and Physical Sciences

University of Birmingham

September 2021

ABSTRACT

Photonics based imaging is a widely utilised technique for the study of biological functions within pre-clinical studies. Specifically, bioluminescence imaging is a sensitive non-invasive and non-contact optical imaging technique that can detect distributed (biologically informative) visible and near-infrared activated light sources within tissue, providing information about tissue function. Compressive sensing (CS) is a method of signal processing that works on the basis that a signal or image can be compressed without important information being lost. This work outlines the development, testing and validation of a CS based hyperspectral Bioluminescence imaging system that is used to collect compressed fluence data from the external surface of an animal model, due to an internal source, providing lower acquisition times, higher spectral content and potentially better tomographic source localisation.

The work demonstrates that hyperspectral surface fluence images of both block and mouse shaped phantom due to internal light sources could be obtained at 30% of the acquisition time and measurements it would take to collect the data using conventional raster scanning methods. Using hyperspectral data, tomographic reconstruction of internal light sources can be carried out using any desired number of wavelengths and spectral bandwidth. Reconstructed images of internal light sources using four wavelengths as obtained through CS are presented showing a localisation error of ~3 mm. Additionally, tomographic images of dual-coloured sources demonstrating multi-wavelength light sources being recovered are presented further highlighting the benefits of the hyperspectral system for utilising multi-coloured biomarker applications.

Often it is the case where the optical parameters of the small animal are unknown leading to the use of a ‘best’ guess approach or to direct measurements using either a multi-modal or dedicated system. Using these conventional approaches, can lead to both inaccurate results and extending periods of imaging time. This work also introduces the development of an algorithm that is used to accurately localize the spatial light distribution from a bioluminescence source within a subject by simultaneously reconstructing both the underlying optical properties and source spatial distribution and intensity from the same set of surface measurements. Through its application in 2- and 3-dimensional, homogeneous and heterogenous numerical models, it is demonstrated that the proposed algorithm is capable of replicating results as compared to ‘gold’ standard where the absolute optical properties are known. Additionally, the algorithm has been applied to experimental data using a tissue mimicking block phantom and real bioluminescent mice models, recovering spatial light distributions that have localization errors of ~ 1 mm and intensities which are similar if not better than results gained using ‘gold’ standard methods without the need of assumptions regarding the underlying optical properties or source distribution.

ACKNOWLEDGEMENTS

I would firstly like to extend a massive thanks and appreciation to my lead supervisor, Professor Hamid Dehghani. His invaluable contributions to my work have not only led to this thesis, but also many other things such as the development of myself as a researcher. Without his dedication, patience, and knowledge I don't believe I would have made it through the first year of PhD, never mind arriving at this final step. I would also like to thank my second supervisor, Professor Jonathan Rowe, for his support, guidance, and advice throughout all aspects of my PhD project. I would like to thank the Physical Sciences for Health (Sci-Phy) CDT, including all of my colleagues, supervisors and lecturers over the entire four-year program, for their support and guidance.

I would like to send a thank you to my friends and colleagues within the Medical Imaging group, for making my time in the group at the University of Birmingham enjoyable and providing great mentorship and knowledge. A special mention goes to Ben Mellors who has helped from the first second of the program, from providing knowledge, to proof reading all of my work and just being a great friend.

I'd like to give thanks to Professor Ken Kang-Hsin Wang, Xiangkun Xu and Zijian Deng from the Department of Radiation Oncology at the University of Texas Southwestern, for providing me with the help and data that made the final part of my PhD project possible.

I would like to send a massive thanks to my family including my dad Lee and sisters Sara and Charlotte who have supported me through every aspect of my studies. A special mention will go to my mum Julie who has supported me through everything,

and also provided top-class proof-reading assistance. Also, I would like to thank all of my friends outside of university who have supported me throughout my life and have helped make me who I am today.

Finally, I'd like to extend my appreciation to my partner Hannah Spicer-Short who has stood by me through all of the ups and downs of my time at university and has helped and supported me whenever I needed it.

This work was funded by the Engineering and Physical Sciences Research Council as part of a studentship for the Physical Sciences for Health Centre for Doctoral Training (Grant number EP/L016346/1).

PUBLICATIONS ARISING FROM THIS WORK

Journal Papers

A novel hyperspectral bioluminescence imaging system based on compressive sensing was presented. The system was tested using multiple tissue mimicking optical phantoms to 'prove the concept' of the hyperspectral imaging system. This paper is the focus of Chapter 6 of this thesis.

Bentley, A., Rowe, J.E. and Dehghani, H., 2019. Single pixel hyperspectral bioluminescence tomography based on compressive sensing. *Biomedical optics express*, *10*(11), pp.5549-5564.

A novel dual-parameter reconstruction algorithm that can simultaneously recover bioluminescent source distributions and underlying optical parameters has been presented. This has been shown to work using both homogenous and heterogeneous mouse models as well as real data collected from a tissue mimicking phantom. This paper is the focus of chapter 7 of this thesis.

Bentley, A., Rowe, J.E. and Dehghani, H., 2020. Simultaneous diffuse optical and bioluminescence tomography to account for signal attenuation to improve source localization. *Biomedical Optics Express*, *11*(11), pp.6428-6444.

The novel dual-parameter reconstruction algorithm has been presented as applied to real murine tumour models, in collaboration with Professor Ken Kang-Hsin Wang and his research group at the university of Texas Southwestern. This paper is the focus of chapter 8 of this thesis. This journal paper has been submitted to the Journal of Biomedical Optics and as of submission of this thesis is currently under review.

Bentley, A., Xiangkun Xu, Zijian Deng, Rowe, J.E, Ken Kang-Hsin Wang ,Hamid Dehghani, 2021. Quantitative in-vivo Bioluminescence tomography**. Journal of Biomedical Optics** (Currently Under Review).

The theory of compressive sensing has been applied to the application of Spatial Frequency Domain Imaging. This papers lead author was Ben Mellors as part of the University of Birmingham's Medical Imaging Group. The theory in chapter 4 of this thesis underlines the basis of the presented work.

Mellors, B.O., Bentley, A., Spear, A.M., Howle, C.R. and Dehghani, H., 2020. Applications of compressive sensing in spatial frequency domain imaging. *Journal of biomedical optics*, *25*(11), p.112904.

Conference Proceedings

A novel hyperspectral bioluminescent imaging system based on compressive sensing was presented at the Photonics West conference in San Francisco in February 2019.

Bentley, A., Rowe, J. E., Dehghani, H., 2019, March. Compressive sensing based hyperspectral bioluminescence imaging, Proc. SPIE 10889, High-Speed Biomedical Imaging and Spectroscopy IV, 108891H

A novel hyperspectral bioluminescent imaging system based on compressive sensing was presented at the European Conference of Biomedical Optics in Munich in June 2019.

Bentley, A., Rowe, J.E. and Dehghani, H., 2019, June. Compressive Sensing Based Hyperspectral Bioluminescent Imaging. In *European Conference on Biomedical Optics* (p. 11074_23). Optical Society of America.

A cost effective novel hyperspectral bioluminescent imaging system based on compressive sensing was presented at the Biophotonics Congress: Biomedical Optics 2020 in Miami in February 2020.

Bentley, A., Rowe, J.E. and Dehghani, H., 2020, April. A Cost Effective and Low Footprint Hyperspectral Bioluminescent Tomography System Based on Compressive Sensing. In *Optical Tomography and Spectroscopy* (pp. STh3D-5). Optical Society of America.

A novel dual parameter reconstruction algorithm was presented at European Conference of Biomedical Optics in Munich in June 2021, in collaboration with Professor Ken Kang-Hsin Wang and his research group at the university of Texas Southwestern.

Bentley, A., Xiangkun Xu, Zijian Deng, Rowe, J.E, Ken Kang-Hsin Wang ,Hamid Dehghani, Simultaneous Diffuse Optical and Bioluminescence Tomography to Improve Source Localization. In *European Conference on Biomedical Optics* (To Be Published)

CONTENTS

LIST OF FIGURES

LIST OF TABLES

LIST OF ABREVIATIONS

ADMM – Alternating Direction Method of Multipliers

ATP – Adenosine Triphosphate

BB – Ball Bearing

BEM- Boundary Element Method

BLI – Bioluminescence Imaging

BLT – Bioluminescence Tomography

BOLD – Blood Oxygenation Level Dependant

CBCT – Cone Beam Computed Tomography

CBF – Cerebral Blood Flow

CCD – Charge Coupled Device

COM – Centre of Mass

CS – Compressive Sensing

CSCG – Compressive Sensing Conjugant Gradient

CT – Computed Tomography

cTHb – Concentration of Total Haemoglobin

CW – Continuous Wave

DMD – Digital Micro-Mirror Device

DOT – Diffuse Optical Tomography

DWT – Discrete Wavelet Transform

ECG – Electro-Cardiogram

FD – Finite Different

FEM – Finite Element Method

FISTA – Fast Iterative Shrinkage-Thresholding Algorithms

FLI – Fluorescence Imaging

fMRI – Functional Magnetic Resonance Imaging

FMT – Fluorescence Molecular Tomography

FWHM – Full Width Half Maximum

GBM – Glioblastoma Model

GFP – Green Fluorescent Protein

GN – Gauss Newton

GUI – Graphical User Interface

Hb – Deoxygenated Haemoglobin

HBO_2 – Oxygenated Haemoglobin

IRF – Instrument Response Function

MOSE – Molecular Optical Simulation Environment

MRI – Magnetic Resonance Imaging

MRS – Magnetic Resonance Spectroscopy

MSC – Mesenchymal Stem Cells

NIR – Near Infrared

NIRFAST – Near Infrared Fluorescence and Spectral Tomography

NMR – Nuclear Magnetic Resonance

NNLS – Non-Negative Least Squares

PAT – Photoacoustic Imaging/Tomography

PDAC – Pancreatic Ductal Adrenal Carcinoma

PET- Positron Emission Tomography

RIP – Restricted Isometry Property

SARRP – Small Animal Radiation Research Platform

SNR – Signal to Noise

SO_2 – Oxygen Saturation

SOCP – Second Order Cone Program

SPECT – Single Positron Emission Computed Tomography

TD – Time Domain

THb – Total Haemoglobin

TIF – Tagged Image Format

TOAST++ - Time-Resolved Optical Absorption and Scattering Tomography

TV – Total Variation

TVAL3 – Total Variation Minimisation by Augmented Lagrangian and Alternating Direction Algorithm

UCT – Ultrasound Computed Tomography

US - Ultrasound

CHAPTER 1

INTRODUCTION

Photonics based imaging is a widely utilised technique for the study of biological functions within pre-clinical studies. It is a highly sensitive and non-invasive technique that can detect distributed (biologically informative) visible and near-infrared light sources from, for example, luciferase-catalysed reactions (bioluminescence) or excited exogenous (fluorescent) molecules [1]. This allows for a non-invasive method of detecting and visualising functional activity within live intact animals. Bioluminescent imaging (BLI) has been shown to have the ability to track cells all around the body, including potential sanctuary sites such as the brain [2]. BLI has a number of advantages over fluorescence imaging (FLI), for example, in BLI there is no need for external excitation, the signal is generated directly by the luciferase-catalysed reactions. Also, within FLI there is auto-fluorescence present which leads to a background signal that is not present in BLI, allowing BLI to be used to image processes that produce minimal signal. An advantage that is shared by FLI, is that typically the signal is well localised (i.e., sparse).

BLI currently has many clinical uses for example in cardiac therapy, where bioluminescence can be used to track implanted cell behaviour [3]. BLI can also be used as a powerful tool to monitor gene expression in vivo as well as having potential to elucidate the pathobiology of lung disease including models of inflammation/injury, infection and cancer [4]. However, the most common application of BLI is in pre-clinical small animal studies, for example where bioluminescent molecules are used to infer

the size of tumours when investigating the effectiveness of anti-cancer drugs [5]. A review of different imaging techniques used in pre-clinical imaging is the subject of chapter 2 of this thesis.

The bioluminescent signal is produced by the reaction of the enzyme luciferase with the substrate luciferin in the presence of oxygen and adrenosine triphosphate (ATP) [6]. The light signal from the luciferase-catalysed reaction increases during the first minutes, reaching a plateau after 10 - 15 minutes and remains constant for around 40 minutes [7]. The characteristics of the bioluminescent signal therefore gives a safe timeframe for imaging within 20-30 minutes after the luciferin injection [8]. However, there are limitations to this method such as poor spatial resolution and weak signals and the underlying unknown tissue attenuation. Therefore, the quality and quantitative accuracy of the information that bioluminescent imaging provides can be affected by the difficulties in implementing it efficiently. Since bioluminescent signals are sparse and have very low intensities, highly sensitive spatially resolving detectors are required. Image reconstruction accuracy is also vastly improved through the collection of complete spectral data of the bioluminescent signal (~500-650nm), which means that data must be collected sequentially using different filters, increasing acquisition time. It is the cost of the imaging system and the length of data collection, together with a lack of quantitative analysis of signals that has acted as a barrier in the adoption of bioluminescent imaging. Therefore, there is a need to develop a novel system that can collect the full spectral data from a bioluminescent source, which can then be used to reconstruct the size and location of the source that is being imaged at both high speeds and low costs.

To allow the analysis from BLI to be more quantitative, methods that allow for the recovery of spatially resolved tomographic maps of the bioluminescent source location and intensity can be employed, known as Bioluminescent Tomography (BLT) [9]. In BLT, a 'forward' model of light propagation from the internal source to the surface of the subject, along with an optimization recovery 'inversion' algorithm are used to reconstruct the underlying source spatial and intensity distribution. There are several issues that arise with current BLT systems, including the non-uniqueness of single wavelength data [10]. To overcome this, multi-wavelength data of the emission at the surface of the subject due to the bioluminescence is collected by using spectrally resolved detection schemes such as bandpass filters, however this causes the time used to collect data to increase as data from individual wavelengths must be collected sequentially. Another issue is due to the effects of filter bandwidth on the quantitative accuracy of BLT [11], which has been shown to have dramatic effects on the reconstruction quality and is also often difficult to control due to the limited bandwidth of filters available. A final challenge to overcome is that most existing approaches only take into account the propagation of light from the light source to the surface of the subject and not from the surface of the subject to the optical detector. To address this, it is possible to either model the light propagation in free-space using ray-tracing techniques [12] or to utilise spectral derivative data [13]. Chapter 3 of this thesis introduces the theory behind imaging light through a diffuse medium and explores BLI and BLT in further detail.

Compressive or Compressed Sensing (CS) is a method of signal processing that works on the basis that a signal or image can be compressed under certain conditions (Chapter 4), without important information being lost. One of the most popular

techniques for image or signal compression that is currently used is ‘transform coding’. This technique finds the basis or domain of a signal that is sparse or compressible, meaning that a signal of length **n** can be represented by $\boldsymbol{k} \ll \boldsymbol{n}$ nonzero coefficients. A sparse signal can be represented with high accuracy by only keeping the values and locations of the largest coefficients of the signal. This is the basis of transform coding schemes such as JPEG, MPEG and MP3 [14]. By using this concept, it is possible to create a new framework for acquiring signals using highly efficient and cost-effective sensors. If a signal is sparse or compressible, it is possible to acquire a signal with fewer samples than is classically suggested within the Nyquist-Shannon sampling theorem, which states there needs to be a minimum number of measurements taken in order to perfectly capture an arbitrary signal [15]. In Compressive Sensing, rather than first sampling at a high spatial frequency and then compressing the collected data, it is possible to directly collect the compressed data. This enables a potentially massive reduction in the sampling and computational costs of measuring signals that are sparse [16].

There is currently a large body of research being carried out looking at the application of compressive sensing in imaging. A team of researchers at Rice University in Houston Texas presented an approach to building a simpler, smaller and cheaper alternative to a digital camera. This method uses technology to randomly sample an area using a single detector such as a photodiode or spectrometer. The scene is then recovered using a CS algorithm [17]. Compressive sensing is also being implemented into magnetic resonance imaging (MRI) by a team at Stanford University in California. This research is looking at vastly reducing the scan time by utilising the sparsity that is already present within MR images. This is done by under-sampling the

data and then performing reconstruction by minimising the l_1 norm of the transformed image [18]. CS is being used by the Institute for photonics and nanotechnologies in Milano to look at diffuse optical tomography (DOT) and fluorescence molecular tomography (FMT) where absorption/scattering or fluorescence properties respectively are being reconstructed. This research has shown that DOT and FMT can be improved by taking advantage of the properties of a single detector such as higher temporal resolution and larger spectral bandwidth, as well as having an improved acquisition speed compared to raster scanning [19]. The theory of compressive sensing and different recovery algorithms are discussed in chapter 4, as well as a review into several applications of CS.

In this work, a novel hyperspectral optical imaging system based on compressive sensing is presented. This system allows for the collection of hyperspectral data from the surface of a subject that can be used along with an accurate model (collected using a different modality) of the underlying optical properties of the subject to carry out BLT. The key aims of this work is to gain the ability to perform BLT with greater accuracy and efficiency through reductions in both imaging acquisition time and total costs involved, in turn making the BLT more accessible and with improved capabilities compared to traditional BLT, such as detecting multiple sources of different emission wavelengths simultaneously. The work presented in this thesis also presents the development of a dual-parameter reconstruction algorithm, which allows for BLT to be carried out without the need for a priori knowledge of any underlying optical properties. This will allow for further reductions in cost and imaging acquisition time, by not requiring the need for different imaging modalities to gain this information. The key steps of the algorithm development involved taking existing BLT and DOT

reconstruction algorithms and combining them to work together in an iterative method to recover global optical properties and localise bioluminescent sources simultaneously using the same set of surface measurements. This algorithm was tested on sets of simulated data, real phantom data collected with the developed imaging system and real murine data collected by Dr Ken Kang-Hsin Wang and his research group at the University of Texas Southwestern.

The key achievements of the presented work involve the successful design, development and testing of a hyperspectral bioluminescent imaging system based on compressed sensing. This also involved the development of system automation algorithms and the adaption of optimisation algorithms for recovery of signal from compressed data. The work presented led to a number of publications and conference proceedings that make up the latter parts of this thesis. Further achievements include the successful development of a dual-parameter recovery algorithm that was verified using multiple experiments, including simulated data from homogenous and heterogeneous models and real murine tumour models.

The research presented in this thesis will have a significant impact on both a national and international level. There has been a contribution to technology in this work that will potentially revolutionise the way biologically informative signals are measured. This work paves the way for the ability to image biological materials that have weak and sparse signals, such as mesenchymal stem cells (MSCs). Having this ability will bring advances in the understanding of the diseased body and will allow for technological advancements to address questions of the behaviour and fate of exogenous MSCs in animal models of liver tissue damage and hepatitis to a degree of accuracy better than those offered using traditional bioluminescence imaging. This work also addresses the

principals of the 3Rs (Replacement, Reduction and Refinement) that were developed over 50 years ago to provide a framework of more humane animal research. These are met by minimising the number of animals that are used during experiments due to it being a non-invasive technique. The length of time experiments are being carried out for can be refined due to the vast improvement that the technique developed can have on data acquisition time, directly leading to a reduction in animal suffering and improvement in animal welfare.

The structure of this thesis is as follows. The first three chapters present background information on all topics used in this work, in order to add context and motivation for the work carried out. Chapter 2 is a review of existing imaging modalities currently being utilised in pre-clinical studies, providing motivation for the need for the work presented in this thesis. This is then followed by a review of small animal tomography systems used, which adds further context and motivation to the work being carried out in this thesis. Chapter 3 then follows by discussing the theory behind imaging light through diffuse tissue, including the tissue-light interactions, models used in optical imaging, before introducing both DOT and BLT in further detail. Chapter 4 introduces the concept and theory behind compressive sensing, before describing several optimisation algorithms that are used in this work. A review of applications of compressive sensing is then presented. Chapter 5 presents the design and construction of the hyperspectral imaging system including optical components, structure and automation algorithms. The following three chapters show work presented in three journal papers that were written. The first is chapter 6 which presents a paper published in Biomedical Optics Express presenting the development and testing of the developed imaging system. Chapter 7 presents another paper that

was also published in Biomedical Optics Express, which presents the initial development and testing of the dual-parameter recovery algorithm. Chapter 8 shows work carried out in collaboration with the University of Texas Southwestern, which presents the application of the developed algorithm on real murine tumour models and shows the improvements to bioluminescent imaging that using the algorithm can provide. Finally, chapter 9 concludes the thesis.

CHAPTER 2

Pre-Clinical Imaging Modalities

2.1. Introduction

In biomedical science, the fundamental goal is to completely understand entire biological systems and processes, mainly the human body in both normal and abnormal conditions so that procedures and products such as drugs can be developed to treat the overall heath and combat any irregularities such as cancer. Often research and development using different imaging modalities are limited to the use of ex-vivo methods such as isolated cell cultures or tissue samples due to technical reasons such as penetration depth of imaging modalities. As well of this there are often ethical and safety barriers to the use of human subjects in trials such as unknown risk to health, or requires a procedure that would be damaging to the host.

Preclinical imaging is a methodology whereby the issues of human in-vivo imaging are addressed through the use of living animal models, usually small animals such as mice. The mouse model is a suitable analogue to a human model as many biological features such as organ structure, cellular processes and immune responses are shared. The use of mice also allows for longitudinal studies whereby the same subject can be monitored over a defined period of time to investigate and understand the impact of drugs and treatments such as those used in cancer therapy. It is because of this, along with the low costs and reduction of ethical and safety issues, preclinical imaging is now widely used to translate biomedical research from lab-based imaging techniques to human clinical trials.

This chapter introduces different imaging modalities that are currently used within preclinical imaging. Discussion of the principles behind each modality as well as any advantages or limitations they may have are presented. A comprehensive review of small-animal imaging systems is then carried out.

2.1.1. Magnetic Resonance Imaging (MRI)

Magnetic Resonance Imaging (MRI) is an imaging technique that arises from the utilisation of the Nuclear Magnetic Resonance (NMR) phenomenon. MRI is an extremely important method of medical imaging as it allows for the acquisition of detailed images of the anatomy of the body. The high spatial resolution and contrast that is present in MRI is extremely useful in differentiating between healthy and diseased tissue and providing important information on the condition of the skeleton and internal organs such as the brain. It is therefore very helpful for doctors to diagnose and decide on the best course of treatment for a patient [20]. Due to its high sensitivity and resolution, it is also extremely valuable in the area of pre-clinical molecular imaging [21-23]. There are also different variations of MRI that can be used such as Functional Magnetic Resonance Imaging (fMRI) and Magnetic Resonance Spectroscopy (MRS). These variations allow MRI to be useful in a much wider area of both medicine and biological research.

Within an MRI scanner, the signal from the nuclei of atoms and molecules are used to construct detailed images of the body. This signal arises from a phenomenon known as Nuclear Magnetic Resonance. NMR was first discovered by Isidor Rabi in 1937, his team working at New York City's Columbia University were measuring the magnetic properties of multiple nuclei including hydrogen and lithium. Rabi found that you could

flip the principle magnetic orientation of the nuclei by applying an oscillating magnetic field, for which he won the Nobel Prize for physics in 1944 [24].

MRI is an extremely useful and important technique that can be used to obtain structural images at extremely high spatial resolution with excellent tissue contrast. However, the high costs and space required to run and house an MR scanner often act as a major limitation to their use.

MRI can also be used to carry out functional and molecular imaging in the form of Functional Magnetic Resonance Imaging (fMRI) and Magnetic Resonance Spectroscopy. fMRI utilises two different consequences of increased neural activity, the first being increased local cerebral blood flow (CBF). This is done by injecting the subject with a contrast agent and carrying out a perfusion weighted scan, which uses a sequence of images and post processing to measure the flow of the agent within blood vessels in the body, with an increased flow directly relates to an increase in functional activity [25].

The second mechanism to measure functional activity is known as Blood Oxygenation Level Dependent (BOLD) contrast. This is one of the most commonly used methods in fMRI and works on the basis that the magnetic field around red blood cells changes subject to the oxygenation of the haemoglobin. When a haemoglobin is fully oxygenated it is diamagnetic and can be distinguished from other molecules. When deoxygenated the molecule is highly paramagnetic, which results in gradients in the magnetic field with a strength that depends on the concentration of haemoglobin [26, 27]. MRS can be used to carry out molecular imaging within tissue by taking advantage of the different magnetic field a particular proton is subject to due to nearby electrons. Protons within different sites experience different applied magnetic fields

and also resonate at different frequencies, therefore can be distinguished when analysing the data from an MRI scan [28].

2.1.2. X-Ray Computed Tomography (CT)

X-Ray Computed Tomography (CT) is an extremely useful and commonly used imaging modality in both clinical and pre-clinical settings [29-32]. CT is carried out by using a device such as an x-ray tube to generate x-rays that can be transmitted through the subject, to be collected on the other side by a device such as a scintillator. This is done from multiple different viewpoints to build up a series of 2D projections. From these projections algorithms (such as back-projection) can then be used to combine them into a 3D structural image of the subject. Contrast within the images is gained from the attenuation different tissues possess, for example bones attenuate x-rays much more strongly than soft tissue such as muscle. This leads to CT being of greater use in applications in imaging bone and hard tissue such as that found in arthritis studies [29]. It is possible to also image soft tissues with CT by incorporating contrast agents [30, 32], such as iodine-based agents [33, 34] and gold nano-particles [35, 36]. These agents are injected into the subject's blood stream prior to imaging and provides contrast to blood vessels and vasculature to allow for imaging of soft tissue such as organs and tumours. Functional CT can also be achieved through the use of contrast agents and by taking two scans, one before the contrast agent has been injected into the body and another after the contrast agent has reached equilibrium. By then carrying out a basic subtraction, a time-density curve of the contrast agent in the tissue can be found, which is used to give functional information about the tissue [37].

In pre-clinical studies the use of CT can provide structural images of animals with high spatial resolution of internal anatomy, however it is unable to provide any functional information. Another disadvantage for using CT is the high radiation doses that are given to the animal with each scan, which in turn could limit the longevity a study can be run on an individual animal. These high levels of radiation also become a problem for the safety of the human operator requiring significant radiation shielding to be in place. This along with the complexity of the x-ray sources, detectors and mechanical systems all add to high costs being involved.

2.1.3. Positron Emission Tomography (PET)

Positron Emission Tomography (PET) is another commonly used type of molecular imaging applied in both clinical and preclinical studies. When PET is carried out a tracer molecule containing a radioactive isotope is injected into the animal and will be distributed around the animal's vascular system. Through radioactive decay of the tracer molecule a positron is emitted, which after travelling a short distance (~0.5 mm) [38] will annihilate with an electron creating two gamma rays which travel in opposite directions at the speed of light. A detector such as a scintillator placed around the animal will be used to detect the two gamma rays and through the use of time of detection and ray tracing it is possible to locate the exact point at which the gamma rays are created. Throughout the imaging process many different annihilation events are detected, allowing for a 3D distribution of the tracer molecule throughout the body to be built [32, 38]. PET is limited to a resolution of on the order of ~1mm due to the nature of the radioactive decay, however can be used to provide quantitative functional information.

There are a number of advantages to using PET in pre-clinical studies, the first being the extremely high energy of the gamma ray emission. Due to these high energies there is a much lower chance of any tissue interactions when compared to other types of electromagnetic radiation (such as at optical wavelengths), making it much easier to locate the point of emission. This leads to another advantage whereby the sensitivity of imaging is purely limited to the efficiency and ability of the detector being used [39]. A further advantage is the field of view giving the ability to imaging the entire animal in one take, as the tracer will be distributed around the whole body and is highly transmissible [38]. An emission event has high specificity to a certain tracer due to the emission energy being measured, allowing for multiple different tracers to be used to measure different biological processes. There are a number of properties of the tracer molecule that can affect the sensitivity seen in the imaging. Tracer uptake, which can be affected by a number of factors, for example the physiological state of the animal and kinetics into and around the body can affect the sensitivity as well as the ability for the tracer to clear from the body [40]. An example of one of the most common tracers used is fluorodeoxyglucose (FDG) which can be indicative of metabolism within the body by taking the place of glucose .

Some limitations to imaging using PET arise from the availability of the tracer molecules. Due to the need to manufacture the radioisotopes used in the tracer molecules there is a need for a cyclotron to either be on site or close by. Further complications are added by this such as the cost involved and the time sensitivity of the tracer molecule due to the half-life of the radioactive isotope, meaning it has to be taken into account when considering the experiments being carried out. Another limitation to using PET is the high ionizing radiation dose that the subject receives from

the tracer molecules used, which can limit PET being used in long term studies. Due to the contrast gained from PET being entirely dependent on the tracer molecules, there is no structural information that can be gain from using it on its own. Therefore it is often used alongside other imaging modalities such as MRI or CT [38, 41], which can be used to provide clear anatomical information to use as a reference for PET. Both multi-modal imaging systems are commercially available however both come with their own limitations such as high costs.

2.1.4. Ultrasound (US) Imaging

Ultrasound (US) imaging is another commonly used modality of imaging in both clinical and pre-clinical settings. It uses high frequency mechanical (acoustic) waves to internally sample any tissue of interest. When US is used the acoustic waves propagate from the emitter through the animal and reflect back from any boundary of two areas with different acoustic impedance and are detected at the position of the US emitter. Using knowledge of the US waves and the speed of sound it is possible to calculate the exact distance between the acoustic boundary and the detector. Multiple measurements are taken and can be used to build 2D and 3D images of the animal where contrast is achieved through different acoustic boundaries. It is possible to gain further contrast in images through the use of contrast agents such as micro-bubbles [42, 43], which are introduced into the blood stream and act as a source of differing acoustic impedance. Another unique approach of US imaging is through Doppler US, which takes advantage of the doppler effect. As a wave reflects off an object that is moving, the wave is either compressed or stretched (which is measured as a change

in frequency) depending on the velocity of the object. This change in frequency is measured and the velocity of the object being measured can be inferred.

Advantages of US imaging include the use of non-ionizing radiation, therefore it is suitable for long-term studies. US imaging can also achieve fairly good resolution (<100 μm) whilst being very low cost as compared to other imaging modalities. Finally, US is unique when compared to other imaging techniques as it can be used to image in real time. The main disadvantage that arises from the use of US is in its contrast. As the underlying principle relies on gaining contrast from differing acoustic boundaries can limit its application. Contrast can be improved through the use of contrast agents, however contrast is generally quite poor [44-47].

2.1.5. Photoacoustic Imaging

Photoacoustic (PAT) imaging [46] is a hybrid imaging modality which takes advantage of optical absorption within tissue. The technology uses a pulsed laser to induce localized heating of molecules within the animal. This heating results in a rise of localized pressure and the associated rise in energy generates mechanical (acoustic) waves that can be detected as in ultrasound imaging. From the detection of these acoustic waves, it is possible to build a 3D pressure distribution across the animal being sampled using image reconstruction methods such as time-reversal approaches [48-50], which can then be used to infer the absorption of light that is occurring within the tissue.

The absorption that occurs within tissue by different chromophores is dependent on the wavelength of light being used to excite the molecules, leading to a number of benefits photoacoustic imaging can bring. Firstly, good image contrast can be gained

through the optical absorption of different chromophores within tissue. Due to the fact that the main absorbing chromophore in tissue is haemoglobin, this makes photoacoustic imaging a good option for visualizing vasculature for example when studying tumours and cancer [51-53]. Further to this, different absorbing agents can be used to improve the contrast gained when using this modality[54-56]. Because of the unique absorption characteristics of different chromophores, it is possible to use a multi-wavelength approach when imaging to differentiate between multiple chromophores [57-60]. As a similar detection method to ultrasound is used, high spatial resolution can be obtained. Finally, there is no ionizing radiation used in photoacoustic imaging therefore it is suitable for long term pre-clinical studies.

Disadvantages of using photoacoustic imaging arise from the cost associated due to the need of a high-powered pulsed laser system. Also due to the reason that photoacoustic imaging is a fairly novel method, fairly specialized expertise is required to run the systems, however the research and development being carried out, especially in high sensitivity detectors [61], is accelerating making it a much more useful tool. A final disadvantage of photoacoustic imaging is the limited penetration depth that is available, due to the highly attenuating properties of tissue at optical and near infrared wavelengths.

2.1.6. Fluorescence Imaging and Tomography (FLI/FMT)

Fluorescence Imaging (FLI) is an optical pre-clinical imaging technique, similar to bioluminescence, whereby light is generated within an animal or phantom and then measured externally at the boundary. Initially, the cells or area of interest are tagged with fluorescent molecules (fluorophores), which are then optically excited with a laser

through the process described in section 3.2.1. The emitted light is then measured at the surface of the animal/phantom with a camera. Due to the high absorption and scattering properties of biological tissue, the light measured at the surface is both weak and highly diffuse. This leads to poor image resolution and images only having an indirect indication (due to a large number of absorption and scattering events) of the exact position and fluorophore count of the source.

FLI can be extended to Fluorescence Molecular Tomography (FMT) whereby the interactions of light and tissue are modelled to build a 3D distribution of the fluorophores within the animal/phantom. By doing this it allows for much higher resolutions than achieved in standard FLI, whilst also gaining quantitative information about the fluorophore distribution. This allows for molecular imaging to be performed giving functional data comparable to that gained in many other imaging techniques such as PET. However, with FMT advantages are gained due to no ionizing radiation being used as well as much lower costs (system setup and running). Due to the large background of fluorescence being used in different areas of science such as microscopy, there is a vast abundance of fluorophores available for use. Some examples of widely used fluorophores include green fluorescent protein (GFP)[62] and Texas red [63]. Utilizing a fluorophore for in-vivo imaging will highly depend on its excitation and emission wavelength due to the optical window within tissue (section 3.1.1), making the most useful fluorophores those within the red and near infrared parts of the electromagnetic spectrum.

There are also a number of challenges that arise when using FLI or FMT such as background fluorescence, as described in section 3.1.2. It is possible to account for this background signal through different techniques such as spectral unmixing [64] and

fluorescence lifetime de-coupling [65], however using them will add further costs and time required when carrying out imaging. Another disadvantage is the process of photo-bleaching, whereby fluorophore emission depletes over time due to the excitation light, limiting the amount of time available for imaging in a study.

Modality	Advantages	Disadvantages
MRI	High Spatial Resolution Good Tissue Contrast Functional Imaging Molecular Imaging Non-Ionizing	Expensive
CT	High Spatial Resolution Functional Imaging	Expensive Ionizing Radiation
PET	High Energy, Good Resolution Image Whole Animal at Once	Tracer Uptake Tracers and Equipment Expensive No Structural Information Ionizing Radiation
US	Non-Ionizing Low Cost Real Time Imaging Fairly Good Resolution	Bad Contrast
PAT	Good Contrast Non-Ionizing Fairly Good Resolution	High Cost Very Specialist Limited Penetration Depth
FLI/FMT	Molecular/Functional Imaging Non-Ionizing Low Costs	Poor Resolution Background Fluorescence Photo-Bleaching

Table 2.1. The advantages and disadvantages of all pre-clinical imaging techniques described in this chapter.

2.2. Review of Small Animal Optical Tomography Systems

There has been a vast amount of research and development into the implementation of both BLT and DOT along with other pre-clinical imaging modalities into non-contact small animal imaging. This section will introduce different systems and the progression that has occurred with small animal optical tomography systems.

2.2.1. Basic BLT systems

One of the first BLT systems [66], referred to here as a basic BLT system, uses a highly sensitive CCD camera to obtain a single snapshot of the surface of the an animal, as shown in figure 2.1.

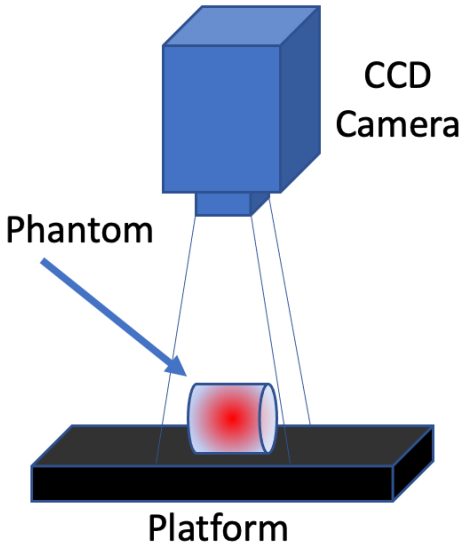

Figure 2.1. The basic BLT system using a CCD camera to take a single snapshot of the object of interest.

This system has been used extensively for research by multiple investigators [66-69]. Multiple views of the phantom are imaged using a rotating stage to move the camera around any axis. By doing this a dataset of single wavelength measurements from

multiple viewpoints is built, which then can be used to tomographically reconstruct the spatial light distribution within the phantom. This set-up is similar to that used in basic fluorescence tomography, with the addition of an excitation light source such as a laser [70-75]. Although this is a simple method of BLT and can provide good coverage of the entire phantom/animal being imaged, it brings a lot of limitations. Firstly, due to the low emission from a bioluminescent light source, it is required to use a large acquisition time (order of minutes) in order to gain enough SNR to obtain a useful measurement. This will then need to be repeated for each view point sequentially for the entire dataset to be built. Depending on the amount of viewpoints required, this approach can often be infeasible due to the time restrictions of the experiment when using bioluminescence. Another issue of the basic BLT setup is that the positioning of the phantom/animal is sometimes unnatural depending on the viewpoint required. This problem has been tackled through the use of a holding chamber, which holds the small animal in a set position and can be rotated about an axis [76-78]. By holding the animal in a set known position also allows for easier co-registration if any other imaging modalities are used. A further major limitation to the basic BLT system is the ill-posed nature of the problem, due to the number of unknowns being greater than the boundary measurements taken. This along with non-uniqueness (as described in section 3.5) makes reconstructing the spatial light distribution accurately using the basic system extremely difficult [10, 66].

2.2.2. Multi-spectral and Multi-view systems

In order to account for the issue of non-uniqueness whilst also increasing the number of measurements taken to reduce the ill-posed nature of the problem, systems have been developed to collect multi-spectral datasets [9, 10]. One of the first examples of a multi-spectral BLT system was developed by Kuo et al. [79] which incorporates a filter wheel into the basic single view-point BLT system, as shown in figure 2.2. This system works by sequentially collecting images using a CCD camera with a different wavelength colour filters in front of the lens. Whilst doing this improves the accuracy of reconstructions made, there is also a significant increase in time taken to collect the full data set due to the need to sequentially collect measurements with different filters. A benefit of using a filter wheel is that the phantom/animal will remain in the same position for each measurement, removing the need for any co-registration between measurements. The system presented by Kuo also included a laser galvanometer, with the purpose to scan the phantom/animal to provide surface geometry data.

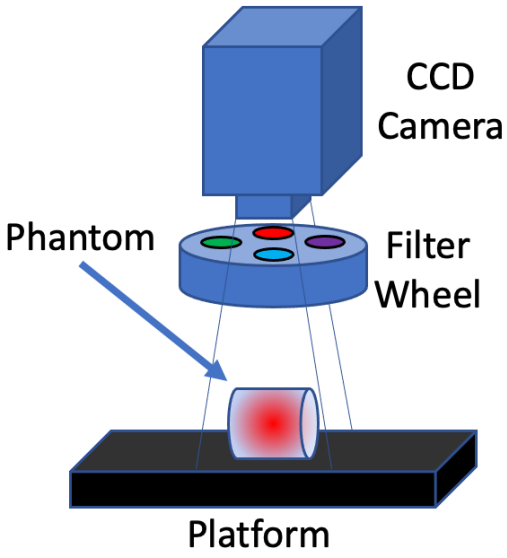

Figure 2.2. A single view BLT system that incorporates a filter wheel to provide multi-spectral data.

To reduce the amount of time taken when collecting data-sets requiring different view-points, the use of mirrors to allow for the acquisition of all the view-points required in one measurement has been presented. This was first proposed by Chaudhari et al. [80], whereby Kuo's multi-spectral system was adjusted to incorporate four 45^{o} mirrors to allow for the views of the top, bottom and sides of the phantom/animal to be measured simultaneously, as in figure 2.3. By doing this, the experimental time is dramatically reduced due to all views being collected simultaneously, at no significant increase in cost. One disadvantage is due to the focus of the different views being taken, which is caused by the different path lengths of light, however this is addressed by either taking multiple images at different focuses or through the use of modelling which will be discussed later.

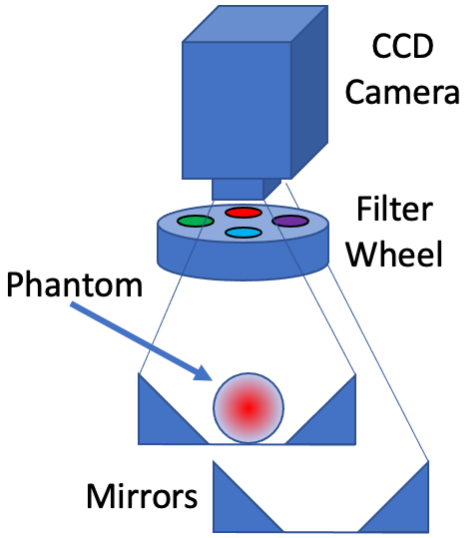

Figure 2.3. The multi-view, multi-spectral BLT system presented by Chaudhari et al. [80], which uses mirrors to collect multiple viewpoints simultaneously.

Another system that uses the same principle of mirrors to gain additional view-points simultaneously was presented by Li et al. [81], which uses conical mirrors to allow for a large amount of the surface of the phantom/animal to be measured in one image. This system also included two laser sources, one to be used for fluorescence excitation and the other to obtain geometry.

Wang et al. [82] presented a system which allows for the simultaneous collection of both multi-spectral and multi-view measurements. This is achieved through the use of mirrors as presented earlier to obtain multiple view-points, along with placing the animal in a multi-coloured holder. The holder is made up of three different coloured bands that act as light filters and are placed in a recurring pattern of evenly sized strips that cover the entire animal. Although this technique can reduce the time taken to collect a whole data-set, limitations arise. The technique is limited to a low number of wavelengths as adding more would reduce the coverage of the animal for a particular wavelength. This is already an issue as each individual wavelength filter doesn't give

complete coverage of the animal, however was shown to work well for three spectral bands. Wang et al. also presented a new method whereby a digital spectral separation device was used to collect multi-spectral data from single images [83].

2.2.3. Structural Imaging

When imaging using an optical tomography system, it is essential to have knowledge of the geometry of the animal being imaged in order to accurately reconstruct the underlying spatial light distribution. This knowledge is often gained through the use of secondary imaging modalities to directly measure the geometry of the animal directly, that can be used to build an accurate model to be used for reconstruction. It has also been shown multiple times that the use of accurate heterogeneous models of optical properties, gained through the use of different imaging modalities, can help improve the quality of BLT reconstructions [84-86].

One method that can be used to gain structural information, is to use a separate imaging device, such as MRI or CT [69, 76, 87]. There are number of benefits arising from obtaining the complimentary structural data, including the ability to segment the animal into regions of different optical properties through the use of published values. However, using a separate imaging device not only significantly raises the cost of the experiment, it also brings the need to co-register the two different images. This is not always easy to do, however can be made simpler through the use of a holder to ensure the animal is in the same position, as explained before.

Another method is to build a bespoke multi-modal system that uses different imaging modalities whilst the animal remains in the same position. This has been done by Liu et al. [84] whereby a dual BLT and CT system was developed. CT was also

incorporated into a number of different imaging systems that are used for FMT such as by, Schulz [88], Yang [89] and Kepshire et al. [90]. Although building such systems also incur large extra costs as with when using a separate device, by combining modalities it allows for the animal to remain in the same position throughout imaging, thus making the co-registration problem much simpler.

A cheaper and often easier method of collecting geometric information about the animal (however gaining less information than CT) is to use an optical surface capture method. In an FMT system that was developed by Deliolanis et al. [71] multiple projections of the animal are used to build a model of the surface geometry of the animal. This method increased both the time and complexity of the experiment due to the need to collect many different views of the animal. Other methods take advantage of structured light techniques [91] to directly capture the surface geometry of the animal. This was done by both Kuo et al. [79] and Basevi et al. [92], whereby sinusoidal structured patterns are projected onto the animal and used to reconstruct surface geometry. The latter is utilized by Guggenheim et al. [1] which uses multiple surface views simultaneously whilst also allowing for the reconstruction of surfaces that are visible in mirrors. This makes it possible for all structural data to be collected without the need to move the animal or imaging device during data collection.

2.2.4. Multi Modal Systems

Other than using secondary modalities to gain structural and geometric information about the animal being imaged, it is also possible to combine modalities to allow for the collection of data to add more scientific context to the study.

A system which utilizes single-photon emission computed spectroscopy (SPECT) and CT in conjunction with an optical imaging system was presented by Cao et al [93]. The optical system was capable of collecting data from bioluminescent and fluorescent sources, whilst CT was used to gain structural information. SPECT was used to collect data that was used as prior information to aid the BLT or FMT reconstructions. A similar idea was presented by Alexandrakis et al. [85], where an optical system is combined with PET. This system would utilize a cylindrical detector array that can simultaneously detect both visible and gamma radiation [94, 95]. Tennstaedt et al. [96] presented a combined MRI and BLI system to carry out non-invasive tracking of stem cells within the brain. The system takes advantage of MRI's high spatial resolution to be able to differentiate between different regions of the brain whilst also possibly offering the ability to carry out single cell imaging [97]. Photoacoustic imaging (PAT) has also been used alongside optical imaging, such as by Razanansky et al. [98], where FMT reconstructions were improved through measuring absorption with PAT. James et al. [99] presented a system that also utilizes PAT, along with fluorescence imaging and conventional ultrasound. Wang et al. [96, 97], presented a multi-modal system which incorporates cone-beam computed tomography (CBCT) to generate an anatomical mesh for BLT reconstructions. The system also includes a small animal radiation research platform (SARRP), which uses the BLT reconstructions for guided radiation therapy. The system has been verified using an orthotopic glioblastoma (GBM) model [100] and a subcutaneous and orthotopic pancreatic ductal adenocarcinoma (PDAC) model [101].

DOT has been used within a number of multi-modal systems as it has been shown to effectively obtain the underlying optical properties of the animal being imaged [86,

102, 103]. A simple single laser DOT system was incorporated into a basic BLT system by Zhang et al. [103], whilst a similar idea was presented by Tan et al. [104] for its use in a FMT system. DOT was used in conjunction with CT in a system presented by Pekar [105], whereby prior knowledge of the animals structure gained by the CT system was used to aid DOT. Yan et al. [106] presented a similar idea incorporating CT, DOT and BLT into a single system, however this uses a fully rotating gantry to allow for the multiple modalities to be used. DOT was combined with MRI by Gulsen et al. [107], who found that the use of MRI improved both the quantitative accuracy [108] and the resolution [109] of DOT. Guggenheim et al. [1] presented a multi-modal system which utilizes multi-spectral DOT to obtain optical parameters to guide reconstruction in BLT. This system uses a single CCD camera for all modalities to remove the need for co-registration, along with mirrors to gain multi-view data. Finally, Liu et al. [110] presented a pentamodal tomographic system that can perform PET, BLT, FMT, CT and Cherenkov luminescence tomography. Using this system allowed for anatomical, metabolic, viability and pharmacokinetic information to be obtained from a single animal. However, limitations to this system arise from the need to sequentially collect data from each modality due to different sources and detectors being used.

2.3. Conclusion

This chapter has introduced the current prominent imaging modalities that are used in pre-clinical trials, including the positives and negatives of each modality as show in table 2.1. These include much wider used, well-established modalities such as MRI

and X-ray CT, and much more recent emerging technologies such as photoacoustic imaging. This chapter has provided an overview of the pros and cons of the uses of each modality, which is often seen as a trade off between high sensitivity, resolution and cost. Whilst the focus of this work is targeted at Bioluminescence Imaging, this has provided an overview of other methods, giving clearer context to some of the reasons behind the choices made.

This chapter has also provided a review of the current state of small animal imaging systems with a focus on BLT. This ranges from basic camera based, single view and wavelength systems, to fully integrated multi-modal systems that have the ability to measure multi-spectral data, gain structural information and calculate underlying optical properties.

The following chapter introduces the theory behind imaging light through diffuse media (tissue) as well as delving further into bioluminescence and diffuse optical tomography. Methods of modelling the transport of light through diffuse media are discussed, and tools for simulating this transport are introduced.

CHAPTER 3

Theory of Models Used in Tissue Optics

Understanding the interactions of light within biological tissue is an essential part in performing functional imaging with optics of biological systems. It is also the key step in modelling the propagation of light within tissue for tomographic imaging reconstruction methods. This section will describe the main phenomena, absorption and scattering, that affect the propagation of light within tissue. This section will also discuss bioluminescence and fluorescence which are the main mechanisms behind the production of light within biological tissue that are used in optical imaging. How the transport of light through diffuse media is modelled is then discussed, followed by different methods of simulating this.

3.1. Interactions of Light and Tissue

3.1.1. Absorption

The absorption of light by molecules at visible to near infrared wavelengths is one of the main light-tissue interactions that can occur. This event is caused by a photon that contains the amount of energy required to raise an electron within a molecule from one energy state to another. This is known as ‘excitation’ and when it occurs, all of the photon energy is transferred to the electron and the photon ceases to exist. The electron will then remain in this excited state until the energy is lost through either heat-loss or further light emission (fluorescence or phosphorescence). Due to the energy states of electrons within molecules being in discrete values, it indicates that the

absorption of light by a molecule is dependent on the wavelength of the light, given by De Broglie's relation $E = \frac{hc}{\lambda}$, where E is the energy of the photon, h is the Planck constant, c is the speed of light and λ is the wavelength of the photon [111].

Light incident onto an absorbing only medium is related to the exiting light through the Lambert-Bouger law [112],

$$I(x) = I_0 e^{-\mu_a x} \quad (3.\ 1)$$

where, I_0 is the incident light intensity and $I(x)$ is the intensity of the light after it has travelled a distance of x through a medium with an absorption coefficient of μ_a. The absorption coefficient is a measure of the probability of a photon being absorbed per unit length [111], meaning that a higher the value of μ_a leads to a higher probability that the photon will be absorbed. The absorption coefficient is also highly dependent on the wavelength of light incident on the medium. At visible to near infrared (NIR) wavelengths (400nm-1100nm) the main absorbing agents within biological tissue are water, haemoglobin (Hb), melanin and lipids. The total absorption of a substance can also be calculated through the linear relationship known as the Beer-Lambert law, which is shown in equation 3.2.

$$A = \varepsilon l c \quad (3.\ 2)$$

Where, A the absorbance is the logarithm of the ratio between the incident and transmitted intensity of light. This is directly proportional as shown in equation 3.2 to the molar extinction coefficient ε, the molar concentration c and the optical path length l.

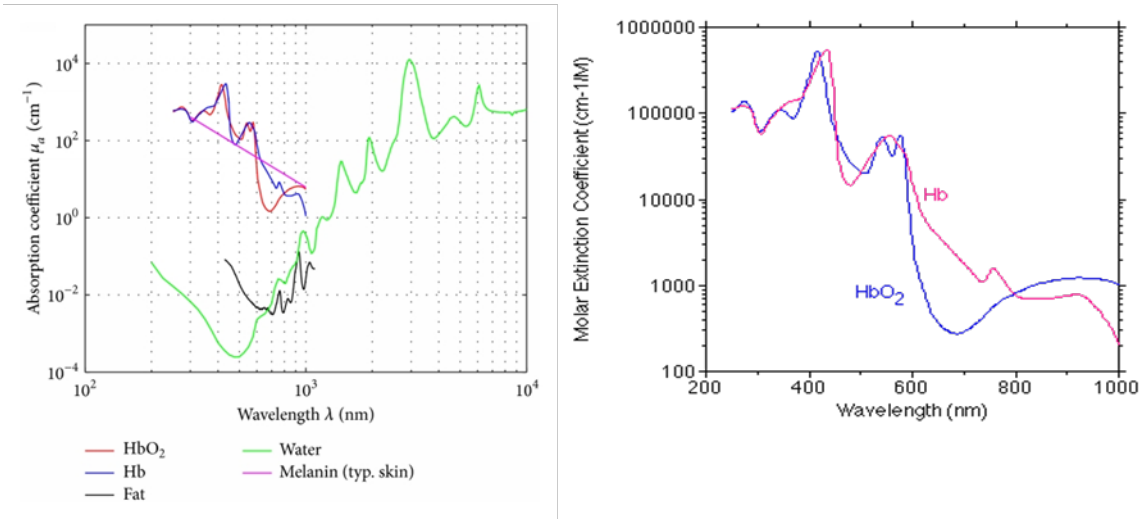

Figure 3.1. Absorption Coefficients Left: Absorption coefficient of chromophores found in biological tissue. Right: Absorption coefficients of oxygenated and deoxygenated haemoglobin.

Figure 3.1 shows the absorption spectra of the different absorbing agents found within biological tissue. As can be seen in the figure, at visible to near infrared wavelengths the absorption coefficient of water is vastly reduced as compared to haemoglobin and lipids. This gives a window of wavelengths where imaging using visible and near infrared wavelengths can be efficiently carried out due to the large amounts of water that makes up biological tissue. Oxygenated and deoxygenated haemoglobin are important absorbers as they are present in most biological tissues as well as being strong absorbers in the visible to near infrared wavelengths. They also act as a good target for both functional imaging and medical and biomedical observations. Due to them having slightly different absorbance spectra as seen in figure 3.1, if the molecular chromophores are known along with their absorption coefficients it is possible to solve a system of linear equations in order to calculate the exact concentrations of each chromophore from light measurements taken at different wavelengths [113].

3.1.2. Scattering

The second key interaction between light and a medium is scattering. This is defined as the event where a photon interacts with a molecule and changes direction without any energy being transferred. When the wavelength of the incident light closely matches with the size of the molecule it is interacting with, scattering occurs more strongly [111]. Just like absorption can be defined by the absorption coefficient, scattering can be defined by a similar value known as the scattering coefficient μ_s. This value is the probability per unit distance that a scattering event will occur whilst light is travelling through a scattering medium. The absorption coefficient in equation 3.1 can be replaced by the scattering coefficient:

$$I_b(x) = I_0 e^{-\mu_s x} \quad (3.\ 3)$$

where $I_b(x)$ is the ballistic transmitted light. The scattering properties of a medium are also defined by a scattering phase function, which describes the proportional scattered light as a function of angle [112]. This can be incorporated into the scattering coefficient through a value known as the anisotropy factor g, which is defined as the average of the cosine of the scattered light from an angular distribution. The values of g range from 1 which describes completely forward scattered light, through 0 which describes isotropic scattering, to -1 which describes completely back scattered light. The scattering coefficient is then changed into the reduced scattering coefficient such that:

$$\mu_s' = \mu_s(1 - g). \quad (3.\ 4)$$

If it is assumed that scattering events are independent, it is possible to define the reduced scattering coefficient using Mie theory by an empirical approximation given by,

$$\mu_s' = a\lambda^{-b} \quad (3.5)$$

Where a and b define the scatter amplitude S_A and scatter power S_P respectively, which are related to scatter particle sizes and density of scatters within a tissue [78].

3.2. Luminescence in Optical Imaging

3.2.1. Fluorescence

Fluorescence is a phenomenon that is often used as a source of light within optical imaging. It is the result of a three-stage process that occurs within molecules known as fluorophores or fluorescent dyes. The first stage is the excitation of the fluorescent molecule, which is often carried out using either a laser or an incandescent lamp. At this stage, energy hv_{EX} (where h is Planck's constant and v_{EX} is the frequency of the excitation photon) is transferred to the molecule which raises it from its ground singlet state S_0 into an excited singlet state S_1', which can be seen in figure 3.2 [114].

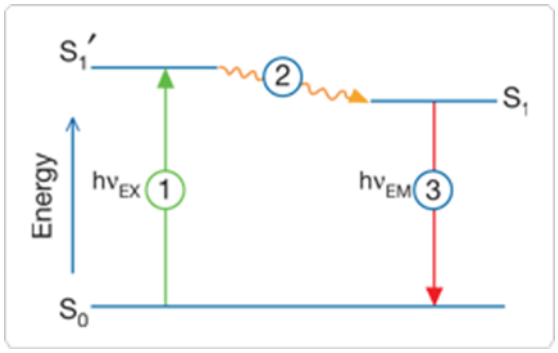

Figure 3.2. Jablonski diagram illustrating the processes involved in the creation of an excited electronic singlet state by optical absorption and subsequent emission of fluorescence. Image credit: [114].

This excited state exists for a short amount of time (1-10ns) during which the molecule is subject to a number of interactions with its molecular environment, such as internal heating. Through this stage of the process, the excited state S_1' is changed to a relaxed singlet excited state S_1 due to energy being partially dissipated. The final stage is the emission of a of a photon of energy hv_{EM} through returning the fluorophore back to its ground state S_0. Due to the effects of the second stage of the process, the energy of the emitted photon is of lower energy compared to the photon used to excite the molecule in stage 1. The difference between the energies of the exiting and emission photon is known as the Stokes shift, as seen in figure 3.3 [114].

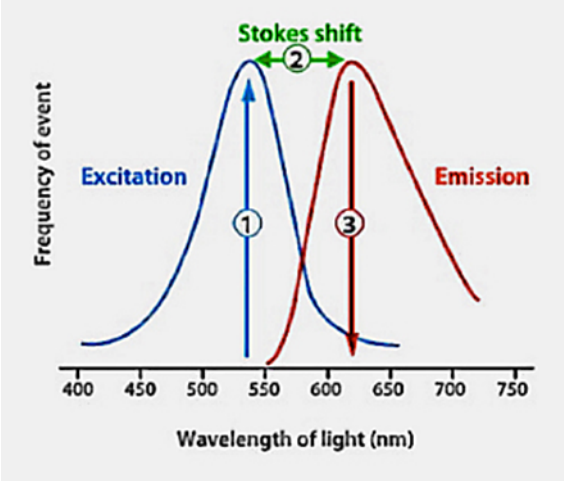

Figure 3.3. Demonstration of the difference in excitation and emission wavelengths known as Stokes shift. Image credit: [114].

Due to this Stokes shift, it is possible to detect the emitted photons against the excitation source and this is a fundamental part of why fluorescence techniques are sensitive.

The whole fluorescence cycle is repeatable, meaning that the same fluorophore can be excited and detected thousands of times unless it is destroyed through a process called photo-bleaching. Photo-bleaching is the irreversible destruction of a fluorophore which limits its detectability. It is caused by multiple photochemical reactions which occur under high-intensity illumination conditions, where a triplet excited state is created from the singlet state through a process called intersystem crossing [115].

Another issue that can arise with fluorescence optical imaging is background fluorescence. This is a background signal that is caused by either endogenous sample constituents (auto-fluorescence) or by unbound fluorescent probes. Background fluorescence can significantly compromise the quality of the data that is collected by reducing the signal-to-noise ratio detected. It can be minimised by using filters to block out the background, however this can lead to a decrease in the intensity of the signal

that is desired [116]. Within biological samples the main sources of auto-fluorescence are collagen and chlorophyll break-down products. Collagen is excited strongly by wavelengths between 300-350nm and emits strongly at 400nm [117] and chlorophyll break-down products excite strongly at 400nm and emit strongly at around 670nm [118]. Due to both of these molecules being found in skin, this is a significant source of auto-fluorescence [64].

3.2.2. Bioluminescence

Bioluminescence is a process similar to fluorescence by which photons are emitted from a molecule through the relaxation from an excited state to its ground state. Unlike fluorescence where the excitation is through the absorption of light, excitation is due to a biochemical reaction. The chemical reaction involves a pair of molecules known as a luciferase enzyme and a small molecule substrate. The reaction works in 3 stages, firstly the luciferase enzyme catalyses the conversion of the substrate, commonly luciferin, and Mg-ATP into luciferyl adenylate. This then reacts with local molecular oxygen to create an electronically excited intermediate. The final stage is the relaxation of this excited state to its ground state resulting in the emission of visible light [119].

When compared to fluorescence imaging, bioluminescent imaging has one main advantage due to the fact that there is no need for there to be an excitation light. This leads to there being no auto-fluorescence background and also no photo-bleaching effects, improving the signal to noise ratio and both specificity and sensitivity. The most common and widely used biomolecules are firefly luciferase (Fluc) and D-luciferin. The luciferase is incorporated into the subject that is being imaged and co-located to a specific process or structure. The luciferin is then injected into the subject prior to the

imaging and the reaction occurs as described above. There are many different bioluminescent agents that have been isolated from biological organisms and it can be shown that their peak emissions range from 490nm – 612nm, of which the higher limit belongs to Fluc [120]. It is important that there are molecules with peak emissions in the red bands of visible wavelengths because wavelength dependent light-tissue interactions limit signal the least within these bands. Because of this there is a wide popularity with using Fluc and also efforts to create molecules with red-shifted and high-power emissions [121].

3.3. Modelling Light Propagation in Tissue

In order to carry out in-vivo optical imaging of small animals, having accurate models of how light propagates throughout biological tissue is necessary. It is also just as important to have the tools available to be able to simulate this light propagation efficiently so that absorption and scattering can be accounted for and the correct solution can be obtained from the measurements collected.

3.3.1. Light Propagation

One method of modelling the propagation of light through biological tissue is to use the mathematical radiative transport equation [122, 123],

$$\frac{1}{c}\frac{\delta L(\boldsymbol{r},\hat{s},t)}{\delta t} = -\nabla . L(\boldsymbol{r},\hat{s},t)\hat{s} - \mu_t L(\boldsymbol{r},\hat{s},t) + \mu_s \int_{4\pi} L(\boldsymbol{r},\hat{s},t)P(\hat{s}\cdot\hat{s}')d\Omega' + Q(\boldsymbol{r},\hat{s},t) \quad (3.\ 6)$$

where L is the radiance, which describes the energy flow per unit area per unit solid angle per unit time. In this equation c is the speed of light, μ_t is the total interaction coefficient that incorporates both absorption and scattering $(\mu_a + \mu_s)$, P is the probability of scatter and Q is the energy of photon flux, all defined at position r at time t in direction $\hat{s}$. Derived using the conservation of energy, equation 3.6 is a differential equation that describes the rate of change of radiance at position r at time t in direction $\hat{s}$ on the left-hand side. There are four terms on the right-hand side of the equation that define the divergence of the radiance in a particular direction, the extinction of the radiance due to μ_t, the energy incident from a direction $\hat{s}'$ and scattered into $d\Omega'$ around direction $\hat{s}$ and finally the energy produced by a source. The radiative transport equation is a highly accurate method of modelling the transport of light throughout homogenous media, however it is also very complex, requiring a large amount of computational power to solve [124, 125]. One method of solving this is by using a method known as Monte Carlo, whereby individual photons paths are tracked [126]. If a sufficient amount of photons are tracked, it becomes representative of the radiative transport equation, however this also becomes computationally expensive. One method to make the problem more computationally viable is through the use of approximations [122, 127]. A method that is commonly used is to model the expansion of the source and radiance using spherical harmonics expansion, by using the first order (P_1) approximation of radiative transport equation. This gives rise to the diffusion approximation, which relies on a number of assumptions to allow it to be valid. The first assumption is that scattering within the medium dominates absorption and the second is that the light source used is isotropic, meaning the same in all directions. A time-dependent version of the diffusion approximation is as follows,

$$\frac{1}{c}\frac{\delta\phi(\boldsymbol{r},t)}{\delta t} + \mu_a\phi(\boldsymbol{r},t) - \nabla.[D\nabla\phi(\boldsymbol{r},t)] = S(\boldsymbol{r},t) \quad (3.\ 7)$$

where, ϕ is the fluence rate, S is the isotropic source and D is the diffusion coefficient which can be defined as,

$$D = \frac{1}{3(\mu_a+\mu_s')} \quad (3.\ 8)$$

The use of this approximation is significantly easier to solve compared to directly solving the radiative transport equation, however it is only an approximation so will not be as accurate. There are analytical solutions to the diffusion approximation available, that can be used to solve for certain geometries, such as homogenous infinite [128] or semi-infinite [129] mediums.

3.3.2. Simulating Light Propagation

Using models of light propagation in biological tissue such as the diffusion approximation presented in section 3.3.1. It is possible to accurately simulate this propagation. Due to the non-linearity of the light propagation with respect to the changing optical properties within tissue, it is only possible to obtain accurate results locally. Therefore, it is necessary to break the volume used for the model down into small sub-volumes whereby the optical properties are assumed to be constant so that the diffusion approximation can be solved individually to build a solution to the whole volume. There are a number of different methods that can be used, including finite element method (FEM) [130, 131], boundary element method (BEM) [132, 133] and finite difference (FD) [134]. If the volume being used is a simple shape or is considered

to be homogenous (constant optical properties), analytical models can be used to solve for the entire volume [79].

Within this work the FEM approach is used in all reconstructions carried out, where a geometrical accurate model of the small animal/phantom being imaged is used. This model is broken down into discrete tetrahedral elements, through which the vertices are known as nodes, allowing for complex heterogenous (spatially varying optical properties) geometries to be modelled effectively. There are currently several open-source software packages that utilize the FEM approach available, including Time-resolved Optical Absorption and Scattering Tomography (TOAST++) developed by Schweiger et al at UCL [135, 136]. Another toolbox available is the Molecular Optical Simulation Environment (MOSE), that was developed by Wang et al. at the Key Laboratory of Molecular Imaging in Beijing [137]. Finally, another open-source software package based on the FEM approach that is utilized in the work presented in this thesis is Near Infrared Fluorescence and Spectral Tomography (NIRFAST) which was developed by Dehghani et al. at the University of Dartmouth and University of Birmingham [130, 138, 139].

Using the NIRFAST package it is possible to simulate boundary data using modelled light source and optical property estimates. These simulations are used to compare with real measured boundary data in order to obtain objective functions for the optimization methods used in image reconstruction.

3.4. Diffuse Optical Tomography (DOT)

Diffuse Optical Tomography (DOT) is a modality of imaging that takes advantage of modelling light-tissue interactions in a similar way to BLT and FMT. In DOT light of

typically NIR wavelengths is injected into biological tissue from a known point [140, 141]. The light then travels through the tissue, undergoing absorption and scattering events (section 3.1), becoming diffuse and is then measured at set points across the surface of the animal/phantom, usually with a camera. From these measurements, along with knowledge of the animal/phantoms geometry, it is possible to tomographically build the spatial distribution of optical properties within the tissue. With the ability to model the optical properties recovered as a function of chromophore concentrations and scattering models, DOT can be used for functional imaging by recovering the approximate chromophore concentrations and scattering coefficients throughout the tissue being sampled. It is typical for the source of light to be placed on the outside of the animal/phantom, where if the source is on the same boundary as the detectors it is described as taking reflection measurements and transmission measurements if they are on opposite sides. There has been a vast amount of research carried out into applying DOT in health settings, where key areas are in the diagnostics of breast cancer in humans [127, 142-146] and functional imaging of cerebral activations [147-150]. DOT has also been applied to small animal imaging, which was addressed in section 2.2.

Within DOT there are three different modes of acquiring data; continuous wave (CW), frequency domain (FD) and time domain (TD). Firstly, when using CW, a constant input light such as a laser or lamp is used, for which the transmitted or reflected amplitude of exiting light is detected using a sensor such as a camera [130, 151, 152]. FD data collection uses sinusoidally amplitude-modulated light at frequencies typically around 100MHz [151]. Using FD allows for more information to be obtained through the collection of phase data [153, 154]. Finally, TD measurements

are carried out but using short light pulses from a laser, along with ultrafast detectors [135, 155]. TD can also give information for the probabilistic time of flight of photons, which can allow for scattering properties to be calculated. Due to the additional information that can be collected, it has been shown that FD measurements can give improved quantitative performance as compared to CW [137, 151]. However, CW requires much simpler sources and detectors as compared to FD and TD, allowing it to be both cheaper and require less complex analysis methods. Within this thesis any use of DOT will exclusively be using the CW method of data collection and analysis.

In order to reconstruct the spatial distribution of optical properties when carrying out DOT, an inverse problem is solved. This is done by minimizing the difference between the measured data, x, and data that has been modelled, which is known as the forward model, $F(\mu)$, at a given set of sources and detectors. The problem can be solved using a least squared type optimization given by the objective function,

$$\tilde{\mu} = \min_{\mu} \|x - F(\mu)\|_2^2 + \tau\|\mu\|_2^2 \qquad (3.\ 9)$$

where τ is a regularization parameter. This inverse problem is both highly ill-posed due to the non-linearity of the forward model and under-determined, which is a result of the large amounts of unknown variables. Due to these conditions it is implausible to solve accurately in one step, therefore an iterative reconstruction method is typically employed, such as where the gradient of the objective function is calculated [134, 156], or a Newton-like method such as a Levenberg-Marquardt procedure [157, 158], for which the latter is implemented into the algorithms used in this work. To implement this algorithm, an initial estimate of optical parameters, μ_0, typically using either prior

knowledge or a global fitting procedure [130]. From this the generalized Moore-Penrose pseudoinverse [159] is used to update the optical properties at each iteration, given by,

$$\delta\mu = (J^T J + \tau I)^{-1} J^T \delta x \qquad (3.\ 10)$$

where δx is the difference between the measured data and forward data and $\delta\mu$ is the update vector. In this example J is the sensitivity matrix, also known as the Jacobian, which defines the relationship between changes in measured boundary data and small changes in optical properties. This is calculated using an adjoint method [160], which takes advantage of the reciprocity that is present to efficiently construct the matrix from forward model fluence measurements. It has been shown previously that using the natural logarithm of the boundary intensity measured can significantly improve the quality of reconstructions as compared to using absolute values [161]. A modified Tikhonov (L_2) minimization scheme is used, which accounts for the ill-posed nature of the Hessian $J^T J$ by stabilizing the update [162] resulting in a smoother solution. Alternate regularization schemes have been investigated for their application in DOT [163], whereby L_1-norm minimization is applied. Doing this has been shown to outperform Tikhonov regularization consistently through its ability to preserve edges in images and robustness against noise. It is however harder to implement, with the need for more complex algorithms such as the alternating direction method of multipliers (ADMM) or fast iterative shrinkage-thresholding algorithms (FISTA).

When carrying out DOT using a single wavelength, it is only possible to obtain maps for the absorption coefficients μ_a or scattering coefficients μ_s'. If data is collected

and coefficients are recovered at multiple different wavelengths, it is possible to use the Beer-Lambert law (Equation 3.2) to recover for chromophore concentrations [164] and scattering power S_P and amplitude S_A through Mie scattering theory (Equation 3.5) [78]. Through this method any small errors in μ_a and μ_s' will propagate and be amplified when calculating the chromophore concentrations, S_P and S_A [164]. Instead, it is possible to constrain the problem spectrally by incorporating them directly into the reconstructions. This is done by changing the jacobian to relate to a small change in chromophore concentrations, S_P and S_A, instead of optical properties. Doing this reduces the number of unknowns from 2 per wavelength, to the number of parameter images required, usually 5 [140, 143, 165]. Doing this has been shown to improve reconstruction quality [164], whilst providing functional information. One example is by recovering concentrations of haemoglobin (HbO_2) and de-oxyhaemoglobin (Hb) to allow for functionally relevant information such as total haemoglobin concentration (tHb) and tissue oxygen saturation (SO_2) to be calculated.

3.5. Bioluminescence Imaging and Tomography (BLI/BLT)

Bioluminescent (BLI) Imaging is a widely used imaging modality within pre-clinical biomedical studies. It is a highly sensitive and non-invasive technique that can detect distributed biological visible and near-infrared light sources from luciferase-catalysed reactions [166]. This allows for a non-invasive method of detecting and visualising functional activity within live intact animals. Bioluminescent imaging has been shown to have the ability to track cells all around the body, including potential sanctuary sites such as the brain [2]. The light signal from the luciferase-catalysed reaction increases during the first minutes, reaching a plateau after 10 to 15 minutes, after which the signal

remains fairly constant for around 40 minutes [7]. The characteristics of the bioluminescent signal therefore gives a safe timeframe for imaging within 20-30 minutes after the luciferin injection [8]. Limitations to this method include poor spatial resolution and the quality of the information that bioluminescent imaging can provide can be affected by the difficulties in implementing it efficiently. Since bioluminescent signals have very low intensities, highly-sensitive spatially resolving detectors are required. Image reconstruction accuracy is also vastly improved through the collection of complete spectral data of the bioluminescent signal, which means that data must be collected multiple times using different filters, increasing acquisition time.

Bioluminescent tomography (BLT) is a further step on from BLI, where the aim is to reconstruct the internal light source distribution within the subject that is being imaged. This method was first proposed by Wang et al in 2003 [66] and can bring many advantages to pre-clinical imaging as bioluminescent light sources used are co-localised with features of interest such as tumours [167]. Images taken at the surface of the subject, as well as knowledge of the source and optical properties, image reconstruction can be carried out using different methods such as finite element methods (FEM) or boundary element methods (BEM). This reconstruct method uses a least-squares minimisation,

$$b = \min_{b} \|y - F(b)\|_2^2 \qquad (3.\ 11)$$

where b is the desired internal light distribution, F is the model that accounts for the optical properties and geometry and y is the boundary data that is measured. An example of open source FEM-based light modelling software is Near Infrared

Fluorescence and Spectral Tomography (NIRFAST) [130, 139], developed by Dehghani et al. Due to the relationship between the light measured at the boundary and the source intensity being linear, it is possible to describe the two through a single matrix known as the Jacobian (defined in section 3.4). In a practical real world experiment, there is typically many more unknown internal nodes than boundary measurements made, leading to a number of problems as it is both mathematically ill-posed and ill-conditioned [9, 168]. Another major issue that arises from this problem is that no matter however many observations are made the problem is mathematically non-unique, which is illustrated in figure 3.4.

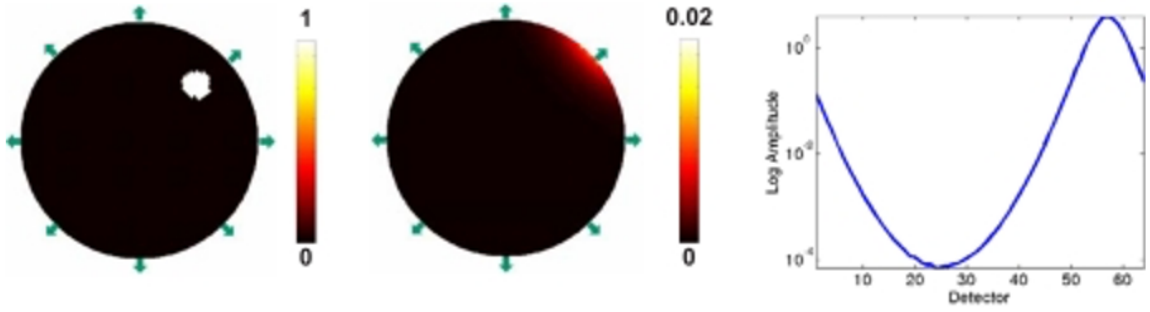

(a) (b) (c)

Figure 3.4. A demonstration of the non-uniqueness that arises from the problem of bioluminescence tomography. (a) and (b) represent two different internal light sources that give rise to exactly the same boundary data (c). This figure has been replicated from Dehghani et al. [9].

The issue of non-uniqueness can be addressed through the acquisition of the boundary data at multiple different wavelengths [9, 10, 79, 168, 169]. This is due to the fact that the optical properties of tissue are related to the wavelength of light, meaning that light at one wavelength will take a different path compared to a different wavelength. Using this method will not completely negate the effect of non-uniqueness,

however through the use of different optimisation algorithms it is possible to work past this.

Chapter 4 of this thesis will introduce different optimisation algorithms that can be used in BLT, whilst chapters 6, 7 and 8 will show the application of BLT. BLT has been applied to small animal imaging, which was explored further in section 2.2.

3.6. Conclusion

This chapter has introduced the key principles describing the phenomena that occur when light travels through diffuse media such as biological tissue. This is the fundamental theory that governs the basis of how BLT and DOT is possible. Both the imaging techniques of BLT and DOT have been initially introduced and will be used in the work presented in this thesis. Key interactions that result in the emission of light, bioluminescence, and fluorescence, have also been discussed. Methods of modelling the transport of light through the use of the diffusion approximation of the radiative transport equation has been introduced, as well as how this is utilized within tools that can simulate the path of light through diffuse media.

The following chapter introduces the theory of compressive sensing which is the basis behind the novel imaging system that is presented in this work. This is followed by the presentation of different optimisation algorithms that are utilised. The chapter ends with a review of current applications of compressive sensing within imaging.

CHAPTER 4

COMPRESSIVE SENSING THEORY

This chapter introduces the theory of Compressive Sensing (CS) and introduces a number of different reconstruction algorithms that can be used to aid in obtaining signals and images from compressed data. This is an important theory that makes up the basis of the hyperspectral imaging system presented in this thesis. First the background theory of CS is discussed before different types of reconstruction methods and algorithms are introduced. The chapter closes with a review of current applications of CS to imaging modalities that can be used in both clinical and pre-clinical studies. There is huge motivation to apply CS to BLI and BLT as it gives the potential to reduce both the costs and time associated with collecting data. It also adds the ability for hyperspectral data collection and paves the way for additional functionality, which will be discussed in more detail later in this thesis.

4.1. Theory

4.1.1. Overview and Sparsity

Compressive or Compressed Sensing is a signal processing technique that utilises the sparse nature of real-world signals in order for them to be compressed either in it original domain or in some transform domain. It works in a similar way to standard transform coding and image/signal compression algorithms such as JPEG-2000, where the data vector which represents the raw pixels of the image is transformed using the discrete wavelet transform (DWT). Once the image has been transformed all

of the small wavelet coefficients are set to zero leaving behind a sequence that can be stored efficiently and when required later can be inverse-transformed to provide an approximate representation of the original image or signal [14]. This technique finds the basis or domain of a signal that is sparse or compressible, meaning that a signal of length n can be represented by $k \ll n$ nonzero coefficients. A sparse signal can be represented with high accuracy by only keeping the values and locations of the largest coefficients of the signal.

Using the ideas of transform coding, it is possible to create a new framework for both acquiring signals and how sensors are designed. If a signal is sparse or compressible, it is possible to acquire a signal with less samples than is classically suggested within the Nyquist-Shannon sampling theorem, which states there needs to be a minimum number of measurements taken in order to perfectly capture an arbitrary signal [15]. When collecting analogue signals the Nyquist-Shannon sampling theorem states that the sampling frequency must be at least twice the highest frequency present in the data. Expanding this to 2D digital image capture, the theorem states that any spatial image frequency components that are above the Nyquist frequency of the sensor, which is defined as one half of the reciprocal of the centre-to-centre pixel spacing, cannot be accurately reproduced by the sensor [170, 171]. In Compressive Sensing, rather than first sampling at a high rate and then compressing the collected data, it is possible to directly collect the compressed data. This enables a potentially massive reduction in the sampling and computational costs of measuring signals that are sparse [172].

By considering an $N \times 1$ signal x, that is real-valued, finite-length and one-dimensional, it is possible to represent this basis of $N \times 1$ vectors $\{\varphi_i\}_{i=1}^{N}$ expressed as,

$$x = \sum_{i=1}^{N} s_i \varphi_i = \varphi s \qquad (4.\ 1)$$

where s is an $N \times 1$ column vector of weighting coefficients. The signal x is defined as K-sparse if only K of the s_i coefficients are nonzero, and if $K << N$ the signal is compressible. In order to directly capture the compressed signal, $M < N$ linear measurements are taken of the inner products of x and a collection of vectors $\{\phi_j\}_{j=1}^{M}$ such that $y_j = \langle x, \phi_j \rangle$. Arranging y_j into a $M \times 1$ vector y, ϕ_j as rows in an $M \times N$ matrix ϕ and substituting in x from equation 4.1, y can be written as,

$$y = \phi x = \phi \varphi s = \Theta s \qquad (4.\ 2)$$

where Θ is an $M \times N$ matrix. If the measurements y are collected for a certain measurement matrix ϕ, there are two problems that need to be overcome in order to accurately obtain the signal x. Firstly, the measurement matrix needs to be designed so that important information within the signal is not lost by the dimensionality reduction from N to M measurements. Secondly, a reconstruction algorithm needs to be designed so that it can correctly recover the signal x from only M measurements [173].

In order to design a system that can acquire signals using a compressive sensing method, first a suitable measurement matrix needs to be designed so that the signal can be reconstructed from $M < N$ measurements. This problem can be solved if the signal is K-sparse given that $M \geq K$. A condition that has to be met in order for the problem to be well conditioned is the restricted isometry property (RIP). This states

that for any vector v that has the same K nonzero entries as x and some $\epsilon > 0$, it must satisfy the inequality,

$$1 - \epsilon \leq \frac{\|\Theta v\|_2}{\|v\|_2} \leq 1 + \epsilon \qquad (4.\ 3)$$

Which implies that matrix Θ must preserve the length of these particular K-sparse vectors v. A sufficient condition for a stable solution for compressible signals is that matrix Θ satisfies equation 4.3 for an arbitrary $3K$-sparse vector[174]. Another condition that has to be met with the measurement matrix is incoherence, meaning that the rows of ϕ cannot sparsely represent the columns of φ. Both the RIP and incoherence conditions are met with high probability if the measurement matrix is formed of independent and identically distributed (iid) random variables from a Bernoulli distribution, with probability $p = 0.5$ [175]. A Bernoulli distribution is defined as a discrete probability distribution of a random variable with probabilities $[P(x = 1) = p; P(x = 0) = 1 - p]$. This results in y simply being M randomly weighted linear combinations of the signal x. By using a random Bernoulli measurement matrix there arises two properties that are useful in the application of Compressive Sensing. Firstly, the matrix is incoherent and has the RIP with high probability if,

$$M \geq cK\, log\left(\frac{N}{K}\right) \qquad (4.\ 4)$$

where c is a constant. This means that a K-sparse signal can be exactly reconstructed with M measurements as specified in equation 4.4. The second property is that the

matrix ϕ will have the RIP with high probability regardless of what the orthonormal basis φ is chosen to be.

4.1.2. L_1 Minimisation

The next step in creating a system to utilise Compressive Sensing is to design a suitable reconstruction algorithm. This algorithm needs to be able to find the solution to equation 4.2 that represents the signal x exactly given the random matrix ϕ, the basis matrix φ and the M measurements within the vector y. As $M < N$ the system is referred to as underdetermined, which means that there is an infinite amount of solutions that satisfy equation 4.2. In order to find the correct solution, the algorithm will need to find the signals sparse coefficient vector [174]. One method to find the correct solution is to minimize certain variations of the l_p norm of the vector s, which is defined as,

$$\left(\|s\|_p\right)^p = \sum_{i=1}^{N} |s_i|^p \qquad (4.5)$$

The classical approach to solving this problem is to minimise the L_2 norm (energy) of vector s by solving,

$$\hat{s} = argmin\|s'\|_2 \;\; such\ that \;\; \Theta s' = y \qquad (4.6)$$

This method also referred to as L_2 regularised least squares and has a simple closed form solution, however this method almost never finds a $K-$sparse solution and often

returns a nonsparse solution with many nonzero values. The reason for this is shown in figure 4.1. Another approach to this problem is to find the solution that has a minimum L_0 norm. The L_0 norm finds the sum of the zeroth power of the values within vector s therefore finds the sparseness of the solution. The equation that has to be solved in this case is,

$$\hat{s} = argmin\|s'\|_0 \quad such\ that\ \ \Theta s' = y \tag{4. 7}$$

and will find the K-sparse solution exactly [176]. However, solving this is both numerically unstable and NP- hard, meaning that is it near impossible to find the correct solution without exhaustive enumeration of all of the nonzero values in s. The final method of finding the correct solution to equation 4.2 is to minimise the L_1 norm of s by solving,

$$\hat{s} = argmin\|s'\|_1 \quad such\ that\ \ \Theta s' = y \tag{4. 8}$$

Solving equation 4.8 recovers the exact K-sparse solution and can closely recover compressible solutions meeting the condition specified in equation 4.4 [177]. This problem often reduces to a linear program known as basis pursuit that has a reasonable amount of computational complexity, however with current advances in technology it is a problem that can easily be solved. An example of this is the In-crowd algorithm, which solves basis pursuit denoising by minimising sub-problems iteratively [178].

It is much easier to visualise why reconstructing the signal by using the L_2 norm fails, whilst reconstructing with the L_1 norm doesn't by looking at the geometry of both norms along with the null space for s. Figure 4.1 shows the unit balls of both the L_1 and L_2 norms in two dimensions along with the null space that represents equation 4.2. In the visual representation of the two different norm minimisations, the line labelled $\mathcal{H}_0$ is the null space that represents equation 4.2, for which the gradient is determined by the measurement matrix and is therefore random. The L_2 minimiser finds the point on $\mathcal{H}_0$ which is closest to the origin, which is found by increasing the size of the L_2 unit ball until it touches $\mathcal{H}_0$. Due to the randomness of $\mathcal{H}_0$ the point $\hat{s}$ will most likely lie away from the coordinate axes and therefore give a non-sparse value. Whereas, the L_1 unit ball has points that align with the coordinate axes so when the L_1 norm is increased it will make first contact with $\mathcal{H}_0$ near the axes and will give the exact sparse solution to equation 4.2 [173].

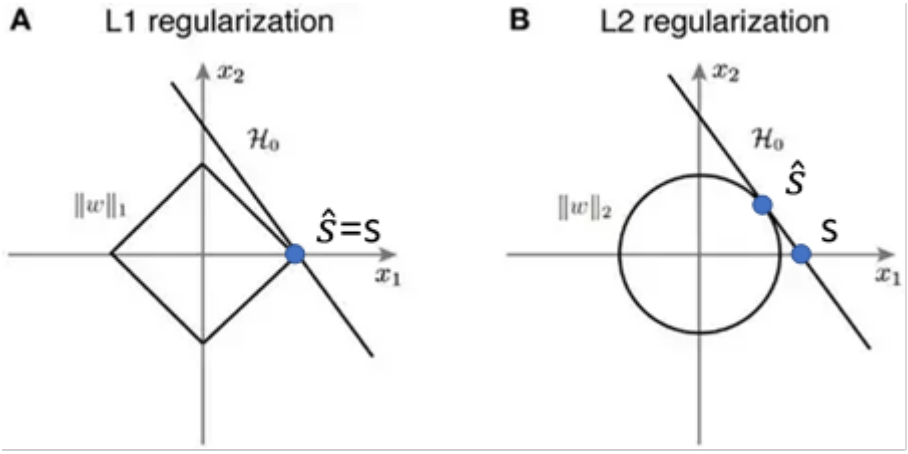

Figure 4.1. Visualisation of the L_1 and L_2 norm (A) Visualisation of the L_1 norm minimisation that finds the sparse solution. (B) Visualisation of the L_2 norm minimisation that finds a non-sparse solution. Image credit:[179]

4.1.3. TV Minimisation

In order the find the solution of an underdetermined problem, it is assumed that the signal is sparse in some basis. If it is assumed that instead of the signal being sparse, the gradient of the underlying signal or image is sparse, it is possible to recover the signal by minimising the total variation (TV) of the signal instead of the L_1 -norm. Using TV-regularisation over L_1 -regularisation can result in reconstructed images being sharper due to the edges and boundaries being preserved more accurately. TV regularisation has been used extensively since its introduction in 1992 by Rudin, Osher and Fatemi for its use in image denoising [180]. Since then it has been used in many other applications such as image deconvolution [181] and image restoration [182]. One issue with TV regularisation is that the properties of non-differentiability and non-linearity make it much more computationally difficult than L_1 -norm regularisation. This leads to the need of efficient algorithms that can be used to reduce the processing time that it takes to find a solution to the problem. To tackle this problem German and Yang began by proposing the idea of a joint minimization method to solve a variant of TV model known as half-quadratic models [183, 184]. Following on from using half-quadratic models, in 2008, Wang, Yang, Yin and Zhang successfully applied TV minimization to deconvolution and denoising problems [185], which was then extended into multichannel image reconstruction, deblurring and denoising [186-188]. Whilst the reconstruction algorithm was both effective and efficient, a restriction arises from the need to use the partial Fourier matrix as the measurement matrix. This restriction has been investigated by Chambolle in 2004 and displayed linear convergence through the use of iterative algorithms [189]. Through the use of this type of algorithm, TV

regularization was applied to denoising and image reconstruction problems whilst using an orthogonal measurement matrix.

Through the development of TV algorithms they were shown to be extremely powerful tools in a number of applications including image reconstruction and edge detection. However, when compared to algorithms which used L_1 minimization schemes, they were shown to be both slower and less robust. These difficulties were overcome by Li in 2009 through the development of a new TV minimisation algorithm (TVAL3) which was shown to be more robust through the ability to use many different measurement matrices, whilst also being as fast as most L_1 minimisation algorithms [190].

4.2. Algorithms

There are a number of open source CS reconstruction algorithms that are currently available to be used and adapted for different CS applications. The majority of these algorithms use L_1 minimisation in order to find a solution to the problem. This next section will describe different algorithms that can be used.

4.2.1. L1 Magic

L1-Magic is a MATLAB based package that contains scripts that can be applied to a number of different cases where there are different constraints or different classes the problem can be cast into. It was developed by Emmanuel Candes and Justin Romberg at Caltech in 2005 as a proof of concept showing that recovery procedures are computationally tractable for both small and large scale problems where there may be

millions of data points [191]. There are two main algorithms that are used within this package; the first is for when the problem can be recast as a linear program. In this case a generic path-following primal-dual method is used in order to find the solution to equation 4.2. A primal-dual algorithm works by re-writing the problem as a system of non-linear equations known as the Karush-Kuhn-Tucker conditions:

$$
\begin{aligned}
&(KKT) \quad c_0 + A_0^T v^* + \textstyle\sum_i \lambda_i^* c_i = 0, \\
&\lambda_i^* f_i(z^*) = 0, \;\; i = 1, \dots, m, \\
&A_0 z^* = b, \\
&f_i(z^*) \leq 0, \;\; i = 1, \dots, m.
\end{aligned}
\qquad (4.\ 9)
$$

Where, c is a constant, z and b are search vectors, A is a matrix. At the optimal point z^* there will exist dual vectors v^* and λ^* where the KKT conditions are met. The algorithm solves these equations by using a classical Newton method, where at an interior point (z^k, v^k, λ^k) the system is linearised and solved. The step to the new point $(z^{k+1}, v^{k+1}, \lambda^{k+1})$ is then modified so that the system remains in the interior. The primal-dual algorithm repeats the Newton iterations until a set value η known as the surrogate duality gap which is an approximation of how close a certain (z, v, λ) is to being optimal, has decreased below a set tolerance [192].

The second algorithm is for when the problem can be re-cast as a second-order cone program (SOCP). This algorithm uses a log-barrier method to solve the problem, by transforming equation 4.8 into a series of linearly constrained programs:

$$\min_{z} \langle c_0, z \rangle + \frac{1}{\tau^k} \sum_i -log\,(-f_i(z)) \quad subject\ to \quad A_0 z = b, \tag{4. 10}$$

This algorithm works my first inputting a starting point z^0 and a tolerance η. Equation 4.10 is then solved using Newton's method, which terminates once the duality gap, m/τ^k is below a set tolerance. It can be shown that as τ^k gets large the solution z^k approaches the optimal solution z^*, therefore the solution will be within the duality gap of the optimal solution at iteration k. If the solution does not reach within the duality gap, the solution z^k is set as the new starting solution and then a new log-barrier iteration begins, continuing in the same way as before with further Newton iterations. This process continues until the optimal solution is found [192].

4.2.2. TVAL3

The total variation minimisation by augmented Lagrangian and alternating direction algorithm (TVAL3) is a TV minimisation algorithm developed by Chengbo Li at the Department of CAAM, Rice University in Houston. This algorithm works by combining a classic augmented Lagrangian method with an appropriate variable splitting and nonmonotone alternating direction method. This is done by rewriting the minimisation problem as an alternative problem known as augmented Lagrangian function. An iterative method is then used to implement this function by finding minimising parameters by means of an alternating direction algorithm [190].

The TVAL3 scheme begins by taking the standard compressive sensing problem whilst replacing the L_1 norm term with the term for total variation,

$$\min_{w_i,u} \sum_i \|w_i\|, \ s.t. \ Au = b \ and \ w_i = D_i u \qquad (4.\ 11)$$

Where $u \in \mathbb{R}^n$ is the measured signal/image, $A \in \mathbb{R}^{n \times m}$ $(m < n)$ is the measurement matrix, $D_i u \in \mathbb{R}^2$ is the discrete gradient of u at pixel i and $b \in \mathbb{R}^m$ are the linear measurements that are observed. Due to the non-differentiability and non-linearity of the TV term within equation 4.11 it is extremely difficult to directly solve. A method of bypassing these restrictions are to approach the problem by rewriting it as a sequence of linear unconstrained sub-problems. This was initially seen in 1943 where Courant developed the quadratic penalty method [193], where the constraint in the objective function is replaced with a quadratic penalty term. This method was extensively used due to its simplicity, however it was often ill-conditioned due to the multipliers being required to go to infinity to guarantee convergence. A solution to this problem was proposed in 1969 independently by both Hestenes [194] and Powell [195], whereby an explicit Lagrangian multiplier is introduced and estimated at each iteration in a method known as the augmented Lagrangian method.

To apply this method to minimize the TV model in equation 4.11, the corresponding augmented Lagrangian function is,

$$\mathcal{L}_A(w_i, u) = \sum_i (\|w_i\| - v_i^T (D_i u - w_i) + \frac{\beta_i}{2} \|D_i u - w_i\|_2^2)$$
$$-\lambda^T (Au - b) + \frac{\mu}{2} \|Au - b\|_2^2 \qquad (4.\ 12)$$

Where, v_i and λ are multipliers and β_i and μ are penalty parameters. Due to equation 4.11 being a convex problem, the global convergence theorem can guarantee that

convergence is achieved whilst applying the augmented Lagrangian method. The sub-problem is to now minimize equation 4.12 at each iteration whilst updating the multipliers v_i and λ according to the formulas presented by Hestenes and Powell,

$$\tilde{v}_i = v_i - \beta_i(D_i u^* - w_i{}^*) \; for \; all \; i,$$
$$\tilde{\lambda} = \lambda - \mu(Au^* - b). \qquad (4.\ 13)$$

Where u^* and $w_i{}^*$ represent the true minimisers of equation 4.11. For this to be problem to be solved it is critical that equation 4.12 is minimized efficiently at each iteration, however this is still difficult due to the non-differentiability and non-linearity present. In order to combat this, an alternating direction minimisation scheme was proposed so that a solution could be found efficiently.

The alternating direction method [196], developed by Peaceman and Rachford in 1955, was originally intended to be used to solve parabolic and elliptic differential equations. This method splits the sub-problem down further to solve for each multiplier separately, using the so-called “w-subproblem” and “u-subproblem”, where each separated problem has a closed form solution. Within the TVAL3 algorithm, all variables are initialized and starting points are selected, the iterative process then begins. Firstly, whilst some outer stopping criteria has not yet been met, which can be selected based on whether optimality conditions have been met or the relative change in $\|u_{k+1} - u_k\|_2$ is sufficiently small, minimisers $u^* \; and \; w_i{}^*$ of the augmented Lagrangian function are calculated. This is done using the alternating direction method where whilst an inner stopping criteria has not yet been met, which is similar to the outer stopping criteria, $w_{i,k+1}$ is computed using a shrinkage-like formula,

$$w_{i,k+1} = shrike(D_i u_k; v_i, \beta_i) \quad (4.\ 14)$$

where, the operator shrike represents using a shrinkage-like formula to solve using either an anisotropic or isotropic TV model. Once $w_{i,k+1}$ has been computed, u_{k+1} can then be calculated using a one-step steepest descent method,

$$u_{k+1} = u_k - \alpha_k d_k \quad (4.\ 15)$$

where, d is the gradient direction of the objective function and α is the step length. The step length is set at each iteration using a Barzilai and Borwein (BB) [197]– like formula,

$$\alpha_k = \frac{s_k^T s_k}{s_k^T y_k} \quad (4.\ 16)$$

where, $s_k = u_k - u_{k-1}$ and $y_k = d_k(u_k) - d_k(u_{k-1})$. In order validate the BB-like step at each iteration, a nonmonotone line search formula that was developed by Zhang and Hager [198] is used. This process continues until the inner stopping criteria has been met, where the multipliers defined in equation 4.13 are updated and new penalty parameters are selected. The algorithm can also be extended to work with other TV models with added constraints such as non-negativity constraints which are suitable in the area of image reconstruction.

This algorithm was tested against other image reconstruction algorithms by taking a 64 by 64 phantom and encoding it with an orthogonal random matrix. Images were reconstructed using 30% measurements with TVAL3, TwIST [199], NESTA [200] and

l1-magic algorithms with zero additive noise. The quality of the reconstructions were measured using the signal to noise ratio as well as the CPU time taken to complete the reconstruction. From the results that are shown in figure **4.2**, it is observed that the TVAL3 achieves the highest quality reconstruction whilst also requiring the least CPU running time [201].

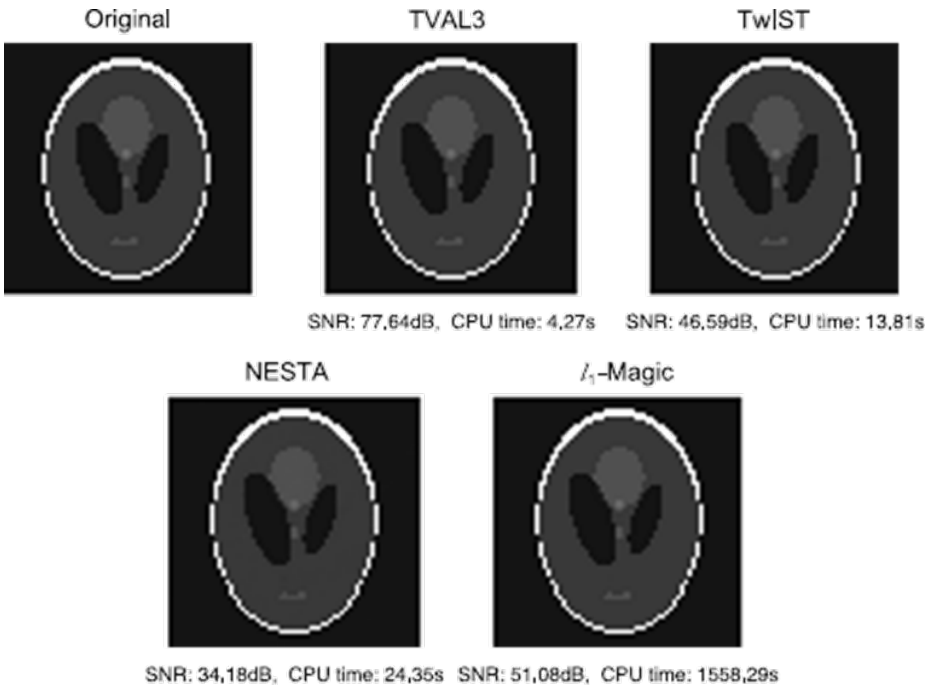

Figure 4.2. Recovery of a 64x64 phantom image (top-left) from 30% noiseless measurements. Top-middle: Reconstruction using TVAL3. Top-Right: Reconstruction using TwIST. Bottom Left: Reconstruction using NESTA. Bottom Right: Reconstruction using l1-Magic. Image credit: [201]

4.2.3. CSCG

Developed at the University of Birmingham by Basevi et al. [202], the Compressive Sensing Conjugant Gradient (CSCG) algorithm was made specifically to aid in the imaging of sparse and compact source distributions such as those found in bioluminescent based cancer studies or macroscopic cell tracking. By re-writing equation 4.2 in terms of a bioluminescent source distribution,

$$y = Jb, \tag{4. 17}$$

where y is a vector of measurements made at defined boundary points, J is a spectrally varying sensitivity matrix and b is the source vector which is defined as a value per-node when using a FEM model. As this problem is both ill-posed and highly under-determined (typically around 1-2 orders of magnitude difference between known measurements and unknown values), an accurate compressive sensing based algorithm is well suited to the problem. Described in detail by Basevi et al. [202], the algorithm combines a least squares fit of the data which aims to minimize the measurement error, along with an L_1 norm minimizing component with favours spatial sparsity within the reconstructed image, giving the objective function,

$$b = \min_b \|y - Jb\|_2^2 + \gamma \|b\|_1, \tag{4. 18}$$

where, γ is the relative weighting between the two parts of the function. It is has been shown previously [18, 203] that solving for equation 4.18 is equivalent to solving,

$$b = \min_b \|b\|_1 \; such\; that \;\; \|y - Jb\|_2^2 < \varepsilon, \tag{4. 19}$$

where, ε is an error threshold that is a function of γ. To solve this problem a conjugant gradient method [18] is implemented, which solves using an iterative process with decreasing values of γ. The initial value of γ is chosen so that the sparsity term is much larger than the measurement error term which gives the algorithm the effect of ‘guided’

least squares fitting which finds an optimum solution that minimizes the measurement error whilst being influenced by sparsity. The algorithm also has the option to constrain the solution to be non-negative, which for the case of bioluminescent tomography will help reduce the non-uniqueness of the solution and further improve the accuracy of the algorithm. The iterative process will continue until the solution is believed to have converged, which is defined as when the error threshold of sparsity weighting has reduced below a set threshold. In order to assess the algorithms performance when reconstructing the spatial distribution of a bioluminescent light source, it was compared to two standard reconstruction algorithms. The algorithms selected for comparison were a Gauss-Newton (GN) and Non-negative Least Squares (NNLS). Through the use of both simulated and experimental data, it was shown that the CSCG algorithm displayed improved compactness and reduced noise artifacts when compared the GN and NNLS methods. There was also much improved source localization when compared to the GN method, whilst showing similar if not better localization when compared to the NNLS method.

4.2.4. Spectral Derivative Method

There are several effects that may lead to erroneous results when carrying out non-contact BLT reconstructions, including animal position and surface geometry. Traditionally, to overcome these problems 3D surface capture systems can be used alongside a free-space model which accounts for the propagation of light from the surface of the animal to the detector. However, these capabilities are not always available, reducing the accuracy of reconstructions. To overcome these issues Dehghani et al applied the spectral derivative method, which had already been shown

to improve reconstructions in near infrared spectroscopy (NIRS) [204], to bioluminescence tomography [13].

Due to the differences in measured data caused by animal position, it is assumed that there is a measurement point specific angular dependent offset n, that is spectrally invariant. By applying this assumption, equation 4.17 can be modified to be:

$$J_\lambda x = b_\lambda n \tag{4. 20}$$

To account for this offset, the logarithm of data is used by multiplying equation 4.20 by $\frac{\log (b_\lambda n)}{b_\lambda n}$, giving:

$$\frac{log\ (b_{\lambda i} n)}{b_{\lambda i} n} J_{\lambda i} x = log\ (b_{\lambda i} n) \tag{4. 21}$$

The difference between neighbouring wavelengths is then used by subtracting the data measured at two nearest wavelengths, which gives:

$$\left[\frac{log(b_{\lambda i} n)}{b_{\lambda i} n} J_{\lambda i} - \frac{log(b_{\lambda i+1} n)}{b_{\lambda i+1} n} J_{\lambda i+1}\right] x = \frac{log(b_{\lambda i})}{b_{\lambda i}} \tag{4. 22}$$

By doing this, any spectrally invariant properties such as the animal geometry and position are cancelled out and any measurements taken (right hand side of equation 4.22) no longer depends on the unknown parameter n.

The spectral derivative algorithm has been shown to improve the quantitative accuracy of bioluminescence tomography by up to 10 times [13] and is the standard reconstruction technique used in any reconstructions presented in this thesis.

4.3. Applications

4.3.1. Single-Pixel Camera

A ground-breaking and significant application of compressive sensing is the development of the single-pixel camera by Baraniuk, Kelly, et al. in 2006 [17, 205]. The architecture of the single-pixel camera is fairly trivial and only involves two main components as can be seen in figure 4.3. The first is a digital-micromirror-device (DMD) [206], which is an array of individually controllable micro-mirrors in either an off (0) or on (1) position. The DMD is used to display the pseudo-random patterns as defined by the measurement matrix Θ in equation 4.2. The second component is a single point detector such as a photodiode, which is used to collect the light which travels from the scene and reflects from the DMD.

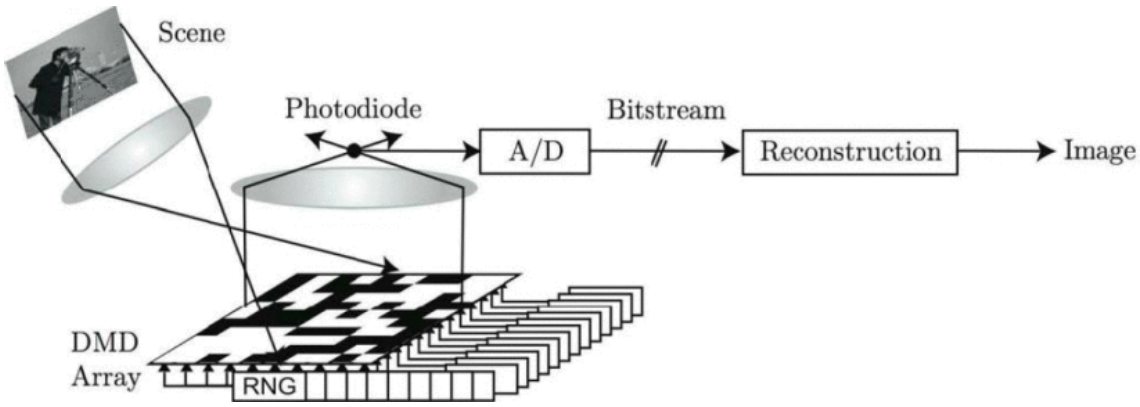

Figure 4.3. The architecture of the single pixel camera. This figure has been replicated from Baraniuk, Kelly, et al. [17]

When a pattern is displayed on the DMD, the detector will collect a measurement, which is repeated until all patterns making up the measurement matrix Θ have been used. This will leave a vector of M linear measurements which is typically lower than

the original resolution of the image. Because of this the problem is therefore underdetermined and can be modelled as a compressive sensing based problem and a suitable algorithm can be used to reconstruct the underlying image. When the single-pixel camera was first developed, it adopted the toolbox L_1- magic as its primary recover solvers, which are based on L_1 minimisation schemes. However due to the benefits of TV minimisation schemes such as better edge detection and preservation, these solvers are much better suited to the single-pixel camera. Since its development the single – pixel camera and compressive sensing based solvers have been utilised widely within the scientific and medical community.

4.3.2. Compressive Sensing in Health Monitoring

With the increased popularity and functionality of compressive sensing, its application to health monitoring is an important and useful exercise. Health monitoring is defined by the technologies that monitor the vital signals from the human body, which can take multiple forms, such as Electrocardiogram (ECG) [207], Magnetic Resonance Imaging (MRI) [18] and Computed Tomography (CT) [208]. By applying compressive sensing to health monitoring technologies, it is possible to reduce the high volume of data that is typically required in each modality, allowing for examinations to be much shorter than normally required.

ECG is a technique that is used to measure the electrical activity of the heart so that a physician can check it's functioning correctly. This is an important modality as currently worldwide cardiovascular problems and heart disease is the leading cause of death [209]. Due to the emergence of wireless, wearable ECG devices [207], one of the main issues faced with ECG is the battery capacity and data transfer. By applying

CS to ECG, it is possible to reduce the number of samples that are required to reconstruct a signal, therefore reducing the size of the data being transferred, which in turn reduces the energy required improving the battery consumption of the devices [207].

Computed Tomography (CT) is an imaging technique that uses multiple X-Ray projections to build a 3D image of the human body [210]. This is an extremely important imaging modality as it can be used to analyse and detect many different abnormalities and conditions. The main issue with CT is the radiation exposure associated with it, therefore it is necessary to reduce the dose that is received during a scan. To do this in a standard way would require fewer projections to be taken, in turn reducing the clarity of images, making it not a viable option. By applying compressive sensing to CT can reduce the required amount of data to recover a clear image, reducing the dose that is received by a patient. CS has been applied to CT in multiple ways, including by Yu et al. where internal reconstruction methods can be used to obtain relevant information from global projections [211]. Another application by Van Sloun et al. is to used CS in ultrasound computed tomography (UCT) to reconstruct measurable tissue characteristics [208]. This allowed for reduced sensing which minimised data acquisition times without affecting the quality of images.

Magnetic Resonance Imaging (MRI) is a modality of imaging which uses magnetic fields and radio waves to measure the movement of the nucleus of atom [212]. Due to no ionising radiation being used, MRI scans cause no harm to human beings, however issues arise due to limitations of the device. One limitation is due to the long period of time a scan takes as well as the patient being required to lay as still as possible. CS can be applied to MRI since images created are sparse in a particular domain (typically

using a discrete wavelet transform [213]) and can be utilised to vastly reduce the time required to collect data [214]. Other than standard MRI [18], there has been a number of different applications of health monitoring that utilise compressive sensing with MRI. Firstly, Lustig et al. stated that angiograms are very sparse in nature and presented the application of 3D angiography, preserving blood vessel information with only 5% of measurements [215]. Another application is in neuroimaging and functional MRI (fMRI) [216], where CS has the ability to reduce the data collection time and improve image resolution.

The vast amount of research and advances in technology has allowed for the commercialisation of applying compressed sensing to clinical MRI scanners by several companies such as Phillips and Siemens[217]. Combining ideas from parallel imaging such as Sensitivity Encoding (SENSE) [218] and Generalised Autocalibrating Partially Parallel Acquisitions (GRAPPA) [219], with compressive sensing ideas described in this chapter, CS acquisition and reconstruction has been fully integrated into clinical MRI scanners. Siemens have integrated an award winning CS reconstruction algorithm developed by Liu et al [220], which adds new capabilities to MRI due to the acceleration of real time sequences. An example is in cardiac imaging which now allows for full quantification of left-ventricular function within the time of a single breath-hold [221].

4.4. Conclusion

This chapter has provided an introduction to the theory behind compressive sensing, including the idea of how sparsity can affect the potential for reducing the number of measurements required to fully represent a signal or image. This was followed by discussing methods of recovering sparse signals/images from compressed

measurements such as L_1 minimisation and TV minimisation. Different optimisation algorithms, that have been utilised in this work, that can be used to implement both L_1 and TV minimisation have been presented. The chapter ended with a review in current applications of compressed sensing included health monitoring and the single pixel camera, which is the basis behind the novel system developed as part of this work.

The following chapter introduces the design and construction of the novel imaging system developed as part of this work. It also presents characterisation, automation and methods of operating the system.

CHAPTER 5
SYSTEM DESIGN AND CONSTRUCTION

In this chapter, a novel system developed for performing in-vivo bioluminescent imaging and tomography of small animals is described. The system is used to capture diffuse hyperspectral light at the surface of the small animal (subject of chapter 3), using a compressive sensing based detection scheme (subject of chapter 4). From this data, using the algorithms described in chapters 3 and 4, this system is able to achieve quantitatively accurate tomographic reconstructions of spatially distributed bioluminescent sources in-vivo (subject of chapter 6). Along with the system proposed, a novel algorithm has been developed to provide simultaneous recovery of both the unknown underlying optical properties, as well as reconstructing the spatial light distribution of the bioluminescent source from the same hyperspectral data set collected from the surface of the small animal (subject of chapters 7 and 8).

All parts of the hyperspectral imaging system are discussed in this chapter, including every individual component in detail so that it could be reproduced. System response functions and noise characterization are also evaluated and discussed, along with detailed information on how the systems automated data collection is carried out.

5.1. System Overview

Throughout the development of the imaging system there has been two versions, the first using a pre-built optical system as shown in figure 5.1. The second upgraded system followed exactly the same detection scheme as the first, however each component within the optical system was optimized to improve the signal to noise ratio of the whole system, which can be seen in figure 5.2. Both systems employ a typical

basic layout that can be seen in established small animal imaging systems such as that of Guggenheim et al. [1], where a horizontal stage is used to support the small animal underneath the optical system with a vertical light path. The entire system is housed within a light tight box to limit as much background light entering the system as possible.

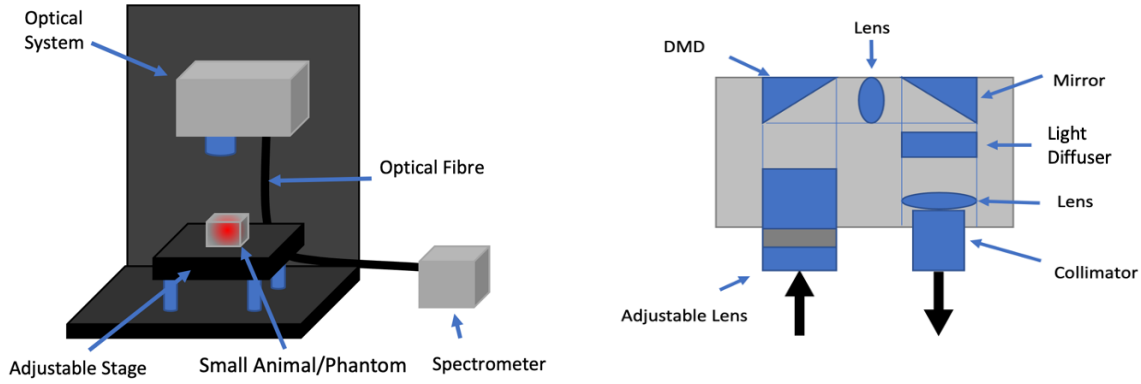

(a) (b)

Figure 5.1. Developed system schematics (a) Labelled schematic of the developed system and (b) a labelled schematic of the optical system used in the first iteration of the developed imaging system. This system was developed by altering an existing Texas Instruments Lightcrafter DLP.

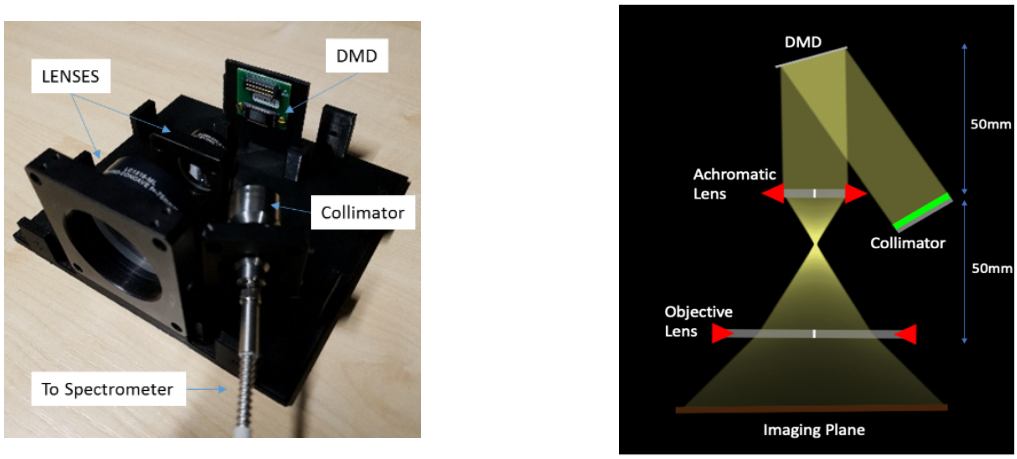

(a) (b)

Figure 5.2. Custom optical system (a) Labelled image of the custom designed optical system and (b) Simple ray diagram showing the optics of the custom designed optical system.

The second system was custom designed to optimize the optics within the optical system, to increase the light throughput by reducing the distance between the subject and the detector and by increasing the aperture of the lenses used.

5.2. System Components

5.2.1. Enclosure and Support

The entire imaging system is contained within a cage and support structure that accounts for two main functions. The first is to provide a physical structure for which components of the imaging system can be held securely in place. The second is to render the entire system dark so that any background light that could potentially affect the signal to noise ratio is removed. This is specifically important in the area of bioluminescent imaging due to the extremely low light levels being detected through highly attenuating tissue.

The outer shell of the cage is constructed from square aluminium posts (RS Components, Corby, UK) that are attached directly to an optical bench (Thorlabs, Cambridgeshire, UK). The optical system and components are attached to a 600 mm by 150 mm optical breadboard (Thorlabs, Cambridgeshire, UK) that is mounted in a vertical position to the optical bench. A smaller 150 mm by 150 mm is mounted on four ½ inch optical posts and placed within 4 post holders that are connected to the optical bench. This board is situated where the imaging plane of the system is and its height can be adjusted, to bring the system into focus. On the outside of the shell, black acrylic sheets are mounted to completely enclose the system and render it dark. The front sheet of acrylic is mounted to hinges and acts a door to the system so that the optics and imaging plane can be accessed. Any joins in the outer panels were covered with

black tape to remove any leakage of light between panels. Figure 5.3 shows the system and dark box mounted upon the optical bench.

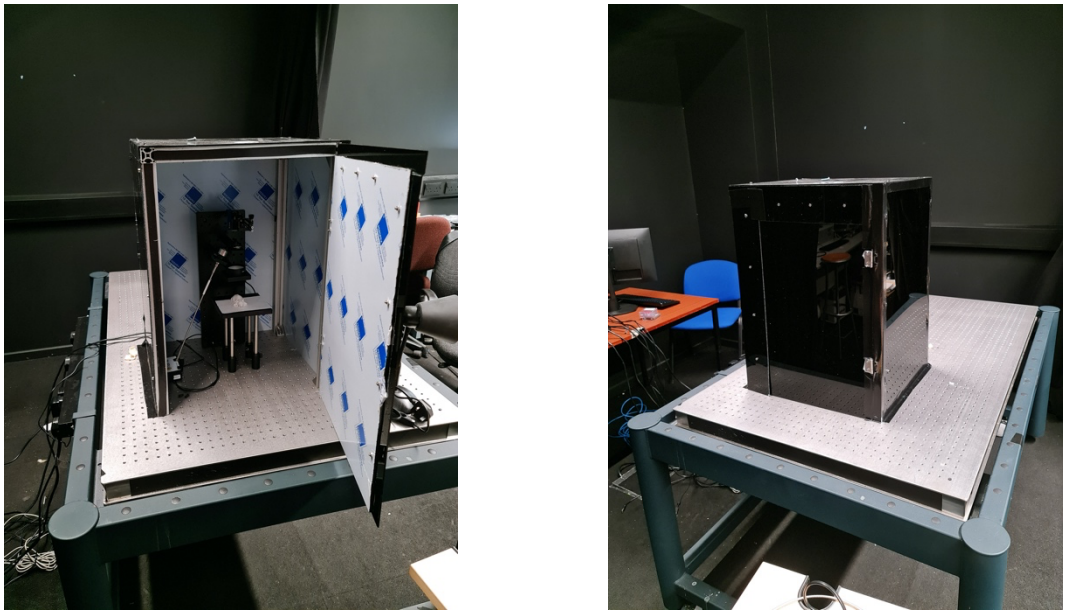

Figure 5. 3. The optical system dark housing shown with the door open and closed.

Figure 5.4. shows a prototype system that was initially developed to carry out proof of concept tests. This system involved using the pre-built optical system of a Texas Instruments DLP Lightcrafter 4500. To modify the system to be used in application of imaging the three RGB projection LEDs were removed and a ½ inch collimator was placed in the same location. The system was then operated as if it was a projector by streaming binary patterns onto its DMD through a HDMI cable. The system included an adjustable 1 inch objective lens that focuses light onto a DMD which is used to display binary patterns that reflect light into a collimator through a series of lenses, mirrors and a light diffuser. The role of the light diffuser is to ensure equal illumination from the DLPs LEDs on the DMDs surface.

The final system design, as shown in figure 5.2(a), utilized a custom built optical setup to reduce the total pathlength of light and maximize light throughput. To do this

a number of optical components were used in combination. The first is a large 2 inch objective lens (Thorlabs, Cambridgeshire, UK) shown in figure 5.5(a), with a fixed focal length of 75 mm. This lens was chosen to both maximize the amount of light entering the lens whilst minimizing the distance between the lens and the imaging plane. After this lens there is an achromatic lens (Thorlabs, Cambridgeshire, UK) with a fixed focal length of 25 mm. This lens was chosen to account for any chromatic aberration that occurs due to the DMD. Finally, a 1-inch air-spaced doublet collimator (Thorlabs, Cambridgeshire, UK) shown in figure 5.5(b) was used to focus the light into an optical fibre. This collimator has a fixed focal length of 35 mm, a numerical aperture of 0.25 and has an alignment wavelength of 635 nm making it suitable to be used in bioluminescence imaging. Figure 5.2(a) shows a simple ray diagram displaying the path of light through the optical system.

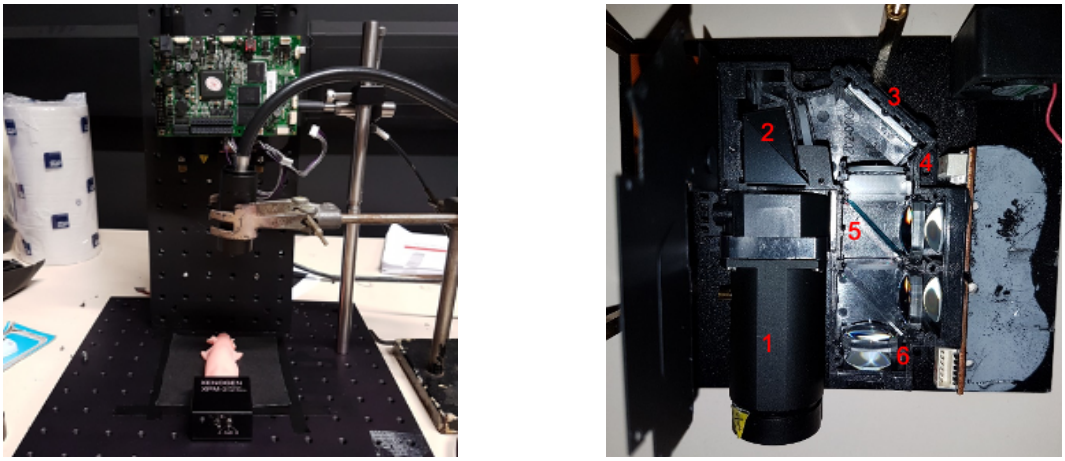

(a) (b)

Figure 5.4. Prototype system (a) An image of the initial prototype system using a prebuilt Texas Instruments Lightcrafter DLP. (b) The inside of the optical engine showing, 1. An adjustable 1-inch objective lens, 2. The DMD, 3. A inch standard mirror, 4. A light diffuser, 5. Dichroic mirror and 6. The location of the ½ inch collimator that connects to the sensor.

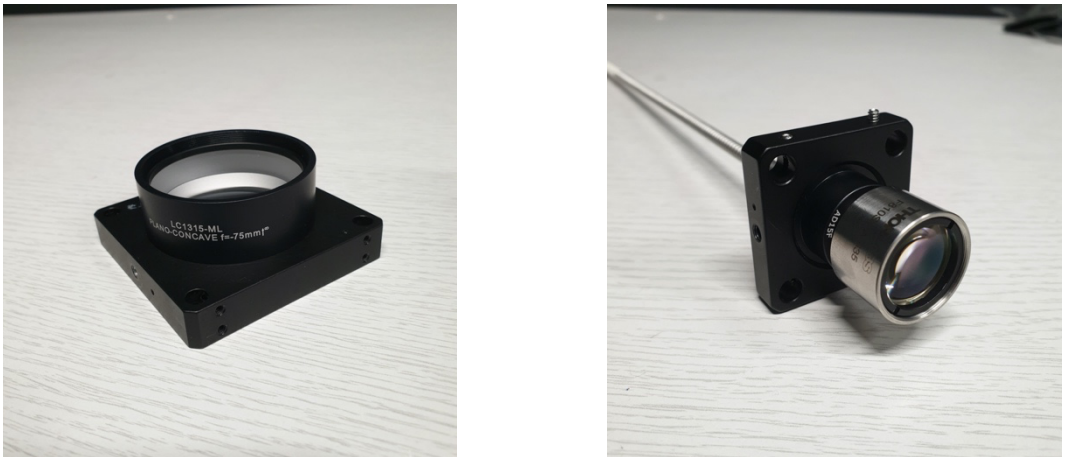

(a) (b)

Figure 5.5. System optics (a) A 2 inch objective lens with focal length of 75mm used in the custom optical system. (b) A 1 inch air spaced doublet collimator with a focal length of 35 mm used in the optical system.

To take light from the collimator into the sensor a multimode 1500 μm optical fibre (Thorlabs, Cambridgeshire, UK) of length 30 cm was used. This fibre was chosen as it has a higher numerical aperture of 0.5 and largest core size available to maximize the light through put. Finally, in order to display the binary patterns to randomly sample the imaging plane, a DLP4500 .45 WXGA DMD (Texas Instruments) was used. This digital micromirror device (DMD) is a 0.45 inch diagonal micromirror array containing a 912 by 1140 array of highly reflective micromirrors each of which can be digitally switched into an on (+12^o tilt) or off (-12^o tilt) position. Light reflected from mirrors in the 'off' position is absorbed by the black Perspex material of the outer casing. The DMD used is optimised to operate at wavelengths between 420 nm and 700 nm, making it suitable for bioluminescence imaging. The DMD can be operated through the use of streaming patterns or images through a HDMI cable or by uploading the patterns to the on board memory. By operating in a continuous streaming mode it is possible to achieve pattern rates of up to 2880 Hz, however through the use of a burst operation mode it is possible to achieve a pattern rate of 4220 Hz using patterns saved to the

internal memory. Figure 5.6 shows a macroscopic image of the DMD, as well as a schematic of how each micromirror operates.

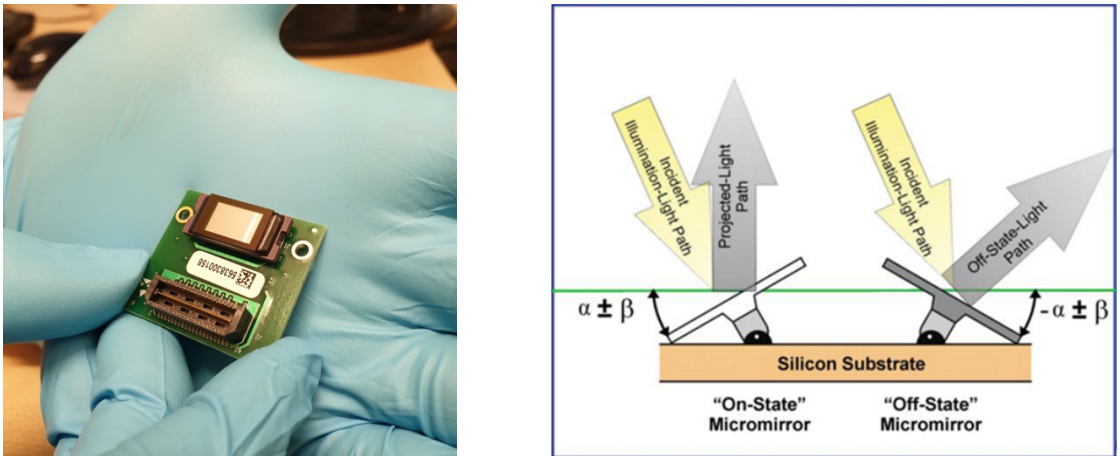

(a) (b)

Figure 5.6. Digital micro-mirror device (a) A macroscopic view of the DMD used. (b) A schematic of how each micromirror is operated where α is the resting angle (0^o) and β is the tilt angle ($\pm 12^o$). The path of the light when the mirror is in each state is also highlighted [REF TI Manual].

5.2.2. System Housing

To house and to hold all of the systems optical components in alignment a housing was designed using Autodesk Fusion 360. The housing is shown in figure 5.2 and is a modular 3D printed case that was printed out of black PLA using an Ultimaker S3. The case includes slots for each optical component to be held in place with a separate compartment to house the electronics of the DMD. This was done due to LEDs being present on the DMD and may introduce unwanted noise into the system. The housing also includes a front plate that has holes to accommodate the objective lens as well an HDMI and power cable that connects to the DMD control board.

5.2.3. Spectrometer

The sensor used in the system shown in figure 5.2 is a Ocean Insight (formally Ocean Optics) FlameS VIS-NIR spectrometer (Ocean Insight, Florida, USA), which is a compact spectrometer with interchangeable slits and gratings that operates between 300 and 1000 nm with a spectral resolution as low as 0.1 nm. The detector in the spectrometer is a Sony ILX511B linear silicon CCD array, which contains 2048 pixels, with physical size of 14 μm by 200 μm. For use in this application the largest slit of 200 μm was used to maximise the light throughput into the spectrometer, whilst only increasing the spectral resolution to 0.4 nm. This spectrometer was chosen for its high sensitivity over the visible and near infrared range with a low cost (~$3000). The spectrometer can be controlled using the OceanView software, however can also be controlled using 3rd party software such as MATLAB and LabView. It is able to collect data with an integration time as low as 1 ms.

5.3. System Characteristics

In order to correct any data and images that were collected using the created system a number of system characteristics were measured. The first is an instrument response function that represents any spectral changes to measurements that are due to the components of the system. The second is a characterization of the imaging plane to account for any differences measured in intensity across the plane. The final characteristic is an investigation of the noise profile of the system due to the spectrometer itself and any background light that may be present.

5.3.1. Instrument Response Function

The instrument response function (IRF) was measured using a 630 nm red LED, which was selected due to its resemblance of a typical bioluminescence signal. First a measurement was taken by placing the LED close (~20 mm) to the entrance of the spectrometer. Then a measurement was taken through the system by placing the led in the middle of the imaging plane and setting all the micromirrors on the DMD to the on position. Data was acquired for 200ms in each case and averaged across 50 measurements. To calculate the IRF both measurements were normalized, and the ratio of the signals was calculated. Figure 5.7 shows the normalized system response, which was applied to any data that was collected with the developed imaging system.

Limitations of this IRF arise from the methodology used to calculate it. Instead of using an LED, a more accurate IRF could be measured using a white light source such as a halogen light source. This would provide a more constant source of light at a much wider range of wavelengths and therefore result in a more accurate IRF measured. Due to this limitation, there is only a small window between 600 nm and 650 nm where the response function may be accurate, therefore this IRF was not applied to any of the data that has been presented in this thesis.

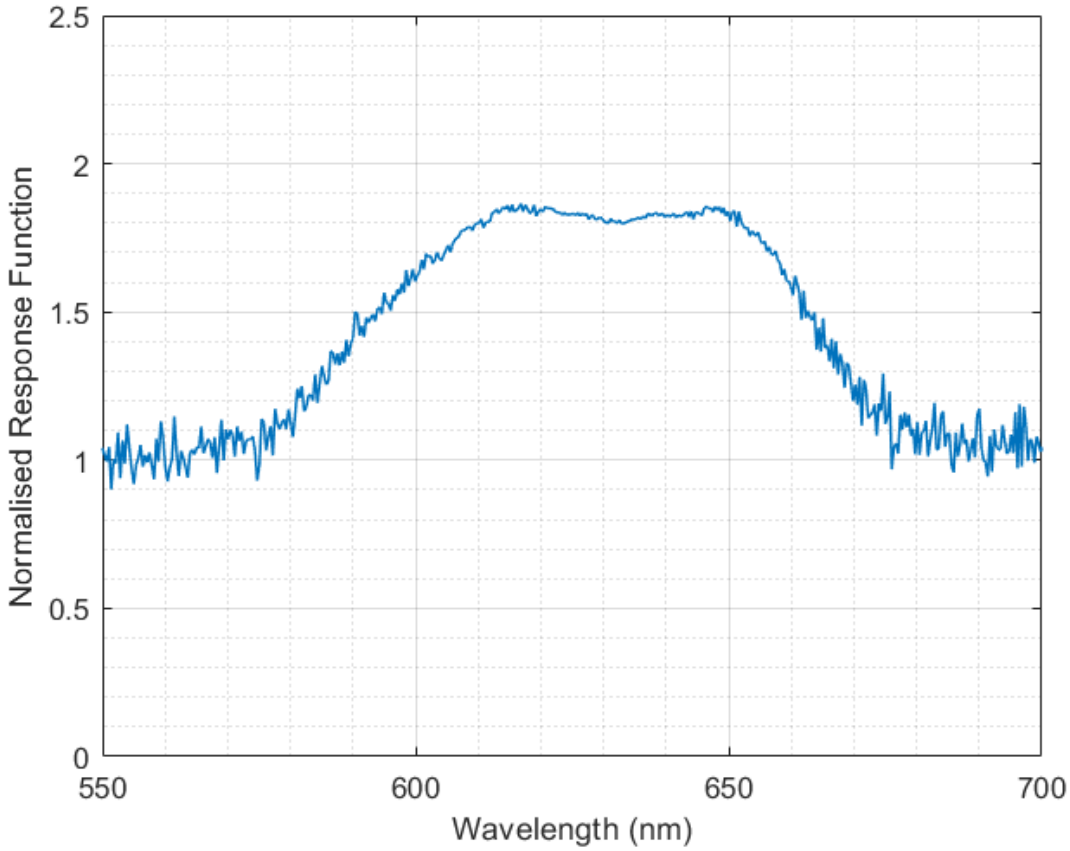

Figure 5.7.The normalised instrument response function of the developed system.

5.3.2. Imaging Plane

In order to characterize the imaging plane to allow for any inconsistences measured across it to be corrected for, testing using an LED array was used to create a correction function that could be applied to reconstructed images. This was done using an 8x8 LED array (40 mm x 40 mm), shown in figure 5.8(a), placed within the imaging plane of the system, whilst setting all of the mirrors of the DMD to an 'ON' position. Each LED was then turned on sequentially and spectral data was collected using an integration time of 20 ms per LED. Data was collected across the whole array 50 times and then averaged to allow for any variation in the individual LEDs over time. Figure 5.8(b) shows the collected data averaged across the whole spectrum for each pixel within the

imaging plane. This function can be applied to reconstructed images to correct for differences in measured light across the entire imaging plane.

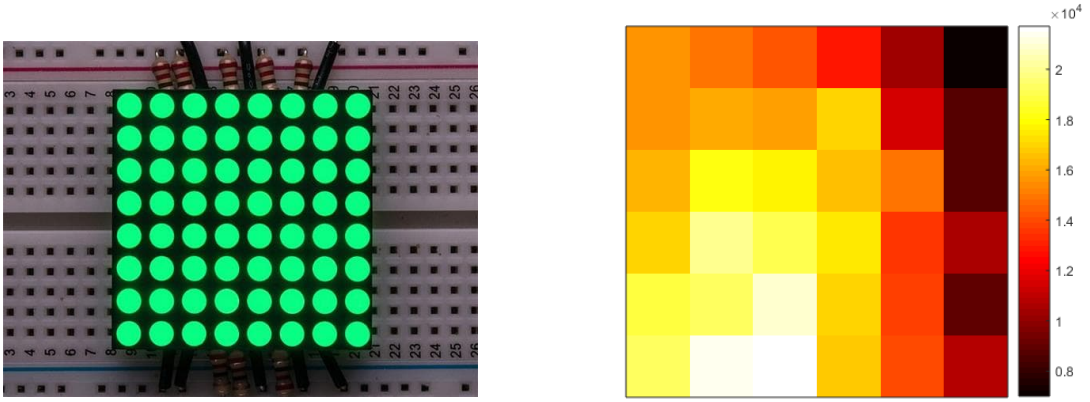

(a) (b)

Figure 5.8. Imaging plane correction (a) The LED array used to collect the intensity of light measured at each pixel with the imaging plane of the system. (b) The averaged data collected, that can be used as a function to correct ay reconstructed images.

5.3.3. Noise

In order to build an accurate noise model for the developed system, it is first important to understand the origins of any noise that may be present. The first source of noise is photon shot noise which is fundamental noise that a stable light source will have. The second source of noise is baseline noise, which depends on the read-out electronics of the sensor itself. Over short periods of time (< 1 sec) the effect of this is generally very small so can be disregarded in this application. The third source of noise is dark noise, which is caused by dark current, and the spectrometer has a function to correct for this itself when data is collected. The final source of noise is read noise, which is fixed noise that is associated with the detector and unavoidable when reading out data. The different noise sources can be assumed to be independent and have normal

distributions, so the total noise of the system is calculated by summing the squares of each noise source.

The noise of the system is proportional to the integration time being used due to it being a combination of all four noise sources as well as any background light that is present during imaging. In order to correct collected data for noise within measurements a ‘dark’ spectrum is collected from the system by setting all of the mirror to an ‘OFF’ position and then collecting a spectrum using the same integration time that will be used for data collection. This spectrum is then averaged across the wavelengths of interest where the light source being measured is (typically ~ 550 nm - ~700 nm) and subtracted from the measured data after data collection, before image reconstruction.

5.4. System Automation and Data Collection

In order to collect data, MATLAB scripts were created to automatically collect data after any variables (such as spectrometer integration time and image resolution) had been defined. A MATLAB graphical user interface (GUI) was developed in order to streamline the process and make the system accessible to any potential user. The next section describes the process of data collection using the automation scripts and the MATLAB GUI.

5.4.1. Automation Scripts and Data Collection

To collect data using the system a MATLAB automation script is used. Firstly variables, such as the resolution of images, number of spectra and integration time per spectra are initially defined and then the script can then be run. Firstly, the script will create a

randomly generated measurement matrix from a Bernoulli distribution with probability 0.5, that has the dimensions of the resolution of images by the number of spectra being measured. For practicality, all -1 entries of the measurement matrix are changed to 0 so that it can be displayed on the DMD. Each column of the matrix defines a binary pattern that is to be displayed on the DMD for data collection. Once the matrix has been generated it is saved so that it can be used post data collection for image reconstruction. The spectrometer is then initialized using the integration time specified by the user and data collection begins. Firstly a 'dark' measurement is taken by setting all mirrors to an off position, followed by a 'light' measurement by setting all of the mirrors to an 'ON' position. The 'light' measurement is used to convert the measured data from a basis using patterns made up of 1's and 0's to a basis that uses 1's and -1's. The main data collection process then begins by displaying the first pattern defined by the first column of the measurement matrix on the DMD. A spectrum is collected by the spectrometer and then the second pattern, defined by the second column of the measurement matrix, is displayed on the DMD. This process is repeated until all of the measurements have been collected, producing a hyperspectral dataset shown in figure 5.9 where each colored line represents an individual pattern. A second script is then used for image reconstruction whereby the spectral data and measurement matrix are loaded into the workspace. Within this script, firstly the desired wavelengths of reconstruction are selected, and image reconstruction begins. Initially the data collected is converted from the binary basis to a basis of 1's and -1's, followed by a background subtraction using the value calculated using the 'dark' measurement. The instrument response function is then applied to the spectral data to correct for any changes due to the system itself. This data is then fed along with the measurement

matrix into a total variation (TV) minimizing algorithm, described in chapter 3. This algorithm reconstructs the pixel-by-pixel image within the imaging plane at each wavelength that has been selected. After reconstruction the imaging plane correction function is then applied to each image and the output is individual corrected images at each wavelength which are saved.

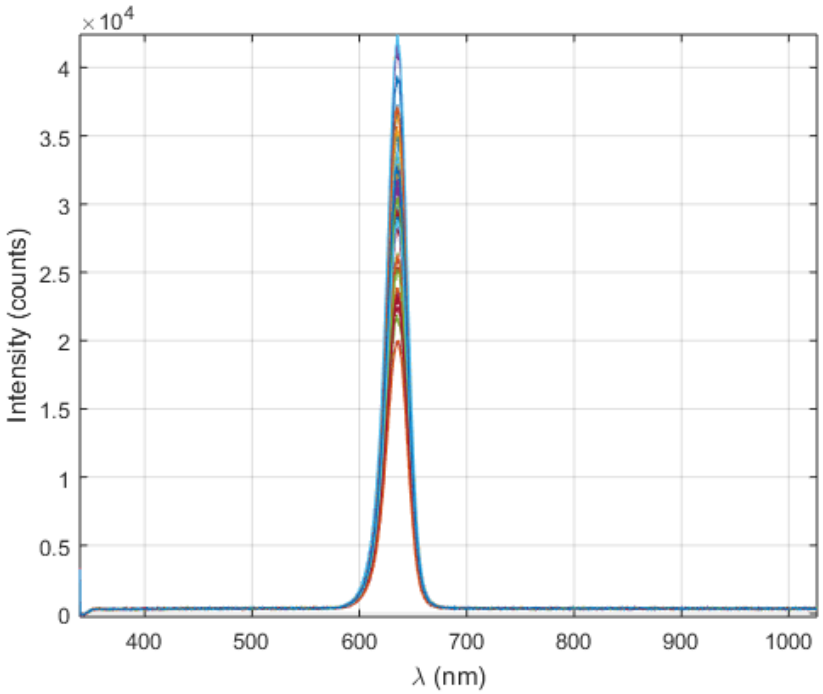

Figure 5.9. Example spectral data of a red LED collected using the system. Each different coloured line represents an individual pattern displayed on the DMD.

5.4.2. Graphical User Interface

A MATLAB graphical user interface was developed to allow the system to be used by any potential user without the need to access individual automation scripts. The GUI as shown in figure 5.10, included options to select the different variables for data collection before pressing a button to start data collection. Data is collected using the same process as the automation scripts, however, the GUI also has the functionality to preview the raw spectral data before using a button on the GUI to save the dataset.

A final module on the GUI can be used to select the wavelengths of light used for image reconstruction as well as an option to select the mesh used in tomographic reconstruction which is the topic of the following chapter.

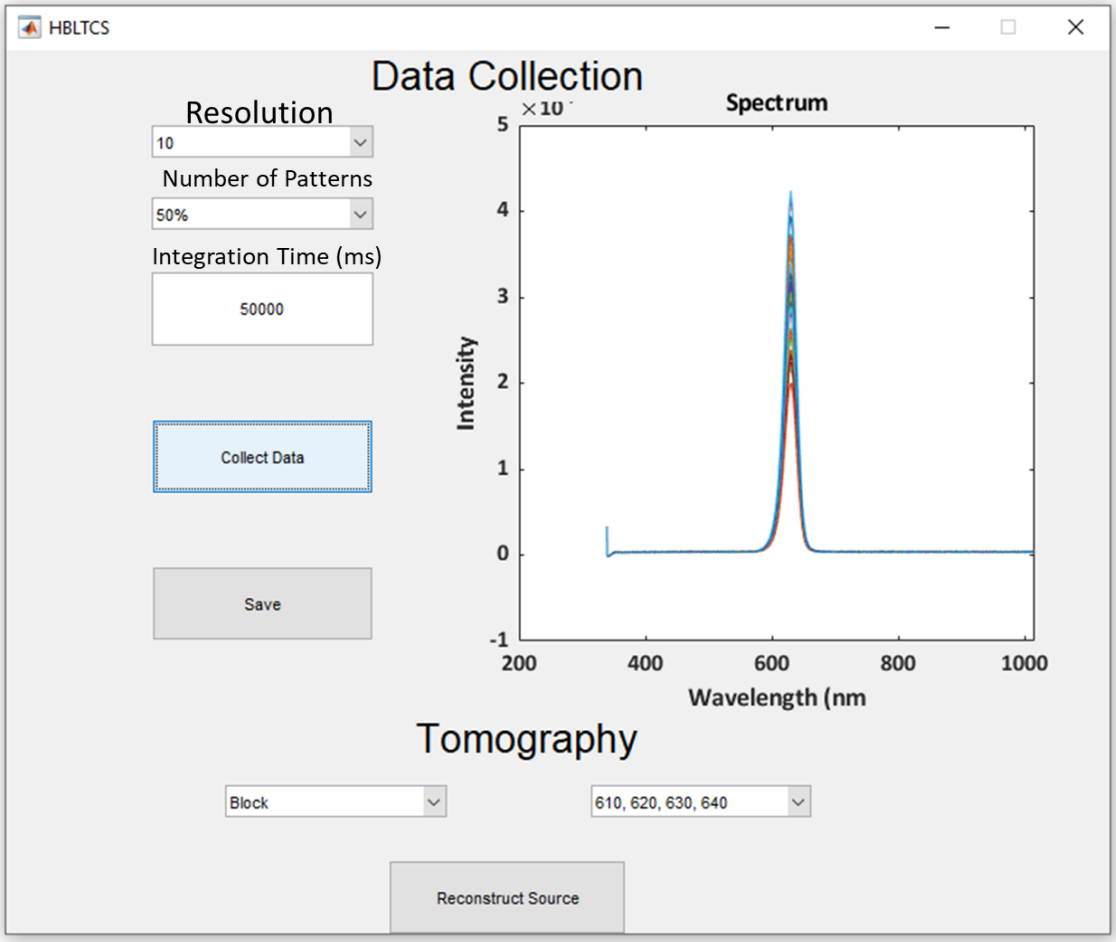

Figure 5.10. The graphical user interface used for data collection. It includes options to select the resolution of images, number of patterns and integration time before collecting data. It also features a preview panel used to view data before saving, as well as a module used for selecting wavelengths and a mesh used for image and tomographic reconstruction.

5.5. Conclusion

This chapter has introduced the design of the novel system which has been developed as part of the work presented in this thesis. The system is designed to collect compressed hyperspectral data from the surface of a small animal, utilising the concept of compressive sensing (Chapter 4) to recover images with fewer measurements than typically required. Different components utilised in the system have been described and key design considerations have been shown. A number of different system characteristics have also been presented including how images captured with the system are corrected for noise, spectral response and discrepancies in the system imaging plane. Methods of operating the system are described including automation scripts and a user-friendly graphical user interface.

The remainder of this thesis follows the initial experiments that were carried out to further characterise and prove the concept of the novel imaging system being presented. Following on from this a novel dual-parameter reconstruction algorithm is presented that can be utilised alongside the developed system to aid in reconstructing internal spatial light distributions without requiring a priori knowledge on the underlying optical parameters of the small animal or object being imaging.

CHAPTER 6

BIOLUMINESCENT IMAGING AND TOMOGRAPHY

The previous chapters have presented the theory behind imaging light travelling through tissue and compressive sensing, as well as the development of a hyperspectral optical imaging system. The work presented in this chapter was presented in the published article: Single Pixel Hyperspectral Bioluminescence Tomography based on Compressive Sensing, Biomedical Optics Express (2019)[1] which shows some of the initial data taken using said system for 'proof-of-concept' purposes.

6.1. Introduction

By using the concept of CS, it is possible to create a new framework for both acquiring signals and how sensors are designed. If a signal is sparse or compressible, it is possible to acquire a signal with less samples than is classically suggested within the Nyquist-Shannon sampling theorem, which states there needs to be a minimum number of measurements taken to perfectly capture an arbitrary signal. Using this approach, rather than first sampling at a high rate and then compressing the collected data, it is possible to directly collect the compressed data. This enables a potentially

[1] https://doi.org/10.1364/BOE.10.005549

dramatic reduction in the sampling and computational costs of measuring signals that are sparse [172], as is the case in BLI and BLT.

Single-pixel imaging has been be used in a wide variety of applications as shown by Edgar et al [222], however is has not yet to date been demonstrated in BLT [223-225]. By applying the basis of CS to the application of BLT, it is possible to incorporate cheaper single dimensional (in space) detectors to allow for the collection of hyperspectral data. By using a single-pixel acquisition allows for the collection of hyperspectral data which in turn will potentially improve tomographic recovery, sensitivity and specificity particularly for multi-coloured sources which is the main motivation behind this work [17]. Collecting data this way would potentially bring improvements to the issues outlined, such as non-uniqueness and the bandwidth size, as these are both highly tuneable when using a spectrally resolved detector. This is a novel approach of hyperspectral imaging and has the potential to be faster and cheaper than existing hyperspectral cameras as these often use a line scanning method and can cost upwards of $50000. Existing schemes typically collect data using non-contact systems utilizing a CCD camera with filters which are pre-defined for wavelengths and to improve data acquisition typically have large bandwidths. Collecting hyperspectral data using existing schemes is unfeasible due to the length of time required, further motivating the proposed methodology. In this chapter, the development of a compressive sensing based hyperspectral Bioluminescence tomographic imaging system is presented. Preliminary results using this system are shown utilizing block and mouse phantoms containing single internal artificial light sources and multiple light sources of different wavelengths.

6.2. Theory

The theory involved in the capture of hyperspectral data and reconstruction of surface fluence images follows the theory presented in chapters 3 and 4. Fig. 6.1 shows different measurement matrices that can be used to collect the compressed data used for image reconstruction. The first column shows Bernoulli distributed random matrices with probability 0.5 and the second shows a binary pattern taken by sampling random rows of the Hadamard matrix. Both of these matrices have been shown to have both incoherence and meet the restricted isometry property, so can be used in this application [226]. The third column of Fig. 6.1, represents the patterns used when raster scanning the subject, where a measurement is taken for each pixel of the reconstructed image, hence taking full measurements and not utilizing CS. Further types of measurement basis can also be used such as wavelet, noiselet and speckle patterns depending on which basis the signal is sparse [222].

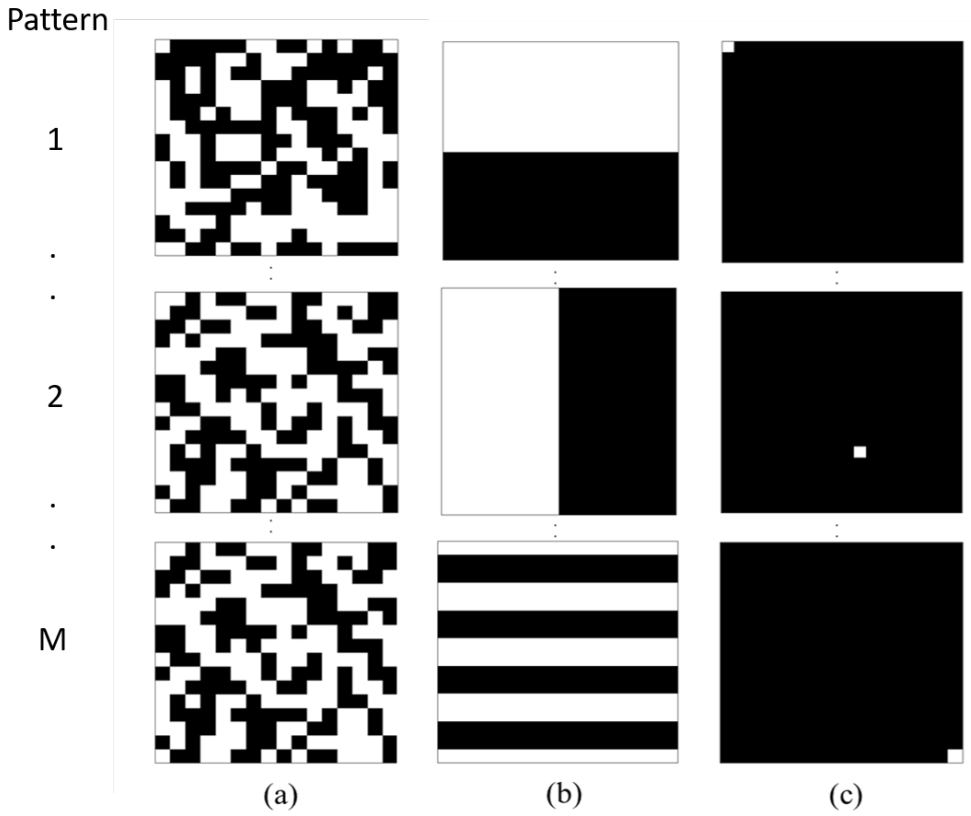

Figure 6.1. Examples of the different types of measurements matrices that can be used for image compression. (a) Randomly generated patterns with a Bernoulli distribution with probability 0.5, (b) Hadamard matrices and (c) a raster scanning method where the scene is scanned pixel by pixel by pixel.

6.3. Methods and results

6.3.1. Hyperspectral imaging system

Fig. 6.2 presents a schematic of the imaging system that has been developed which was extensively discussed in chapter 5, showing the different components that allow measurements from a sparse source distribution map. A Texas Instruments DLP Lightcrafter 4500 has been modified so that the digital micro-mirror device (DMD) within can be used to direct random projections of the imaging scene into a spectrometer. The DLP is modified by removing the three LEDs that are part of the

system and then attaching one end of an optical fiber in the LEDs place for detection. The optical fiber used in this work has a core diameter of 1000 µm. The DMD within the DLP has an array of 912 by 1140 micro mirrors that can be individually controlled to be in either an 'on' or 'off' position. This allows for random binary patterns to be created as shown in Figure 6.2(a). The spectrometer used in the system is a Flame S-VIS-NIR (OceanOptics), which has an optical detection range of 350 nm to 1000 nm with a spectral resolution of 0.4 nm, which is suitable as the wavelengths detected for a typical BLI are typically around 600 nm. It contains a 200 µm slit and uses a Sony ILX511B linear silicon CCD array to detect the incident light. Both the DLP and the spectrometer are controlled using MATLAB that automatically collects data once the desired resolution, number of measurements and acquisition time have been selected. The system includes an adjustable stage that the object being imaged can be placed on to correct and set the imaging field of view and focus. The whole system fits within a custom made light-proof housing to eliminate any background light, increasing the signal-to-noise ratio

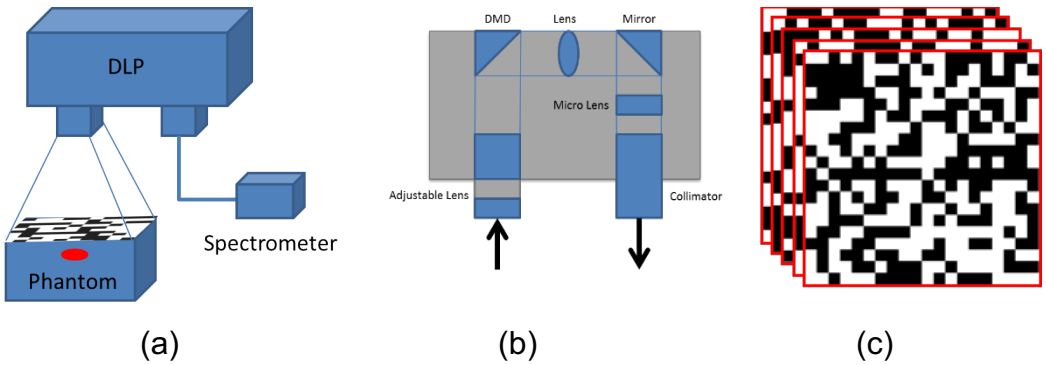

Figure 6.2. Optical system schematics (a) Schematic of the developed hyperspectral imaging system, (b) Schematic of the internal components within the DLP used and (c) the random binary patterns that are displayed on the digital micro-mirror device.

6.3.2. Effect of the number of measurements on image reconstruction accuracy

An experiment was undertaken to demonstrate the impact of the number of random patterns M, used in data collection on the accuracy and quality of the image reconstructions. Spectral data was collected as described above. The imaged object was a block phantom (Biomimic, INO, Quebec, Canada) of dimensions 33 × 26 × 40 mm. The phantom is made of a solid plastic with homogeneous spectrally-varying optical absorption and scattering properties that have been characterized within the range of 500 to 850 nm in terms of the absorption coefficient, μ_a = [0.007 – 0.12] mm^{-1}, and the reduced scattering coefficient, μ_s' = [1.63 – 1.79] mm^{-1} [227]. The phantom body contains two tunnels with a diameter of 6 mm at depths of 5 mm and 15 mm in which rods of matching optical properties to the background can be inserted to create a solid homogeneous phantom. A rod containing a light source was made that can be inserted into either of the two channels to mimic a bioluminescent light source. The light source used to mimic in-vivo bioluminescence in the experiment was a standard 5 mm LED (Arduino), with the emission spectrum being a Gaussian-like curve with a central peak at 620nm and a full-width-half-maximum of ~20 nm, meaning it has a similar spectral profile to a typical bioluminescent reporter such as Fluc.

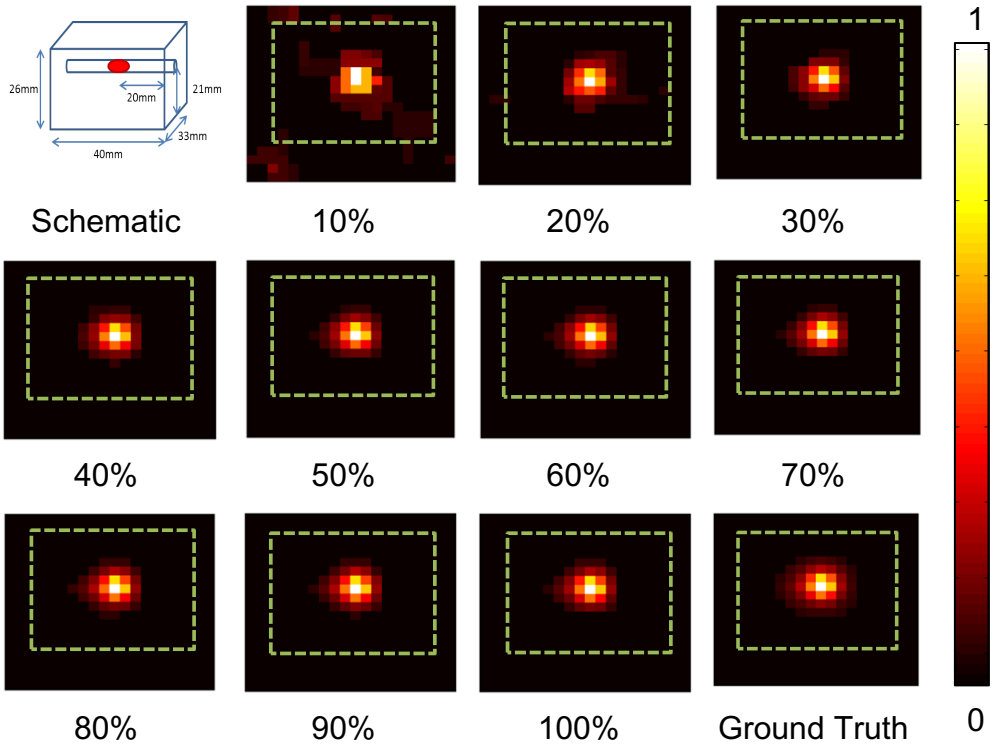

Figure 6.3. Schematic of the phantom setup and the reconstructed surface fluence images for the number of measurements (as a percentage of total pixels) used for reconstruction at 620 nm. Green dashed line represents the outline of the phantom. The 'ground truth' image was measured using a raster-scan of 400 measurements.

For the experiment the light source was placed at a depth of 5 mm inside the block phantom. This was then imaged by sequentially collecting the spectral data of the imaging scene convolved with a series of binary patterns that are displayed on the DMD within the imaging system at an acquisition time of 200 ms per pattern. The binary patterns used in this experiment are a series of 400 randomly generated 20×20 pixel patterns made up of ones and zeros. After the spectral data had been collected a total variation minimizing algorithm [201] was used to reconstruct images of the surface light fluence of the phantom using 10% to 100% of the total amount of measurements M, at a wavelength of 620 nm with a bandwidth of 5 nm. The percentage of measurements used for reconstruction is a percentage of the total amount of pixels of the

reconstructed image, for example when reconstructing a 20×20 image reconstructing using 10% measurements will be using 40 measurements (Number of patterns required in practice is highly dependent on the sample being measured). The reconstructed images were exported in Tagged Image Format (TIF) and the recovered photon intensity as a function of number of measurements used is shown in Fig. 6.3. It is clear from the images that as the number of measurements used for reconstruction is increased, they more closely represent the ground truth, which is captured using a raster scanning method (i.e. 400 individual measurements for each pixel).

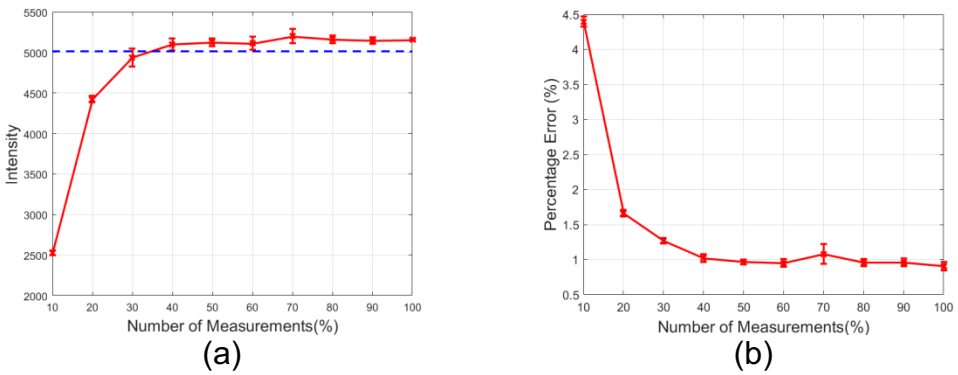

Figure 6.4. Analysis of reconstructions with changing number of measurements (a) Maximum reconstructed value for the number of measurements used for reconstruction (solid red) and the maximum value for the ground truth (dashed blue). (b) The percentage error between the reconstructed images and the ground truth for the number of measurements taken.

To better represent the accuracy and quality of the surface fluence reconstructions, the detected maximum intensity of the signal for each image presented in Fig. 6.3 is plotted in Fig. 6.4(a) with respect to the percentage number of measurements used, as compared to the full raster scan 'Ground Truth' image. Data collection was repeated four times in all experiments and the standard deviation of the data is shown in the error bars. It can be seen that when using a low number of measurements (<30%, M

< 120) the maximum intensity is lower than the ground truth, whereas at higher number of measurements (>30%) the maximum intensity asymptotes at a value similar to the ground truth. The percentage error of the reconstructed images as compared to the ground truth has also been plotted as a function of the number of measurements used for reconstruction in Fig. 6.4(b). It can be seen that at a similar point as the asymptote in Fig. 6.4(a), there is an asymptote at a percentage error of ~1%. These findings have shown that it is possible to reconstruct an image of the fluence data at the surface of the subject, using as low as 30% of the total number of measurements taken when using a standard raster scanning method whilst maintaining quantitative accuracy. However, for the remainder of this work, a total of 50% (i.e. M = 200) of measurements will be used.

6.3.3. Effect of the measurement matrix 'fullness' on image reconstruction accuracy

A second experiment was undertaken to demonstrate the effect of the 'fullness' of the measurement matrix used to collect the spectral data. Although the effect of fullness of the pattern has been previously investigated in depth, this effect has not been investigated for random patterns [228]. The term 'fullness' describes the percentage of 1's used in the binary patterns that are displayed on the DMD within the system, Fig 6.1(a), which is achieved by adjusting the parameter p of the Bernoulli distribution used as described in chapter 4. The term 'fullness' used in this work is only applicable to the random binary patterns used as this is not switchable for other well-defined basis. Increasing the 'fullness' of the measurement matrix will improve the signal-to-noise ratio that is obtained as it increases the amount of spatial information being sampled,

however it may affect the quality of the reconstructions of the surface fluence. For this experiment the setup is the same as in the previous section where a tissue mimicking block phantom is used with an LED of peak wavelength of 620 nm as the light source. Spectral data of the imaging scene as obtained with the binary patterns was collected as before. The light source was placed at a depth of 5mm and the spectral data was collected using M = 200 (i.e. 50% of total measurements) 20×20 binary patterns at an acquisition time of 200 ms per pattern, which were then repeated for varying measurement matrix 'fullness'. The same total variation minimizing algorithm was then used to reconstruct images of the surface fluence with varying 'fullness' at 620 nm with a bandwidth of 5 nm. The reconstructed images were exported in TIF and the detected photon intensity as a function of number of measurements used is shown in Fig. 6.5.

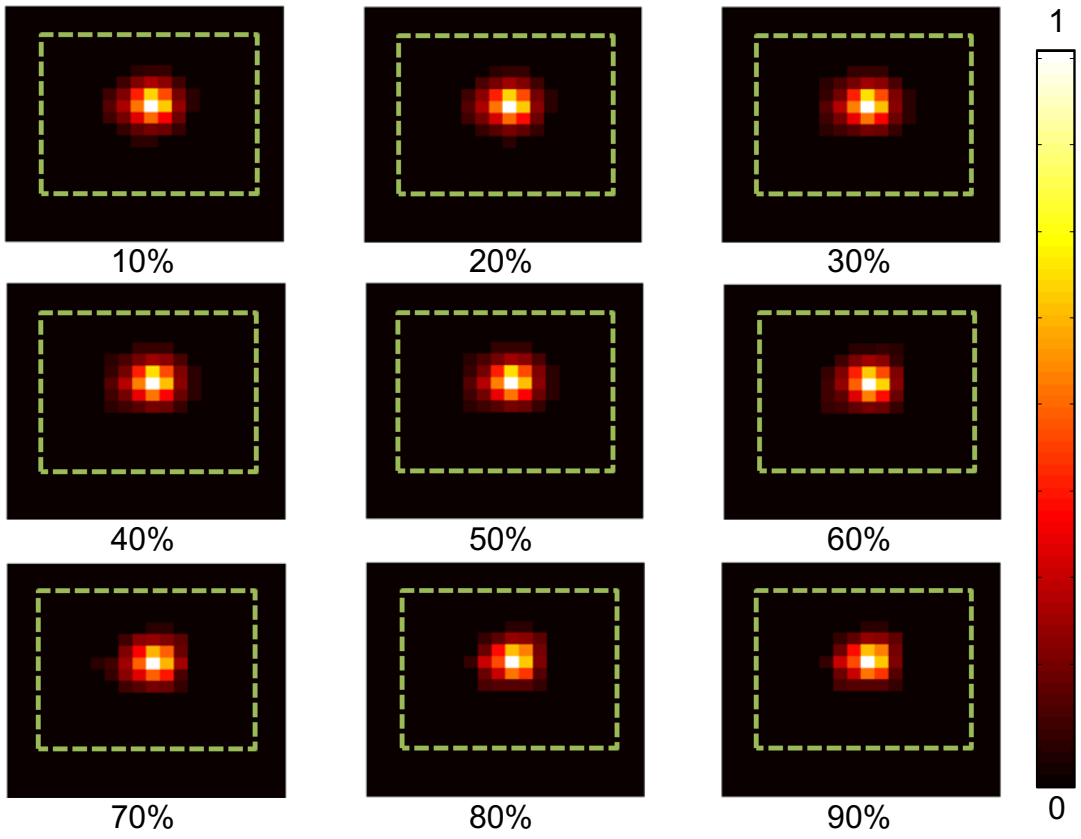

Figure 6.5. The surface fluence images reconstructed at a wavelength of 620 nm for different measurement matrix 'fullness'. Green dashed line represents the outline of the phantom.

From the images it can be seen that there is little qualitative differences in the reconstructions between different matrix 'fullness', with slight variations apparent in the higher 'fullness' percentages (70%-90%).

To quantitatively analyse the images, the maximum reconstructed intensity is plotted in Fig. 6.6(a) with respect to the matrix 'fullness'. It can be seen that the maximum intensity of the reconstructions closely resembles that of the ground truth at 10% up to 60%, after which, the variation in the reconstructions become large. It is believed that this relationship is due to sparseness of the measurement matrix and not meeting the restricted isometry property (RIP) that is required for a compressive sensing based method to work. To further quantitatively analyse the images, the

percentage error as compared to the ground truth (as from Fig. 6.3.) is plotted in Fig, 6.6(b) with respect to the matrix ‘fullness’. The same pattern as with the maximum intensity can be seen, where the error is constant at 1% for the lower percentage ‘fullness’, whereas at a matrix ‘fullness’ of >60% the percentage error of the reconstructions increases and the quality decreases. Finally, the peak signal-to-noise ratio (SNR) of the measured data is plotted in Fig. 6.6(c) with respect to the measurement matrix ‘fullness’. It can be seen that the SNR of the measured data increases linearly as the matrix ‘fullness’ increases as would be expected. However, due to the effects of higher percentage ‘fullness’ on the maximum intensity and percentage error, the increase in SNR does not provide a benefit in image reconstruction. These findings however are case specific due to the reconstruction quality being dependent on the size and sparsity of the signal, therefore greater or less sparse signals will show different reconstruction qualities.

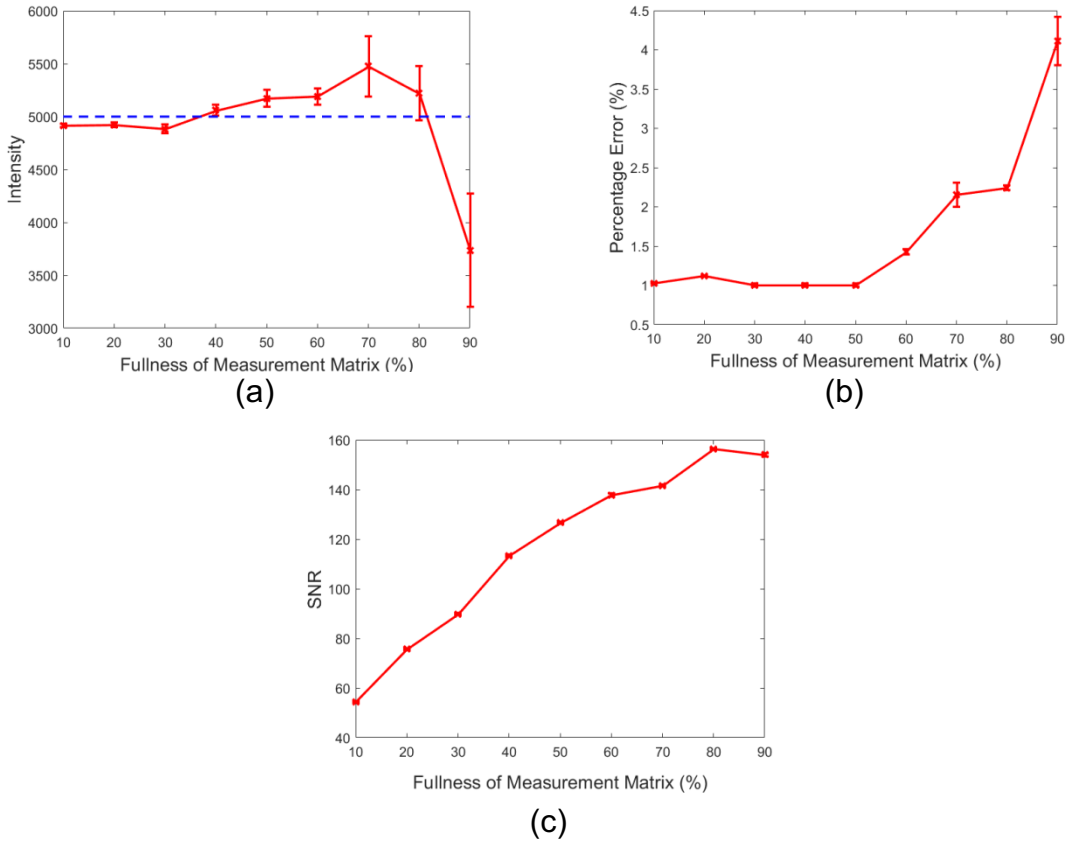

Figure 6.6.Analysis of reconstructions with changing measurement matrix 'fullness'. (a) Measured maximum reconstructed value for the measurement matrix 'fullness' used for reconstruction (solid red) and the maximum value for the ground truth (dashed blue). (b) The percentage error between the reconstructed images and the ground truth for the measurement matrix 'fullness' used for reconstruction. (c) The signal-to-noise ratio obtained for each measurement matrix 'fullness' used.

6.3.4. Tomographic reconstruction using a tissue mimicking block phantom

Using the information gained from the analysis of the data collected in the previous two sections, an experiment was performed to tomographically reconstruct the spatial light distribution of a light source within a tissue mimicking block phantom. Using the same optical setup as defined previously, spectral data was collected sequentially using M = 200 (50% of total pixels) binary patterns with 'fullness' of 50% and an acquisition time of 200 ms. Surface fluence images of the phantom at four different wavelengths (610 nm, 620 nm, 630 nm, and 640 nm) were reconstructed using the same total variation

algorithm as used previously. The wavelengths were selected with a bandwidth of 10 nm and covered the majority of the emission spectrum of the LED being used. The images were then registered to a model of the phantom using the known position of the phantom in the imaging plane and normalized. The fluence images were then used together with NIRFAST which is an open-source Finite Element model-based image reconstruction package for diffuse optics and molecular imaging (www.nirfast.org). Within the NIRFAST, a compressive sensing based optimization algorithm has been developed that uses a forward model of light propagation through the phantom based on the diffusion approximation of the radiative transport equation [130, 202]. The solution found is the spatial distribution of the light source and can be visualized as 2D cross-sections of the 3D model, Fig. 6.7.

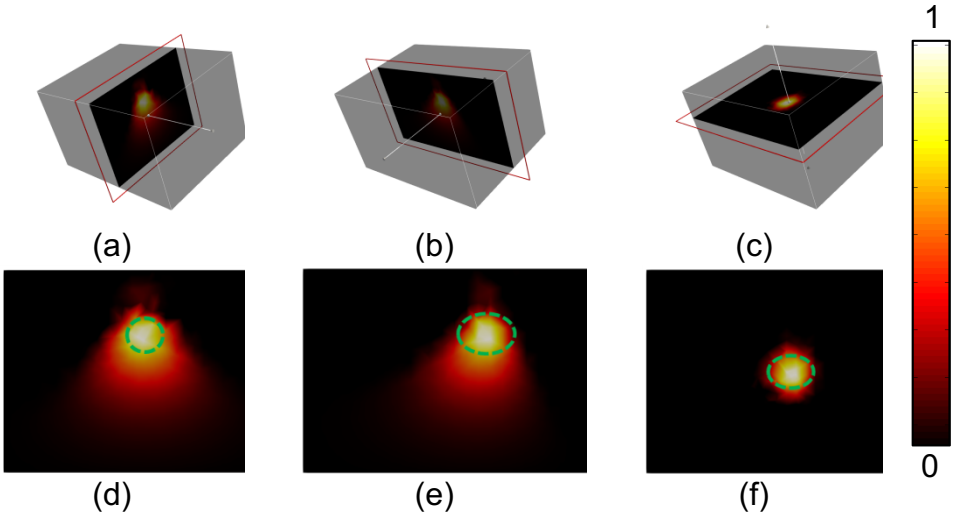

Figure 6.7. 2D cross-sections of the tomographic reconstruction of a 620nm LED within the block phantom from the (a, d) front view, (b, e) side view and (c, f) top view.

Qualitatively there is good accuracy in the localization of the source in the reconstruction as compared to the ground truth. To quantify the accuracy of the

reconstructions, firstly the volume of the source was calculated at full width half maximum and secondly the location of the center of mass of the source was calculated, Table 6.1.

Table 6.1. The expected and measured volume of the internal light sources and the localization error of the reconstructed sources.

	Actual Volume (mm^3)	Measured Volume (mm^3)	Localization Error (mm)
Block Phantom	137.0	72.0	4.0
Mouse Phantom	50.2	54.7	3.7
Block (RED)	137.0	88.5	3.0
Block (GREEN)	137.0	123.0	2.7

6.3.5. Tomographic reconstruction using a tissue mimicking mouse phantom

To demonstrate the application of this technique on a more geometrically realistic model, a mouse shaped phantom (XFM-2, Perkin Elmer Inc., Waltham, MA, USA), Figure 6.8(a), embedded with an optical fibre connected to an Ocean Optics HL-2000 halogen light source to mimic a light source with dimensions of 4 mm x 4 mm x 4 mm and a peak emission of 620 nm, Figure 6.8(b). The phantom is made from polyurethane material that includes scattering particles and dye to simulate the optical properties of live tissue, which have been characterized to have an absorption coefficient, $\mu_a \approx 0.01$ mm^{-1} and a reduced scattering coefficient, $\mu_s' \approx 1.5$ mm^{-1} at a wavelength of 600 nm. The light source was placed in a channel within the phantom at a depth of 10mm. Hyperspectral emission data due to the light source at the surface of the phantom was collected using the same method as described previously, with M=200, 20×20 pixel binary patterns with a 'fullness' of 50% and an acquisition time of 200ms. Surface

fluence images were reconstructed from the data at four wavelengths (610 nm, 620 nm. 630 nm and 640 nm) with a bandwidth of 10 nm, which were then normalized and registered to a model of the phantom, for tomographic reconstruction, Fig. 6.8(a).

The 3D spatial light distribution was reconstructed from the recovered surface fluence using NIRFAST utilizing the same compressive sensing based optimization algorithm as in the previous section. The raw reconstructed surface fluence image at 620 nm and the tomographic reconstruction of the light source are shown in Fig. 6.8. It was found that the spatial distribution of the light source was reconstructed with good localization (<3 mm) and volume accuracy, Table 6.1.

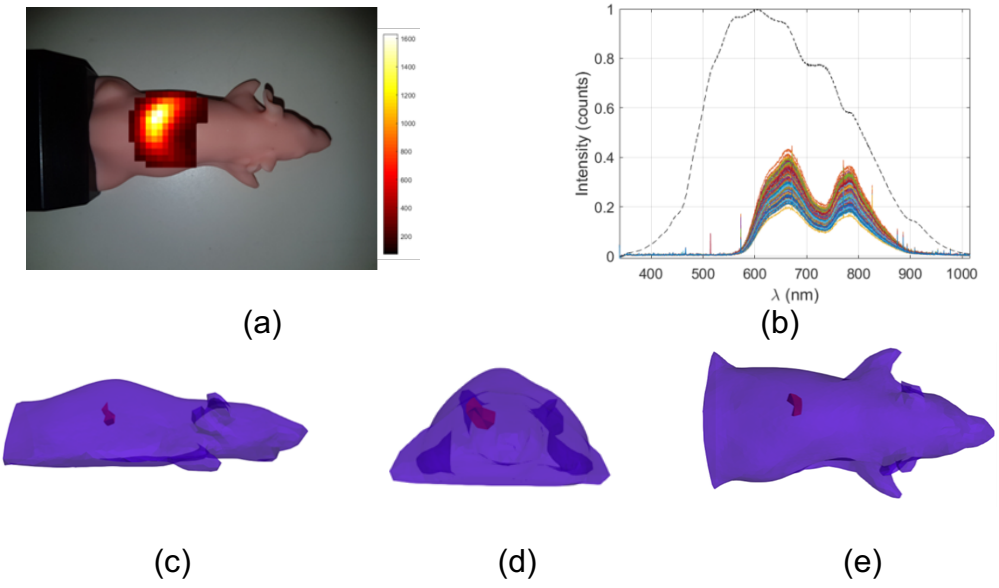

Figure 6.8. Reconstruction of a light source within a homogenous mouse phantom. (a) Overlaid image of the recovered surface fluence of the fibre light source inside the mouse shaped phantom. (b) The hyperspectral data collected from the mouse phantom, each coloured line represents a measurement using one pattern, the black dashed line represents the emission spectrum of the internal light source. Tomographic reconstruction of the light source from the (c) side, (d) front and (e) top.

6.3.6. Tomographic reconstruction of multiple sources of different wavelengths

A final experiment was undertaken to demonstrate an additional and otherwise difficult benefit of collecting hyperspectral data, for the reconstruction of the spatial light distribution of multiple light sources with different peak emission wavelengths using the same data set. The imaged object in this experiment was the block phantom used previously. Two different LEDs (Arduino) were used as a light source, one with a peak emission 620 nm (Red) and one with a peak emission of 510 nm (Green). Data was collected using the same method as before, by measuring the spectral data of the surface emission due to the light source using a sequence of M=200 20×20 binary patterns of 50% 'fullness' and an acquisition time of 200ms. Surface fluence images were reconstructed from the spectral data at four different wavelengths for each source, which were 500 nm, 510 nm, 520 nm and 530 nm for the green source and 610 nm, 620 nm, 630 nm and 640 nm for the red source, all with a bandwidth of 10nm, achieved by adding bins from the spectrometer 5 nm each side of the central wavelength. The reconstructed fluence images were normalized and registered to a model of the phantom and the internal spatial light distribution was then reconstructed as before. A RBG colour image of the emission of the light sources at the surface of the phantom and the raw spectral data collected are shown in Fig. 6.9 as well as the reconstructed spatial light distribution of both sources. It can be seen that both light sources are reconstructed with good localization and volume accuracy, Table 6.1.

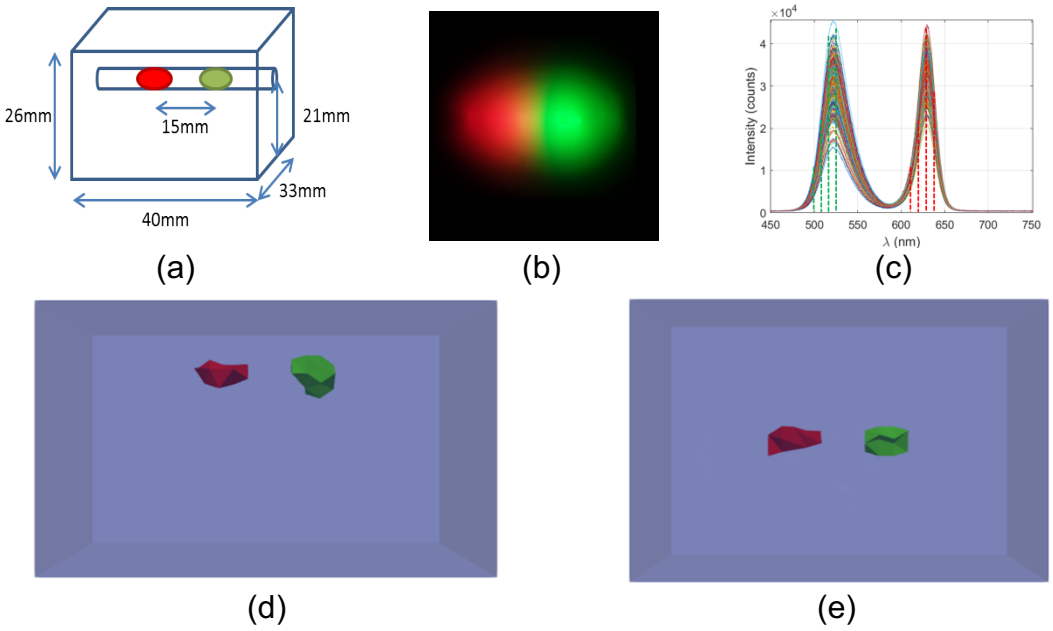

Figure 6.9. Reconstruction of multiple sources of different wavelengths simultaneously. (a) Schematic of the phantom setup. (b) RGB colour image of the reconstructed surface emission due to the internal LEDs. (c) Emission spectra of the red and green LEDs, the dashed lines represent the wavelengths that measurements were taken for tomographic reconstruction. Each curve represents a measurement taken with an individual random binary pattern. Tomographic reconstructions of the green and red LEDs from the (d) side and (e) top.

6.4. Discussions

The number of spectral measurements used to reconstruct an image of the emission at the surface of object due to an internal light source using a compressive sensing method, as described in this paper can greatly affect both the qualitative and quantitative accuracy of the reconstructions, Fig. 6.2. As described in literature, the minimum number of measurements required to accurately represent an image depends on both the number of pixels in the image and the underlying sparseness of the image [17]. In the experiments displayed within this work, using a typical example of an internal light source, it was found that the surface fluence of the light source could be accurately reconstructed to within 1% error of the ground truth using as low as 30%

of the total number of pixels reconstructed in measurements. To further demonstrate the effect that the number of spectral measurements has on the accuracy of image reconstruction, the maximum intensity of the reconstructed value was evaluated against the number of measurements. It was found that the recovered maximum value was comparable to that of the ground truth when only 30% of the total measurements were used for reconstruction. This reduction in number of measurements directly relates to an imaging time that is at least 30% (due to increase SNR as compared to single pixel raster scanning) of the time taken in order to collect the same data using existing methods for hyper-spectral imaging, such as raster scanning. In pre-clinical studies it is common practice to associate the total count in intensity to be proportional to the total amount of activity occurring, therefore it is important that there is no variation in the detected data. Due to these finding it was concluded that 50% of the total reconstructed pixels in measurements would be used for all proceeding reconstructions.

The ‘fullness’ of the measurement matrix used in data collection was shown to have an underlying effect on the quality of the surface fluence images reconstructed from the spectral data that was collected, Fig. 6.3. It was found that using a matrix ‘fullness’ of ≤50% resulted in reconstructions that were within 1% error of the ground truth whilst also showing comparable maximum reconstructed values. When the measurement matrix ‘fullness’ was >50% the quality of the reconstructions were seen to reduce and the maximum reconstructed value shown to fluctuate from the ground truth with greater variation in measurements. It is shown in literature that in order for a compressive sensing based method to successfully find the solutions to the underdetermined problem that is present, the measurement matrix has to meet the restricted isometry

property (RIP), which states that if the measurement basis of the matrix is too closely aligned to the sparsity basis of the measured signal it will be unable to detect the signal as there is no longer incoherence present [229]. This property is typically met by using a randomly generated measurement matrix, however as the ‘fullness’ of the measurement matrix increases the RIP is no longer holding due to the randomness of the matrices being reduced. It was also found that as the ‘fullness’ was increased, the measured peak SNR linearly increased. The benefit of a higher SNR however is not valid for this application as the variation and quality of the reconstructed images is of greater importance. Therefore, it was concluded that a measurement matrix ‘fullness’ of 50% would be used for all proceeding experiments.

Tomographic reconstructions were made using both a block phantom and a mouse phantom using the hyperspectral compressive sensing based system that has been developed, Fig. 6.4 and Fig. 6.5. It was found in both cases that the spatial distribution of the light source was reconstructed with both good localization and volumetric accuracy that is comparable to values quoted in literature [230]. Tomographic reconstructions of multiple sources of different wavelengths have also been shown to be possible from the same set of collected spectral data. In this experiment both sources were reconstructed with good localization and volumetric accuracy, however reconstruction of the green source appeared to be more successful. This is believed to be due to the optical properties of the phantom that are used within the reconstruction algorithm being more closely matched to the true values for the green wavelengths as compared to the red wavelengths, as the values for green wavelengths were obtained by extrapolating measured values of the red wavelengths. This highlights the importance of obtaining a-prior information regarding the optical

properties of the medium for in-vivo applications. It has previously been demonstrated that in a practical setting a multi-modal system [1] or atlas based information [13, 79] can be used to estimate the optical properties of the tissue being imaged.

Using this CS based method to collect hyperspectral emission data from the surface of the imaging subject has the potential to address a number of issues that have previously been raised in respect to BLI and BLT. Firstly, by collecting hyperspectral data, all in one collection strategy, can help address the issue of the variation in measured signal as a function of imaging time [13]. This method can also combat the issue of non-uniqueness in the solution as it has been shown that collecting multi-spectral data improves the accuracy of tomographic reconstruction [10]. It has been demonstrated in previous studies that using multiple views is beneficial when imaging deep in vivo sources [1, 13]. The method of data collection via compressive sensing as used in this work, is also applicable to multi view data collection and can be incorporated into system designs. There is the potential for the time taken for data collection of multi/hyperspectral data to be vastly reduced with this method. Another issue that can be addressed by this method is the effect of filter bandwidth on measurement as no filters are used [11]. The effective bandwidth of measurements taken using the developed system is limited by the spectral resolution of the spectrometer, so can be controlled better [11], and is a topic for future work. Moving forward, it has been shown that using the spectral derivative of the spectral data measured will eliminate the need for any system corrections or system models as light at similar wavelengths display near-identical system responses [13, 231]. This is also a future direction of development for the outlined imaging system, as this data can easily obtained from the hyperspectral measurements.

6.5. Conclusions

This chapter highlights the development of a hyperspectral compressive sensing based imaging system used for non-contact BLI and BLT. The effect of varying the number of measurements and 'fullness' of the measurement matrix has been explored and it has been shown that images made with 30% of the measurements taken in existing systems can be reconstructed with as little as a 1% error, as compared to the ground truth. The ground truth used in this work is collected using a pixel-by-pixel raster scanning scheme which is thought to provides definite information about each pixel in the image [222]. The system has also been shown to be able to carry out tomographic reconstructions using a mouse shaped phantom and a block phantom with both individual and multiple sources of two different wavelengths. Although the use of LED's for these experiments are providing signals much stronger than those from a bioluminescent source, this work has demonstrated the application of CS in BLT paving the way for further optimization of the system to deal with lower light levels as seen in pre-clinical studies. This could be achieved through the development of a unique detection system, rather than an adapted off-the-shelf projector, a more sensitive spectrometer and overall optimization of the system to minimize signal loss due to coupling of the DMD and spectrometer. The system can be optimized by first improving the optical fibre that collects the light from the DMD by increasing the diameter of the fibre, decreasing the length of the fibre and decreasing its proximity to the DMD. A DMD that is optimized for better reflection with visible/NIR should also be used. Lenses with better transmission and shorter focal lengths will reduce the imaging distance, as for example a factor of 4 reduction in imaging distance will result in a factor of 16 increase in signal. Finally, the spectrometer can also be configured to use a lower

spectral resolution such as 2nm instead of 0.3nm to improve detection sensitivity. All of these improvements will be made as well as optimizing the coupling efficiency of the optical fibre to the luminescent source. The use of adaptive patterns can also be explored to further speed up data collection whereby knowledge of the domain being imaged can be utilized [228]. These may provide a hyper-spectral system at a resolution not yet achieved, at potentially a lower cost, which will be applicable to multi-marker imaging in pre-clinical studies. As the proposed CS based system utilizes a 'single' pixel detection, the effective area for sensing light can be seen to increase as compared to utilization of a multi-pixel camera, providing better SNR at lower light levels which will be subject of further investigation.

The following chapters introduce the development of a dual-parameter reconstruction algorithm that can be used to simultaneously recover both source location and underlying optical parameters, without the need for a priori knowledge.

CHAPTER 7

COMBINED BLT/DOT

The previous chapter presented the initial data that was collected to validate the hyperspectral imaging system that was developed. The work presented in this chapter was presented in the published article: Simultaneous diffuse optical and Bioluminescence tomography to account for signal attenuation to improve source localisation, Biomedical Optics Express (2020)[2], which follows the development of a dual parameter recovery algorithm that takes advantage of techniques discussed in chapters 3 and 4 to account for the optical properties of an animal whilst simultaneously recovering the source location.

7.1. Introduction

Pre-clinical photonics-based imaging is a powerful non-invasive technique that is used widely to obtain biologically relevant information. An example of this is Bioluminescent Imaging (BLI), where light from distributed biological visible and near-infrared luminophores are detected at the surface of a subject [1]. However, current limitations of BLI include poor spatial resolution, poor depth sampling and low quantitative accuracy which is due to the often low signal intensities, non-linear signal attenuation and the unknown underlying tissue optical parameters.

- [2] https://doi.org/10.1364/BOE.401671

When requiring to move to a more quantitative measurement, a method can be employed to allow for the recovery of spatially resolved tomographic maps of the source location and intensity, known as Bioluminescent Tomography (BLT) [9]. BLT utilizes a ‘forward’ model of light propagation within an optically diffuse medium, along with an optimization recovery ‘inversion’ algorithm to accurately reconstruct both the spatial and intensity distribution of the underlying light source.

One of the main limitations that has often been largely ignored is the need for accurate measurements of the underlying optical parameters of the tissue being imaging [232]. Previous work has aimed at accounting for signal attenuation through the use of multi-modal systems that incorporate techniques such as Diffuse Optical Tomography (DOT) (Chapter 3) to non-invasively obtain the molecular chromophore concentrations as well as spectrally and spatially resolved optical parameters [1]. By using such a system issues arise, mainly through the time required to collect the data through the use of spectral filters along with a high spatially resolved CCD camera. To date several strategies both experimental and computational have been employed to improve the accuracy of BLT, including the use of computational models that incorporate permissible regions into the reconstructions. These permissible regions can be defined in multiple ways, for example setting values outside of a specific region to 0 [233], using iterative methods to reduce the area of the permissible region [234], and using structural information gained from other imaging modalities such as MRI [235], CT [76] and Ultrasound [236] to improve the reconstruction quality as described in chapter 2. All of these methods, through either using a multi-modal system or through the use of permissible regions have been shown to significantly improve the accuracy of the results, quoted to be up to 25% in certain cases [236].

Here a novel algorithm is presented, allowing for the simultaneous recovery of chromophore concentrations and optical parameters to aid with accurate localization of the underlying spatial bioluminescence source distribution. This is achieved directly using the same hyperspectral data from the bioluminescence source that can be collected using a hyperspectral imaging system, giving the potential for more accurate localization along with a massive reduction in the time spent collecting data.

7.2. Theory

When developing the methodology and framework for data collection as used in this work, several existing algorithms need to be considered. Firstly, a method of obtaining surface fluence data is required. This can be done using a basic camera-based system as described in chapter 2 or through the use of the novel hyperspectral imaging system as presented in chapters 5 and 6 of this thesis. The second part of the problem requires an algorithm to tomographically reconstruct the spatial light distribution from the measured surface fluence data as well as the underlying optical parameters of the subject. Both can be achieved through the theory presented in chapters 3 and 4.

The ultimate algorithm needed to complete the entire framework is one that calculates both the optical properties, given the surface fluence data at multiple wavelengths, as well as the location of the source within the subject. The first (unknown optical properties) is Diffuse Optical Tomography (DOT), as presented in chapter 3. A software package, Near Infrared Fluorescence and Spectral Tomography (NIRFAST) [130], is used to allow for the simulation of light propagation within biological tissue using a finite element method (FEM) and is also well documented elsewhere. Within the package are a number of forward and inverse models, however

a specific spectrally constrained case is utilised in this work. The algorithm has been modified to take the internal bioluminescence source location and surface fluence data with the goal of directly estimating the concentrations of oxy-haemoglobin, deoxy-haemoglobin and water, as well as scattering power and amplitude [164, 237]. The assigned chromophore concentrations can be used to calculate the underlying wavelength dependent absorption coefficient of tissue through the use of extinction coefficients of individual chromophores. This can similarly be done using the scattering power and amplitude to obtain a corresponding reduced scattering coefficient at each wavelengths using Mie scattering theory. Using a continuous wave model, the Jacobian is calculated and then inverted using the Moore-Penrose pseudoinverse which is typically more suitable towards underdetermined problems [159]. The Moore-Penrose pseudoinverse finds the 'best fit' or minimum norm solution to a system of linear equations, the implementation of which have been extensively detailed elsewhere [130, 159]. From this an update in optical properties is calculated and the whole process is repeated, new boundary data is simulated and compared with the original data in order to calculate a projection error. This error is then used as a stopping mechanism for when it is considered that convergence has occurred, typically within 2% change. The Moore-Penrose pseudoinverse applied uses a starting value of 0.1 for the regularisation parameter as defined in equation 3.10, which is the standard value used as detailed elsewhere [130].

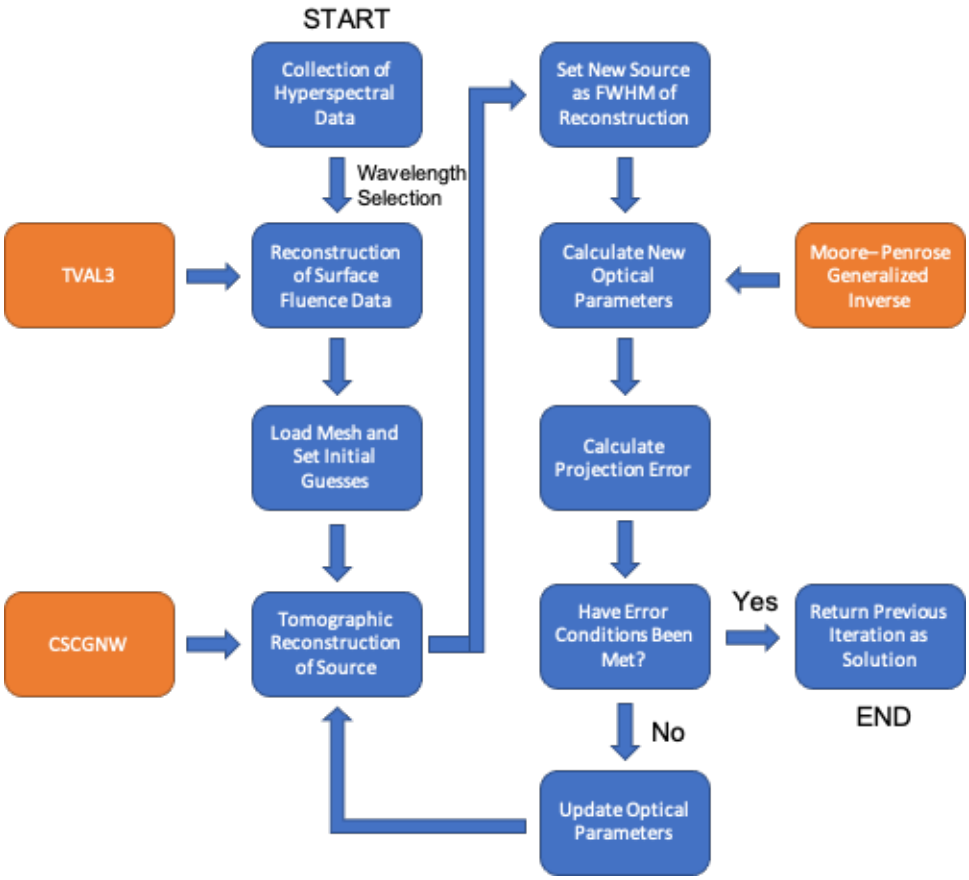

Figure 7.1. A flowchart of the simultaneous source and optical parameter recovery algorithm. Blue steps represent part of the created algorithm and orange steps represent existing algorithms being used.

Figure 7.1 is a flowchart showing the sequence of the new iterative algorithm that has been developed by utilising all of the algorithms previously described. Firstly, hyperspectral data is collected using either simulations within NIRFAST or through the collection of real data using a hyperspectral imaging system as described. From this data the desired wavelengths are selected and surface fluence data is calculated and combined using the TVAL3 algorithm described in chapter 4. This data, along with an initial 'guess' of underlying optical properties, tomographic reconstruction of the spatial light distribution is achieved using the CSCGNW algorithm described in chapter 4. A

new source position is set and then through the DOT algorithm, using the same data-set, optical properties of the medium are calculated. From this, if the error conditions have not yet been met, the optical properties are updated by the average value across the entire mesh or of a particular pre-defined volume within. Using these updated optical properties, the CSCGNW algorithm is then used again to reconstruct the new spatial light distribution and whole process is completed iteratively. As with the inverse problem outlined above a stopping condition is put in place to stop the algorithm when it is considered to have converged. The stopping criteria is the same as that used in the DOT algorithm whereby a projection error is calculated between the original and modelled data using the updated optical properties. The iterative process is continued until the change in projection error is below a tolerance which is typically set to 2%.

When modelling the new source for the update of optical parameters, two different methods can be used. Firstly the tomographically reconstructed source is represented as its full-width-half-maximum (FWHM) and the centre of mass is set as the new point source. Another method is to also represent the reconstructed source as a distributed source, at the recovered FWHM, where the entire distributed source can then be set as the new update. Doing this gives a more realistic representation and therefore may result in more accurate results, both methods are investigated as part of this work.

7.3. Methods and results

7.3.1. 2D Numerical Experiment

Reconstructions from simulated data using a homogenous 2D circle model were carried out to initially demonstrate that the algorithm is capable of successfully reconstructing the spatial light distribution located within the model. The circular mesh

had a diameter of 50 mm and a source of radius 1.5 mm was placed within the mesh at a depth of 10 mm from the top surface, as can be seen in Fig. 7.2(a).

The optical properties and chromophore concentrations of the mesh were set to that of adipose [130], being 0.012 mM and 0.005 mM for oxy- and deoxyhaemoglobin respectively, 40% water and a scattering power and amplitude of 0.56 and 1.34 respectively. Data from the light source was simulated at 4 wavelengths (600 nm, 610 nm, 620 nm and 630 nm) using an array of 20 detectors evenly distributed across the top half of the mesh. Figure 7.2(b) shows the tomographic reconstruction of the spatial light distribution using the known optical properties and chromophore concentrations of the mesh, representing the gold standard method of reconstruction.

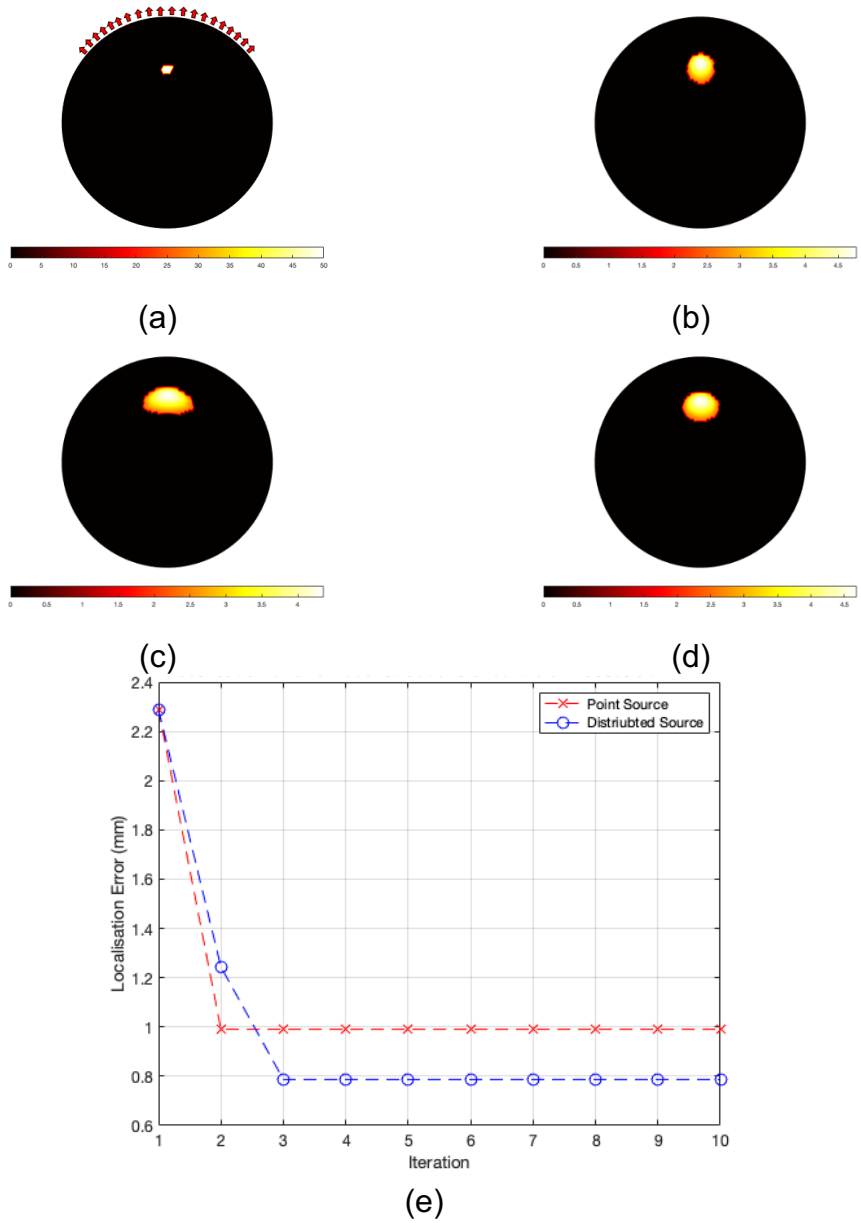

Figure 7.2. Reconstructions of simulated 2D homogenous circular phantom data and analysis. (a) The ground truth location of the light source inside a circle phantom, red arrows represent detector positions. (b) Tomographic reconstruction using the ground truth optical parameters. (c) Tomographic reconstruction of the light source using the initial optical parameter guess. (d) The final tomographic reconstruction of the light source after the error conditions have been met. (e) The localization error between the centre of mass of the light source at FWHM and the ground truth location

For the simultaneous parameter recovery, the initial guesses of optical properties were set to 0.01 mM for both oxy- and deoxyhaemoglobin and 40% for water. As a continuous wave method of calculating the optical properties is currently employed,

the scattering parameters are not included in the update and were therefore set to the ground truth values of 0.56 and 1.34 for scattering power and scattering amplitude respectively. Figure 7.2(c) shows the initial tomographic reconstruction using the set optical parameters, from which the iterative process of calculating the optical parameter updates and source localization begins. Two methods of representing the new source for each optical parameter update were used, the first being a point source located at the centre of the reconstruction at FWHM. The second method was representing the new source as the distribution of the reconstruction at FWHM. This iterative process continues until the stopping criteria set out in the previous section have been met, being the second iteration when using a point source and the third iteration when using a distributed source. Figure 7.2(d) shows the tomographic reconstruction at the third iteration when the source was modelled as the whole distributed source at FWHM. As can be seen in figure 7.2(e) the algorithm performs well in localizing the source, with a localization error of ~1 mm when using a point source and a better localization error of ~ 0.8 mm when using the entire distributed source. The localization error is a measure of the Euclidean distance between the reconstructed centre of mass (COM) and the known ground truth location, which is defined by:

$$L_{err} = \sqrt{(x_g - x_r)^2 + (y_g - y_r)^2 + (z_g - z_r)^2} \quad (7.\ 1)$$

Where x_g , y_g and z_g are the Cartesian coordinates of the ground truth location and x_r, y_r and z_r are the Cartesian coordinates of the reconstructed COM.

7.3.2. 3D Homogenous Numerical Mouse Model

The second set of simulations carried out were using a homogenous 3D mouse mesh of dimensions ~ 90 × 40 × 30 mm, which is based on the Digimouse model [238]. The optical parameters of this mesh were set to that of adipose as in the previous example, and a source of diameter 4 mm was placed in the centre of the mesh at a depth of 7.5 mm from the top surface, as shown in Fig. 7.3(b-c). Surface fluence data from the source was simulated at 4 wavelengths (600 nm, 610 nm, 620 nm and 630 nm) using a 5 × 5 detector array as can be seen in Fig. 7.3(a). The same process as with the 2D circle example in the previous section was carried out by first reconstructing the spatial light distribution using an initial guess of optical parameters and chromophore concentrations, as shown by the top view in Fig. 7.3(d) and the side view in Fig. 7.3(g).

The iterative process of the developed algorithm was then carried out using both methods of representing the new reconstructed source, as stated in the previous section. Figures 7.3(e) and 7.3(h) show the final reconstruction when the source was represented by a point source centred at the reconstruction at FWHM, whilst figures 7.3(f) and 7.3(i) show the final reconstruction when the source is represented as a distributed source at FWHM. As can be seen in Fig. 7.3(k), when the new source used for the optical parameter update is represented as a point source the best reconstruction localization error obtained is ~ 2.2 mm. However, when using the distributed source to obtain the new optical parameters the localization error is much lower at ~ 1.25 mm. Figure 7.3(l) shows the calculated FWHM and is show to be ~ 8 mm for both methods of reconstruction which is ~ 2 times that of the ground truth of 4 mm.

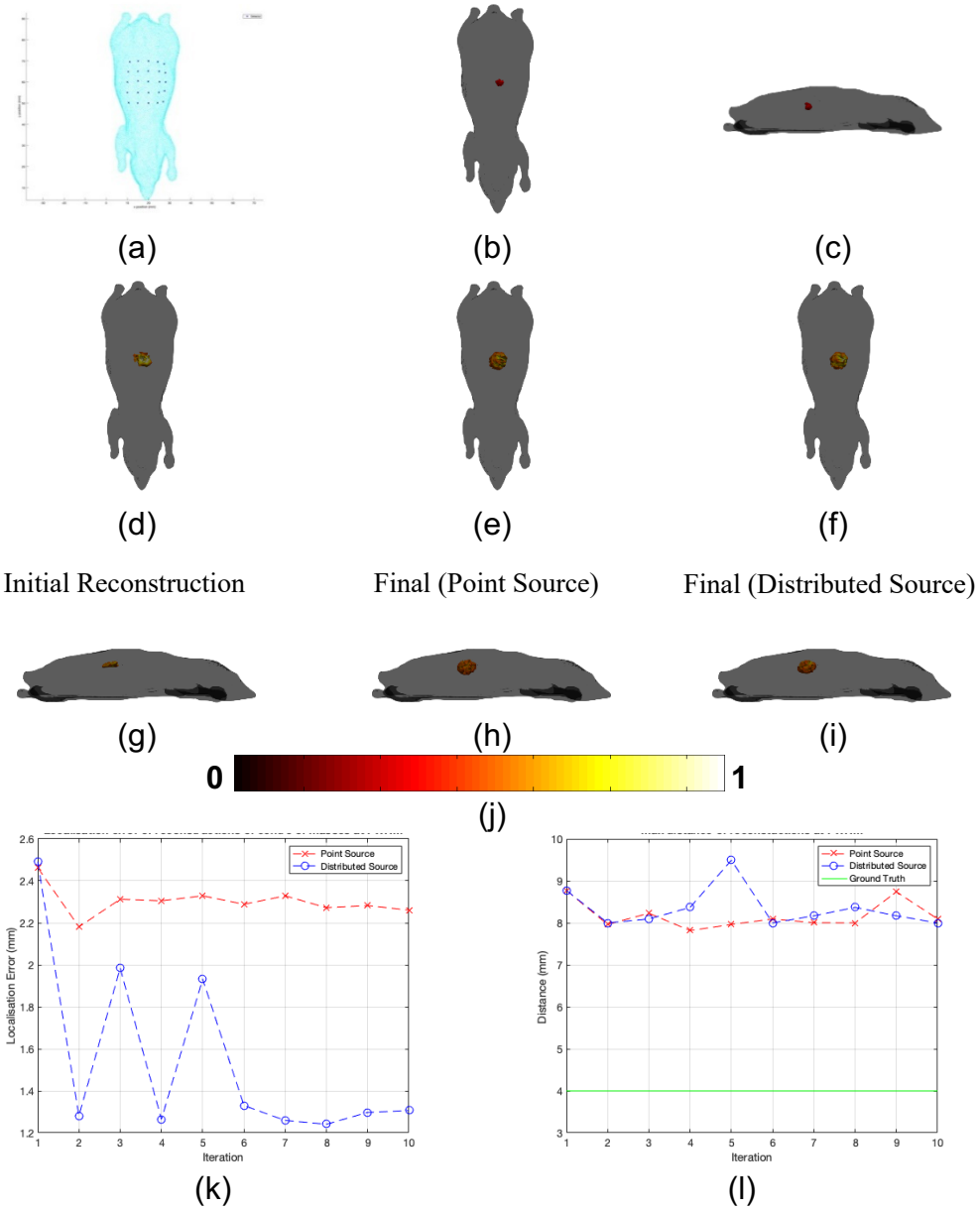

Figure 7.3. Reconstructions of simulated 3D homogenous mouse phantom data and analysis. (a) The homogenous mouse phantom used with the detector positions represented by crosses. (b – c) A top and side view of the ground truth light source placed within the phantom. (d – f) The top views of the initial iteration, final iteration using a point source and final iteration using the whole source reconstructions respectively. (g – i) The side views of initial iteration, final iteration using a point source and final iteration using the whole source reconstructions respectively. (j) The colourbar for all reconstructions excluding the ground truth. (k) The localization error between the centre of mass of the light source at FWHM and the ground truth location and (l) The FWHM of the recovered source. The red dashed line represents reconstruction carried out with the source modelled as a single point and the blue dashed line represents reconstruction carried out with the whole source at FWHM used. The green line represents the ground truth value.

7.3.3. 3D Heterogeneous Numerical Mouse Model

To demonstrate the use of this algorithm on a more realistic model, the same mouse mesh used in the previous section was converted into a heterogenous mesh by marking and setting the optical parameters of 8 separate regions across the mesh to represent different tissue types found in a mouse, table 7.1 [239]. Figure 7.4(a) shows a top down view of the heterogeneous mouse model with the different regions of optical parameter shown. A source of diameter 4 mm was then placed in the centre of the mesh at a depth of 7.5 mm which corresponds to a region within the mesh that represents the left kidney of the mouse which can be seen in Fig. 7.4(b-c). Surface fluence data was then simulated at 4 wavelengths (600 nm, 610 nm, 620 nm and 630 nm) using the same 5 $\times$ 5 detector array that can be seen in figure 7.3(a).

Table 7.1. The seven different regions that make up the heterogeneous mouse phantom used along with their corresponding chromophore concentrations and scattering properties [239].

Region	Total Hemoglobin (mM)	Oxygen Saturation (%)	Water Concentration (%)	Scatter Amplitude	Scatter Power
Adipose	0.0033	70	50	0.98	0.53
Bones	0.0049	80	15	1.4	1.47
Muscles	0.07	80	50	0.14	2.82
Stomach	0.01	70	80	0.97	0.97
Lungs	0.15	85	85	1.7	0.53
Kidneys	0.0056	75	80	1.23	1.51
Liver	0.3	75	70	0.45	1.05
Pancreas	0.3	75	70	0.45	1.05

The iterative algorithm was then used using initial optical parameters of 0.00231 mM and 0.00099 mM for oxy- and deoxyhaemoglobin respectively as can be seen in figures 7.4(d) and 7.4(g). The optical parameter updates were calculated using the same two methods of representing the new source as in the previous sections. During each update, instead of updating the global optical parameters as a homogenous model as

with the previous sections, spatial a priori knowledge about the different tissues were used. This is achieved by using a priori knowledge of the structure of the mouse to calculate an average of the reconstructed optical parameter for each region. Although such structural data is known in this example, in practice either registration to an atlas may be utilized or structural information from other modalities such as CT [76].

Figures 7.4(e) and 7.4(h) show the final tomographic reconstruction of the spatial light distribution when modelling the source used for the optical parameter update as a point source. Figures 7.4(f) and 7.4(i) show the final tomographic reconstruction of the spatial light distribution when modelling the source used for the optical parameter update as the whole distributed source at FWHM. It can be seen in figure 7.4(k) that the calculated localization error of the reconstruction is ~ 1.3 mm when a point source is used, whereas a slightly better localization error of ~ 0.9 mm when the distributed source is used. The recovered FWHM are displayed in Fig. 7.4(l) and it can be seen that a maximum of ~ 11.4 mm is present when a point source is used whereas a maximum of 4.6 mm is found when the whole distributed source is used for reconstruction, which is much closer to the ground truth of 4 mm.

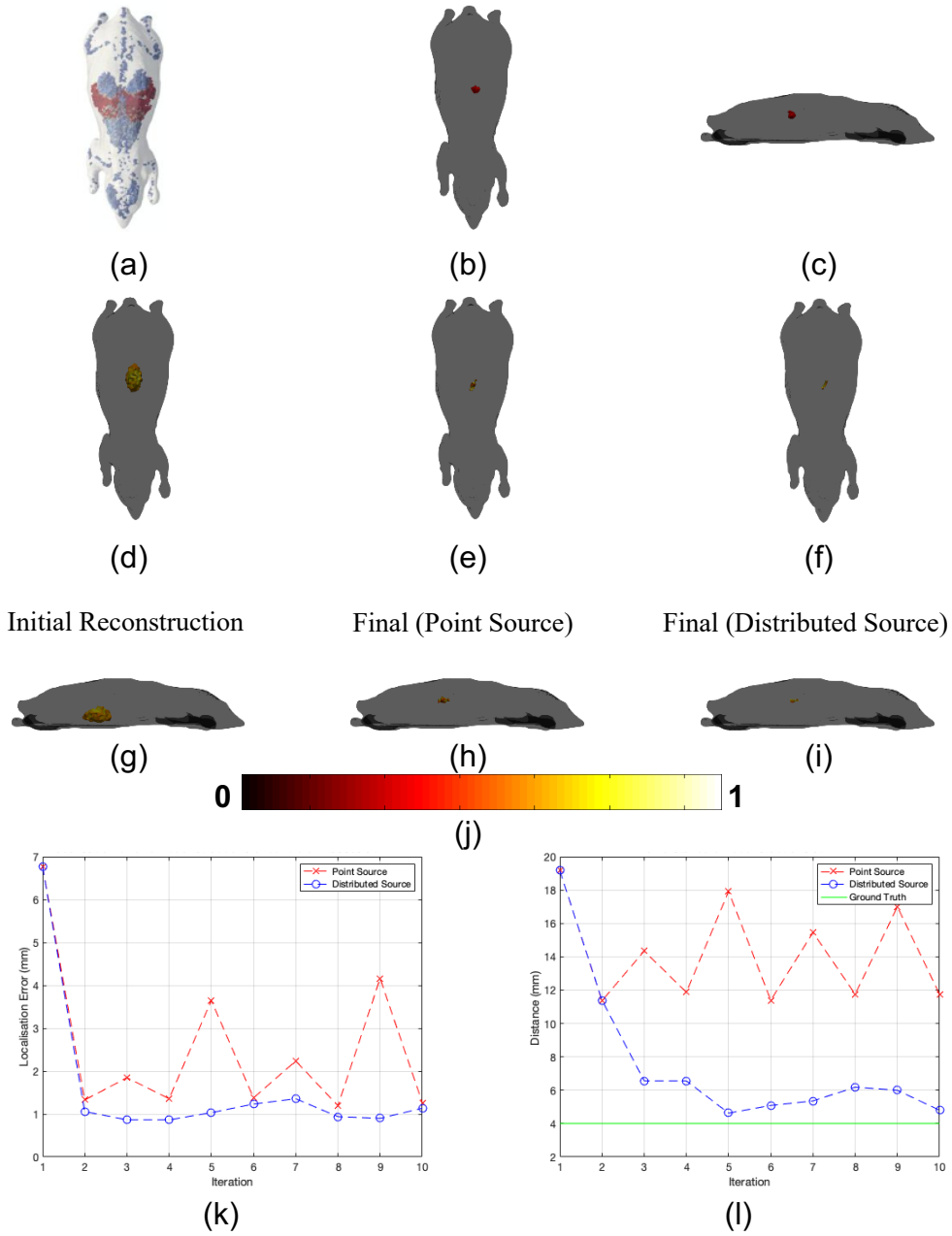

Figure 7.4. Reconstructions of simulated 3D homogenous mouse phantom data and analysis. (a) The heterogenous mouse phantom used with regions of varying optical parameters visible. (b – c) A top and side view of the ground truth light source placed within the phantom. (d – f) The top views of the initial iteration, final iteration using a point source and final iteration using the whole source reconstructions respectively. (g – i) The side views of initial iteration, final iteration using a point source and final iteration using the whole source reconstructions respectively. (j) The colour-bar for all reconstructions excluding the ground truth. (k) The localization error between the centre of mass of the light source at FWHM and the ground truth location and (l) The FWHM of the source. The red dashed line represents reconstruction carried out with the source modelled as a single point and the blue dashed line represents reconstruction carried out with the whole source at FWHM used. The green line represents the ground truth value.

7.3.4. Phantom Experimental Data

An experiment was carried out to further confirm and demonstrate the capabilities of the proposed algorithm. The imaged object for this experiment was a tissue mimicking block phantom (Biomimic, INQ, Quebec, Canada) of dimensions 33 × 26 × 40 mm. The phantom is made of a solid homogeneous plastic that has spectrally varying optical absorption and scattering properties. These properties have been characterized between the 500 to 850 nm and found to range from, μ_a = [0.007 – 0.12] mm^{-1} and μ_s' = [1.63 – 1.79] mm^{-1} for absorption coefficient and reduced scattering coefficient respectively [227]. The phantom also contains two tunnels with a diameter of 6 mm at depths of 5 mm and 15 mm in which rods of matching or varying optical properties can be inserted to create either a solid homogenous phantom, or a heterogeneous phantom. For the use in this study, a rod of matching optical properties containing an embedded red LED was created to allow it to be inserted into either of the channels to mimic an internal light source, such as a bioluminescent marker. The light source used is a standard 5 mm LED (Arduino) that has a gaussian like emission spectrum with a central peak at ~ 620 nm and a full-width-half-maximum of ~20 nm.

For this experiment, the light source was placed within the channel at a depth of 5 mm from the surface. The imaging system shown in section 7.3.1 was used to collect a hyperspectral data set. This was done by displaying a sequence of 50 randomly generated 10 × 10 binary patterns, for each pattern collecting spectral data for 200 ms. From this data, surface fluence images were reconstructed using a total variation minimizing algorithm (TVAL3) [201] at 4 wavelengths (610 nm, 620 nm, 630 nm and 640 nm), each with a bandwidth of 10 nm. The initial guesses for chromophore concentrations for this experiment were those of adipose stated in the previous section

being 0.00231 mM and 0.00099 mM for oxy- and deoxyhaemoglobin respectively. An initial tomographic reconstruction of the spatial light distribution, using the surface fluence data obtained from the system and the initial guesses of chromophore concentrations, can be seen in figures 7.5(a) and 7.5(d). The iterative algorithm was then used in order to obtain a solution for the location of the light source within the tissue mimicking block phantom, using both a point source and distributed source. Figures 7.5(b) and 7.5(e) show the final reconstruction using a point source model and figures 7.5(c) and 7.5(f) show the final reconstruction using the distributed source model. In all parts of Fig. 7.5 the ground truth location of the light source within the phantom is represented by the green dashed area.

Table 7.2 represents the quantitative analysis of the tomographic reconstruction carried out in this experiment. As can be seen using a point source model, the second iteration was returned with a localization error of 3.32 mm and a maximum distance observed at FWHM of 3.91 mm. Compared to a better localization error of 1.53 mm and maximum distance at FWHM of 7.78 mm using a whole distributed source model, which is of the order ~ 5 times closer to the ground truth size of 7 mm. The chromophore concentrations recovered by the algorithm are 0.0532 mM and 0.0536 mM for oxy- and deoxyhaemoglobin respectively. Taking these values and converting them to an underlying absorption coefficient gives a range of μ_a = [0.0592 – 0.1351] mm^{-1} between 610 nm and 640 nm, which represents the ground truth values well.

Table 7.2. Analysis of tomographic reconstructions from the homogenous block phantom, showing the iteration number returned, the localization error and maximum distance at FWHM for when the sources where modelled as both a point source and a distributed source.

	Iterations	Localization Error (mm)	FWHM (mm)	Ground Truth Size (mm)
Point Source	2	3.32	3.91	7
Distributed Source	6	1.53	7.78	7

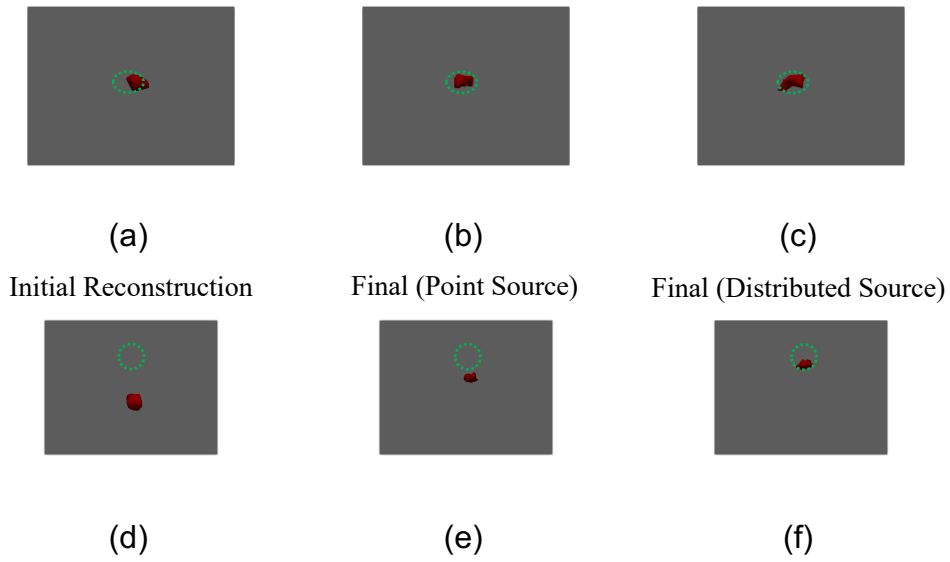

Figure 7.5. Reconstructions of an LED within a homogeneous block phantom. (a – c) Top view of the initial iteration, final iteration modelling the source as a single point and final iteration modelling the whole source respectively. (d – f) Side view of the initial iteration, final iteration modelling the source as a single point and final iteration modelling the whole source respectively. Green dashed area represents the ground truth location of the source.

7.4. Discussions

Current methods of tomographically reconstructing light sources within an object of interest, for example in bioluminescent tomography, rely on knowing the underlying optical properties of the object in order to obtain an accurate solution. This can be done through either a priori information for example from ATLAS based information [13, 79]

or through the use of multi modal systems that have the capability of directly measuring such properties [240]. The work in this paper outlines the development and testing of an algorithm that uses fluence data from an internal light source at the surface of the object of interest to reconstruct both the source localization and underlying optical properties of the object simultaneously. Taking advantage of a previously developed system [241], that is capable of collecting hyperspectral surface fluence data, a number of simulation and real data experiments were designed in order to test the ability of the algorithm in finding a correct solution to the problem. By doing this a vast amount of time is saved in data collection as compared to existing methods as they typically use a manually changed spectral filter approach in order to build up a multi-spectral dataset.

The algorithm developed has shown to perform well in localizing the spatial light distribution present in both 2 and 3-dimensional simulated cases, as well as homogenous and heterogeneous mouse phantoms. Real experimental data was then tested to see if the outcomes found in simulations could be replicated in an experimental setting. This was done by collecting hyperspectral surface fluence data using the system described in chapter 5 and applying the algorithm presented to the dataset. To further test the robustness of the algorithm when optical parameter updates were being calculated, the source location used was modelled as a point source centred at the reconstructed light distribution at full-width-half-maximum, as well as modelling the source as the entire spatially distributed light source reconstructed at FWHM. It was found in all cases that the algorithm performed well at localizing the source distribution as well as obtaining good volumetric accuracy, especially in the more realistic examples demonstrated in sections 7.3.3 and 7.3.4.

In order to quantitatively analyse the accuracy of reconstruction, two different metrics were used. The first being the localization error, which is a measure of the Euclidean distance between the centre of mass of the reconstructed distribution at FWHM and the ground truth location. The second metric use was the maximum Euclidean distance between nodes present within the distribution at FWHM, which gives a direct indication of the size of the reconstruction. In the 2D case, good localization was seen with errors of ~ 1 mm and 0.8 mm for a point source model and distributed model respectively. A maximum FWHM of 10 mm was found when using both models, which is ~ 3 times that of the ground truth, however this increase is also seen when reconstructing the source using the known ground truth optical parameters. When running simulations of a 3-dimensional mouse phantom, similar results were seen, with localization errors of ~ 2.2 mm and 1.25 mm for when a point source model and distributed source model was used respectively. The calculated FWHM was found to be ~ 8 mm for both models, which is ~ 2 times that of the ground truth. A more realistic example was explored through the use of a heterogeneous mouse phantom containing 8 distinct regions of different optical properties that relate directly to the anatomy of a real mouse. When using a point source model, a localization error of 1.3 mm was found along with a FWHM of 11.4 mm, which is much larger than the ground truth value of 4 mm. However, when modelling the update source as the whole distributed reconstruction, much better accuracy was gained with a localization error of 0.9 mm and a FWHM of 4.6 mm. These results were mirrored when using real experimental data, with a localization error of 3.32 mm and maximum distance of 3.91 mm when a point source model was used. As compared to when a whole distributed source model was used a localization error of 1.53 mm and a FWHM of 7.78 mm was

calculated, being ~ 5 times closer to the ground truth value of 7 mm that in the point source model case. When compared to similar data [241], it can be seen that by using this algorithm for reconstruction, results with much better accuracy can be observed.

This proposed algorithm is aiming to account for the underlying unknown optical parameters in order to gain a tomographic reconstruction with improved accuracy and quality. The optical absorption coefficient recovered for the experiment phantom ranged between μ_a = [0.0592 – 0.1351] mm^{-1} for the wavelengths used. Although these values match well with the ground truth values of μ_a = [0.007 – 0.12] mm^{-1}, further work is required to look at its biological relevance. When carrying out tomographic reconstructions using a heterogeneous mouse model or a real murine example, a priori knowledge of the structure of the mouse has been used in this work. This allows for the algorithm to account for small areas of high absorption within the mouse, without the need for directly measuring the optical properties of these regions This information can be gained using methods such as the permissible regions techniques explained above or through the use a mouse atlas such as Digimouse [238], to infer the internal structure of the mouse from measurements of key features on the surface of the mouse.

Using this new algorithm to tomographically reconstruct spatially distributed internal light sources, by simultaneously recovering the underlying optical properties and localizing the source can potentially address a number of issues that typically arise in tomographic imaging, such as bioluminescent tomography (BLT). The first of which is accounting for the unknown optical parameters of the subject, which is typically met by directly measuring the optical parameters using a multi-modal system [240], resulting in a vast increase in data collection time, which is especially valuable in cases such as

BLT where the timeframe of light emission is finite. The system developed allows for the collection of hyperspectral data without the need of spectral filters to be used, further giving the potential for the data collection time to be reduced. The use of a filter-less system also addresses issues that are raised in filter based systems, whereby the bandwidth of said filters have an effect on measured data [11]. The effective bandwidth and number of spectral measurements made are limited by only the spectral resolution of the spectrometer used, therefore can be controlled well and is a topic for future work.

7.5. Conclusions

This chapter highlights the development of an algorithm to be used in conjunction with a previously presented hyperspectral imaging system [241]. The main aim of the algorithm is to achieve better source localization by simultaneously calculating and updating the underlying optical properties and tomographically reconstructing the spatial light distribution using an iterative method. The algorithm has shown to give solutions with good localization accuracy (~1 mm) with both 2 - and 3 – dimensional simulations using homogenous, heterogenous models as well as real experimental data from a tissue mimicking block phantom. Good volumetric accuracy was also achieved in the heterogenous mouse model and experimental data when modelling the updated source as the whole distributed reconstruction at FWHM. These results have the potential to directly translate to improvements in data collection times, especially in multi-modal multi-spectral systems where the underlying optical properties are unknown. It is believed that the algorithms accuracy and efficiency could be improved further through the use of spectral derivative data, as this has been shown previously to improve the accuracy of tomographic reconstruction of bioluminescent

light sources [13]. As hyperspectral data is collected with the system presented, it is possible that the system and algorithm could be utilized to simultaneously collect data from multiple sources of different wavelengths. Other possible improvements could be gained from the true utilization of the hyperspectral data by incorporating a much greater number of wavelengths at each stage of the algorithm and optimizing the bandwidth of data used all of which will be subject of further investigation.

The following chapter presents the application of the novel multi-parameter reconstruction algorithm as applied to real murine tumour models. Also presented is context into the importance of obtaining accurate estimates for the underlying optical properties of the small animal being imaged.

CHAPTER 8

APPLICATION TO REAL MURINE DATA

The previous chapter introduced the design and testing of a multi-parameter recovery algorithm that can be used to account for the optical properties of an animal whilst simultaneously recovering source location. The work presented in this chapter is presented in an article that has been submitted for publication: Quantitative Molecular Bioluminescence tomography[3]. This article investigates the application of the multi parameter recovery algorithm presented in the previous chapter on real murine data as well as demonstrating some of the key advantages it brings over traditional bioluminescence imaging and tomography. This work was completed in collaboration with Professor Ken Kang-Hsin Wang and his research group at the university of Texas Southwestern. All data presented in this chapter has been used with the permission of Professor Wang. To maintain accuracy, sections 8.2.1. through 8.2.7. were written by Professor Wang and his team, for which permission was also granted to be included in this thesis.

8.1. Introduction

Often overlooked, is the importance of having accurate computational models for both the structure and the underlying optical parameters of the animal/tissue being imaged to allow accurate 3D imaging through optimization [232]. Structural knowledge can be gained through secondary modalities, such as MRI [235], CT [76] and ultrasound [236],

[3] Submitted for publication in the Journal of Biomedical Optics December 2021

which can be used to develop an accurate model for optimization and 3D reconstruction, although often relying on estimated tissue optical parameters. Heterogeneous models have been used [84, 86, 232] to offer an alternative, through registration with an atlas model, or defining permissible regions to improve accuracy [233, 234]. Work targeted towards direct imaging of optical properties through the use of Diffuse Optical Tomography (DOT) have demonstrated promise, however with increased imaging and development cost [230].

BLT in areas of research such as oncology has shown to be of benefit as a tool allowing high contrast image-guided radiation therapy [242, 243]. Specifically, to advance image-guided irradiation for soft tissue targeting and treatment assessment, a unique multi-modal system has been developed combining BLT with X-ray cone-beam CT (CBCT) for pre-clinical radiation research. The system has been verified using an orthotopic glioblastoma (GBM) model [100, 242] and orthotopic pancreatic ductal adenocarcinoma (PDAC) model [101], with accuracies of tumor location recovery of ~1 and 2 mm respectively. Limitations however exist from the need of a trial-and-error approach for optimizing the unknown optical parameters of the tissue, based on structural a-priori knowledge from the CBCT.

A novel optimization algorithm allowing simultaneous recovery of optical parameters directly from bioluminescence data was presented in chapter 8 [244], but wasn't applied to real biological data. Here the first ever in-vivo application of the optimization algorithm, recovering both the bioluminescence source, intensity as well as the tissue absorption (total hemoglobin content) in small animal BLT system is presented.

The challenges and limitations as observed in commercial preclinical BLI/BLT systems are highlighted, using the example models of orthotopic GBM and self-

luminous light source implanted in pancreas to highlight the benefits of the proposed algorithm. Not only is it possible to accurately recover the spatial distribution of a bioluminescence source, but also the potential to recover biologically informative parameters such as hemoglobin content, without the need for additional or assumptions, allowing quantitative BLT.

8.2. Methods

8.2.1. Orthotopic Glioblastoma (GBM) Mouse Model

To establish the orthotopic GBM mouse model, a C57BL/6J mouse (female, 8 weeks old; Jackson Laboratory, Bar Harbor, ME) was immobilized on a stereotaxic instrument (Catalog No. 51730; Stoelting, Wood Dale, IL) at prone position. A 5-8 mm sagittal incision on the scalp was made. A 0.5-mm-diameter parietal burr hole at 2 mm anterior to the lambdoid suture and 2 mm left to the sagittal suture of the skull was made with an electric bone drill (Catalog No. 51449; Stoelting, Wood Dale, IL). We injected 1.2 x 10^5 GL261-*Luc*2 cells in 2 ml of phosphate buffered saline (PBS) 3 mm deep in mice brain by utilizing a 10 ml Hamilton gas-tight syringe with 32-gauge blunt-tip needle (Catalog No. 53485-1; Stoelting, Wood Dale, IL). We injected 1 ml of cell suspension and waited for 1 minute, and repeated these two steps until all suspension was injected. After the injection was completed, we raised the syringe 1 mm and waited for 1 minute, and repeated these two steps until the needle was completely moved out of mouse head. The skull opening and incision were sealed with tissue adhesive (No. 1469SB; 3M Vetbond$^{TM/MC}$, St. Paul, MN).

8.2.2. Implantation of self-luminous light source into mouse pancreas

A self-luminous light source (cylinder, 0.9 mm in diameter, 2 mm in length) was surgically implanted into the pancreas of albino C57BL/6J mouse (female, 8 weeks old; Jackson Laboratory, Bar Harbor, ME). The surgical site was located at the skin on the mouse left flank, around spleen position, posterior to rib. An 8-12 mm transverse incision was made on the skin at the surgical site, and another 8-12 mm transverse incision was made on the peritoneum right under the skin incision. The spleen and pancreas were gently exteriorized, and the pancreas was spread out on the skin. A small pocket was created in the pancreatic parenchyma, and the light source was inserted into the tissue pocket. We used a 7-0 suture (CC1107N-45; AROSurgical™, Newport Beach, CA) to close the tissue pocket of pancreatic parenchyma. After placing the pancreas and spleen back into the abdominal cavity, we closed the incisions on the peritoneum and skin using a 4-0 suture (E15A04L-45; AROSurgical™, Newport Beach, CA).

8.2.3. BLT Systems

Two BLT systems in a similar configuration and equal performance were utilized in this study. The first one is an in-house BLT system [242] consisting of an optical assembly, a thermostatic system, a transportable mouse bed and a mobile cart. The optical assembly is driven by a motorized linear stage to dock onto the mouse bed for imaging. The assembly contains a rotatable 3-mirror system (98% reflective, protected silver coating) with 4 light emitting diodes mounted at its corners for photo imaging, a filter wheel (Edmund Optics Inc., Barrington, NJ), a charge-coupled device (CCD, iKon-L936; Andor Technology, Belfast, UK) mounted with a 50-mm f/1.2 lens (Nikkor, Nikon

Inc., Melville, NY), and a light-tight enclosure. The optical signal emitted from an imaged object was directed by the 3-mirror system, passing through the filter wheel and captured by the CCD camera. The image taken at top of the mouse bed is labelled as 0° projection imaging. The 3-mirror system can rotate 180° (from -90° to 90°) around imaged object for multi-projection imaging. The focal plane was set at ~ 11 mm above the mouse bed with the 3-mirror system placed at 0°. The pixel scale is the corresponding physical size of CCD pixel at focal plane, which is 0.12 mm per CCD pixel. The optical path from the focal plane to the front surface of the camera lens is 45 cm. Four 20-nm FWHM band-pass filters (Chroma Technology Corp., Bellows Falls, VT) at 590, 610, 630 and 650 nm were mounted in the filter wheel for multi-spectral imaging. The thermostatic system, which is built in the light-tight enclosure (except heat gun) and consists of a resistor, a thermocouple with monitor, 7 fans, and a heat gun with heat transport pipeline linked to the enclosure, was used to boost and maintain the temperature around the imaged object at 37 °C. The transportable mouse bed allows the imaged object transferred from the optical system to CBCT system for CBCT imaging. Eight ball bearings (BBs; PTFE balls, 2.4mm diameter; McMaster-carr, Santa Fe Springs, CA), which can be identified both in optical photo image and in CBCT image, were attached on the bed as the fiducial markers for registering the coordinates of optical and CBCT system. The in vivo data of GBM-bearing mouse was acquired by the in-house BLT system.

Our team and our industrial partner Xstrahl Inc. developed the second BLT system, MuriGlo (Xstrahl Inc., Suwanee, GA), built from the same concept of the in-house BLT system with improved capability of acquiring full 360° optical projection. Optical signal emitted from the animal is reflected from a 3-mirror system to a fixed 45° mirror,

passing through filter and captured by CCD camera (iKon-M 934; Andor Technology, Belfast, UK). The 3-mirror system supports the 360° multiple projection imaging. The fixed mirror and iKon-M934 CCD allow for a compact configuration. The focal plane was set at ~ 16 mm above the mouse bed with the 3-mirror system placed at 0°, and the pixel scale is 0.10 mm per CCD pixel. The optical path from the focal plane to the front surface of the lens is 40 cm. The in vivo data of the mice implanted with light source in pancreas was acquired by the MuriGlo system.

8.2.4. Quantification of System-Specific Cell Spectrum

Because of the multi-spectral BLT approach, it is important to quantify the optical system spectral response and the emission spectrum of bioluminescent tumor cells. The measurement via our optical systems includes spectral responses of the system and cell, and we called the resulted spectrum as system-specific cell spectrum. Therefore, the wavelength dependent BLIs can be normalized to the measured spectrum weighting, used as the input data for the BLT reconstruction.

We measured the system-specific spectral weights of GL261-*Luc2* cells at 590, 610, 630 and 650 nm in petri dishes with cells > 80% confluency at concentration of 0.75 mg of D-Luciferin per 1 ml of phosphate buffer solution (PBS) at 37 ˚C via our in-house optical system. To eliminate the change of the *in vitro* spectral signal as function of luciferin incubation time, open field images without filters were taken before and after each spectral BLI to quantify the *in vitro* signal variation over time. The time point for each image was recorded and the open field images were used to generate an *in vitro* time-resolved signal curve. We normalized the intensity of multi-spectral BLIs based on time-variant data from the time-resolved curve. The measured spectrum of the

GL261-*Luc2* at 590, 610, 630 and 650 nm are 1, 0.916 ± 0.014, 0.674 ± 0.019, 0.389 ± 0.012 (n = 20), respectively. The same procedure was applied to measure the spectrum of the self-luminous light sources. At 590, 610, 630 and 650 nm, the spectrum weights for the light sources in the mice shown in Fig. 8.8(a) and 8.8(b) are 0.942, 1, 0.893, 0.633, and 0.949, 1, 0.886, 0.626, respectively. We had also investigated the spectral response of the in-house and MuriGlo system. The difference is insignificant, rendering the measured spectrum can be applied to both systems.

8.2.5. In Vivo Bioluminescence Imaging

The GBM-bearing mouse was subject to multi-projection and multi-spectral bioluminescence imaging with our in-house optical system two weeks after the cell implantation. In preparation of bioluminescence imaging session for GBM-bearing mouse, mouse hair was shaved with a clipper, followed by hair depilation. D-Luciferin (125 ml, 30 mg/ml for 25 g mouse to reach 150 mg/kg, XenoLight D-Luciferin K^+ Salt, PerkinElmer Inc., Waltham, MA) was administrated via intraperitoneal injection. BL imaging was conducted 10 minutes after the D-Luciferin injection. Mouse was anesthetized with 1-2% isoflurane (Fluriso, MWI Veterinary Supply Co. Boise, ID) in oxygen while imaging. Multi-projection (0°, 90° and -90°) and multi-spectral (590, 610, 630, and 650 nm) BLIs were acquired at 8 × 8 binning (0.96 mm/pixel at imaging plane), 4x pre-amplifier gain, and 1 MHz readout rate. Because the in vivo signal at 590 nm was weak compared to those at other wavelengths, which would affect the stability of the BLT reconstruction, we used the images at 610, 630, and 650 nm for this study. Open field images were acquired before and after each spectral image to build time-resolved curve for in vivo bioluminescence signal among different projections [242],

which was used to quantify the bioluminescence signal change during the bioluminescence imaging course.

The mouse bearing self-luminous light source in pancreas was subject to multi-projection and multi-spectral BLI (8 x 8 binning, 0.8 mm/pixel at imaging plane) in MuriGlo one week after the light source was implanted. The procedures of BLI acquisition for the pancreatic light source study were similar to those used for the GBM study. Since the implanted light source is closer to the surface of abdomen than that of dorsum, we chose supine position for the BLI acquisition. Due to the location of light source, no or minimum signal was detected at 90° and 180° projection, only the 0° and -90° projections were chosen as the surface input data for the BLT reconstruction.

Photo images at multiple projections were taken to retrieve the BB positions on mouse bed for mapping the BLI onto 3D mesh surface generated from the CBCT imaging as the input data for BLT reconstruction.

8.2.6. Cone-Beam Computed Tomography (CBCT) Imaging

After the bioluminescence imaging, the mouse bed with animal was transferred from the optical system to the small animal radiation research platform (SARRP; Xstrahl Inc., Suwanee, GA) for CBCT imaging. The SARRP consists of a dual focal X-ray source mounting on a 360° rotational gantry, an amorphous silicon flat panel detector and a 4D (3-axis translation and 360° rotation) robotic base. For SARRP CBCT imaging, the X-ray source employed a 0.4 mm focal spot at 65 kVp and 0.7 mA with 1 mm thick aluminum filter. CBCT image was acquired by rotating the animal with the 4D robotic base between the X-ray source and detector panel. Studied animal was anesthetized with 1-2% isoflurane in oxygen during the animal transportation and

imaging course. The acquired SARRP CBCT image was used to provide anatomical structure of animals to generate a tetrahedral mesh for the BLT reconstruction.

Contrast CBCT was used to assess the actual volume of the in vivo GBM [242], and the center of mass of the contrast-labelled tumor volume was calculated for BLT localization assessment. After SARRP CBCT imaging session, imaged mouse was moved to our in-house high resolution CBCT system [245] for the contrast imaging. The mouse was imaged 1 minute after the contrast injection at dose of 2gI/kg (Iodixanol, retro-orbital injection at 320mgI/ml, Visipaque, GE Health Care, Chicago, IL).

8.2.7. Data Mapping for Multi-Projection BLI's

Because CBCT imaging defines the coordinate used for BLT reconstruction, our geometry calibration method published in Ref. [242, 246] was used to map the 2D BLIs acquired at different projections onto the numerical mesh surface of the animal CBCT image. The mapped BLIs were used as the input data for BLT reconstruction. Our method has two steps: 1) mapping the CBCT coordinate to the 3D optical coordinate with rigid transformation, and then 2) projecting the 3D optical coordinate to the 2D optical (CCD) imaging plane. After the 3D CBCT and 2D optical coordinates are registered, for a given projection, we can then map the surface BLI to the CBCT image. The data mapping process requires knowledge of the geometrical parameters of optical system. The BBs on the mouse bed can be located in both CBCT and 2D optical images. An optimization routine with the constrained multivariable optimization function (fmincon, MATLAB, The MathWork Inc., Natick, MA) was developed to retrieve the geometrical parameters by minimizing the difference between the calculated and

measured BB positions in the 2D optical coordinate; the BB positions in 2D photo images were used as the measured positions, and the corresponding BB positions retrieved from the optimization routine based on the optimized geometrical parameters and the BB positions in 3D CBCT were used as the 2D calculated positions. The geometric calibration was performed for each animal imaging session to ensure accurate data mapping for BLT reconstruction.

The BLIs were then mapped onto the 3D mesh surface of the imaged mouse generated from the CBCT image. At the overlapped region on the mesh surface, for a given node between two mapped images from different projections, the maximum value of the two images was chosen as the value on that surface node. The mapped surface data larger than 10% of the maximum value among all the surface points were used as input data for BLT reconstruction.

8.2.8. Algorithm

The final algorithm needed to complete the entire framework is one that calculates both the optical properties, given the surface fluence rate data at multiple wavelengths, as well as the location of the source within the subject. To resolve unknown optical properties, Diffuse Optical Tomography (DOT) is a commonly used imaging technique, known as named due to the fact that the transport of light through tissue at wavelengths in the visible and near infrared (NIR) bands become nearly isotropic, therefore is well defined by photon diffusion. A software package, Near Infrared Fluorescence and Spectral Tomography (NIRFAST), was utilized to allow for the simulation of light propagation within biological tissue using a finite element method (FEM), documented elsewhere [130]. Within the package are a number of forward and inverse models, and

a spectrally constrained case is utilized in this work. The algorithm has been modified to take the internal bioluminescence source location and surface fluence data with the goal of directly estimating the concentrations of oxy-haemoglobin, deoxy-haemoglobin and water, as well as scattering power and amplitude [237]. The assigned chromophore concentrations can be used to calculate the underlying wavelength dependent absorption coefficient of tissue through the use of extinction coefficients of individual chromophores. This can similarly be done using the scattering power and amplitude to obtain a corresponding reduced scattering coefficient at each wavelength using Mie scattering theory. Using a continuous wave model, the Jacobian (function to allow mapping of measured data to internal optical properties) is calculated and then inverted using the Moore-Penrose pseudoinverse, which is typically more suitable towards underdetermined problems [159]. The Moore-Penrose pseudoinverse finds the 'best fit' or minimum norm solution to a system of linear equations, the implementation of which have been extensively detailed elsewhere [130]. From this an update in optical properties is calculated and the whole process is repeated, new boundary data is simulated and compared with the original data in order to calculate a projection error. This error is then used as a stopping mechanism for when it is considered that convergence has occurred, typically within 2% change. Regularization is used alongside the Moore-Penrose pseudoinverse with a starting value of 0.1, which is the standard value used as detailed elsewhere [130]. Firstly, multispectral data is collected as described above which are used with an initial 'estimate' of underlying optical properties to perform tomographic reconstruction of the spatial light distribution as achieved using a compressive sensing conjugate gradient (CSCGNW) algorithm described elsewhere [202]. A new source position is set and then through the DOT

algorithm, using the same dataset, optical properties of the medium are calculated. From this, if the error conditions have not yet been met, the optical properties are updated by the average value across the entire mesh or of a particular pre-defined volume within. Using these updated optical properties, the CSCGNW algorithm is then used again to reconstruct the new spatial light distribution and whole process is completed iteratively. As with the inverse problem outlined above a stopping condition is put in place to stop the algorithm when it is considered to have converged. The stopping criteria is the same as that used in the DOT algorithm whereby a projection error is calculated between the original and modelled data using the updated optical properties. The iterative process is continued until the change in projection error is below a tolerance which is typically set to 2%. When modelling the new source for the update of optical parameters, firstly the tomographically reconstructed source is represented as its full-width-half-maximum (FWHM) and the reconstructed distributed source, at the recovered FWHM, can then be set as the new update.

8.3. Results and Discussions

Traditional biological pre-clinical studies that utilize Bioluminescence Imaging (BLI) typically only use topographic data that is captured at the surface of an animal, taken at a determined wavelength and view. This method allows for qualitative information about the underlying source to be inferred from the intensity of light measured at the surface. Issues arise when employing this method due to the spectral dependance on absorption and scattering of light travelling through diffuse biological tissue. This implies that the intensity of light measured at the surface of the animal will be different depending on the detected wavelength. Another issue arises depending on the

viewpoint of the animal used when imaging takes place whereby the maximum and total intensity measured will change depending on the viewpoint used because of light propagation in space being dependent on the viewing angle. These effects are visualized in figures 8.1 and 8.2, whereby surface fluence data has been measured from an orthotopic GBM model, using three wavelengths, 610 nm, 630 nm and 650 nm. The top and side views of the surface fluence at each wavelength is shown in figure 8.1, where the difference in measured intensity in each case is apparent. These differences are quantified using the bar chart shown in figure 8.2, where the total and maximum intensity for each viewpoint and wavelength are shown.

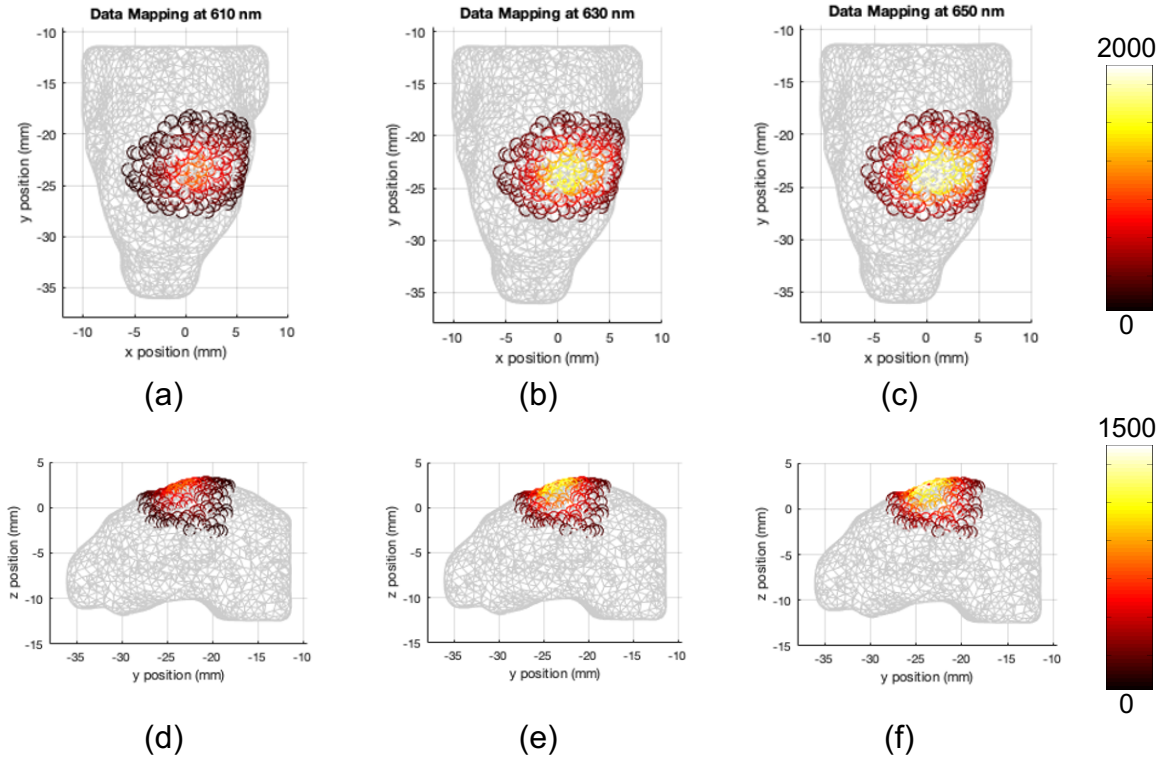

Figure 8.1. Top and Side topographic views of bioluminescence signal for GBM model at 610, 630 and 650 nm.

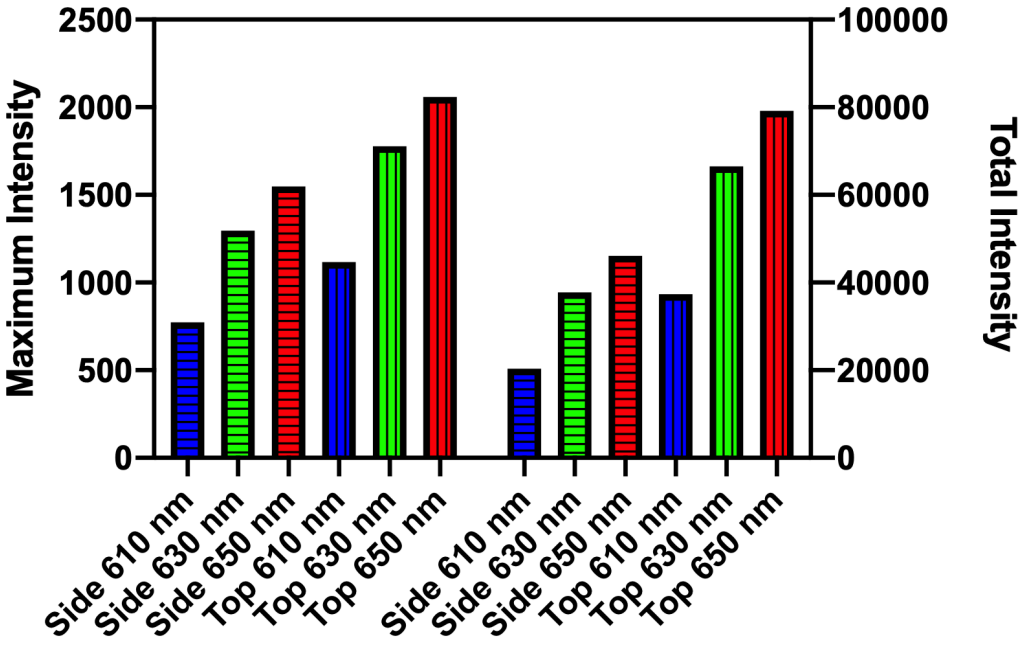

Figure 8.2. The effect of using topographic bioluminescence images for quantification at different wavelengths and views for (left) maximum intensity and (right) total intensity.

Because of the spectral and viewpoint dependency of light intensity measured when collecting 2-dimensional topological fluence data, it is impossible to confidently infer the underlying light source distribution. To counter this, through the collection of multiple viewpoints, it is possible to build a 3-dimensional topological image of the light intensity at the surface of the animal. This provides the ability to infer the underlying light distribution with more confidence, however images still suffer from the spectral variation of absorption and scattering properties found in biological tissue and free-space light propagation. Figure 8.3 shows the same GBM data as before however as a 3D topological image. There are computational methods available that can be used to correct these images for the spectral differences and emission of the bioluminescent source used, however it is still difficult to use the surface data alone to make any significant assumption about the size or location of the source. This is due to non-

uniqueness, meaning that a shallow source may give the same intensity measurements as a deeper source.

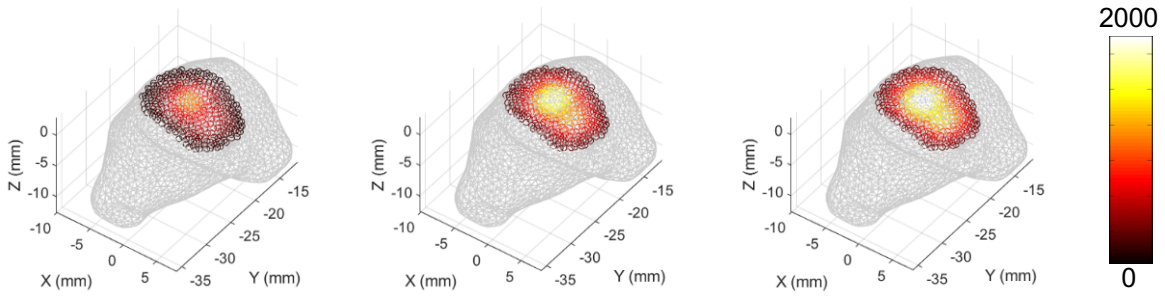

Figure 8.3. 3D surface fluence signal for GBM model at 610, 630 and 650 nm.

Bioluminescence Tomography (BLT) takes BLI a step further, by using prior knowledge of the animal being imaged to reconstruct the 3D spatial distribution of bioluminescent molecules located within the animal using model-based data optimization. To do this a number of conditions need to be satisfied, the first being the need for an accurate computation model of the animal. This information is typically gained through the use of a different imaging modality such as a CT [76], MRI [235] or optical surface capture methods [91]. Traditional BLT requires accurate knowledge of the underlying optical properties of the animal being imaged. This information can be gained using a different imaging modality such as Diffuse Optical Tomography (DOT) [152] or through a 'trial and error' approach. In order to address the issue of non-uniqueness, it is necessary to collect surface fluence data at multiple wavelengths [10], due to the spectral dependence of the optical properties. This multi-spectral data is often collected through the use of a filter-based system [1], however can also be collected through the use of a hyperspectral 'single-pixel' based imaging system [241]. When carrying out

tomographic model-based reconstructions, it is common to use the raw intensity of light measured at each wavelength that has been corrected for the bioluminescent emission spectrum of the molecules. Issues arise from doing this, which relate to the position and shape of the animal being imaged, due to the Lambertian nature of light exiting a boundary of diffuse media. To account for this, it is possible to use a free-space model [12], however this can be time consuming and complex. To overcome this problem, it was shown that by using spectral derivative data, which utilizes the 'logarithm of intensity', it is possible to improve the quantitative error of BLT from 49% to 4%, without the need to collect additional data or make any modifications to existing imaging systems [13].

The importance of having accurate knowledge of the underlying optical properties to account for light propagation in model-based optimization is shown in figures 8.4 and 8.5. Figure 8.4 shows tomographic reconstructions using the surface fluence rate data of the same GBM mouse model, using two different assumed concentrations of Total Haemoglobin (cTHb) as the optical properties used for model-based reconstruction. Optimization techniques are carried out using a spectral derivative method and are then thresholded to half the maximum value present.

Figures 8.4(a-c) represents tomographic reconstruction when an underestimation of optical properties was used (cTHb = 0.05 mM) with the results visually showing a larger, much deeper reconstruction. Figures 8.4(d-f) represents tomographic reconstruction when an overestimation of optical properties was used (cTHb of 0.2 mM) with the results visually showing a larger and more superficial reconstruction. Differences in the reconstructions are quantified in Figure 8.5 using four different metrics. The first metric used is localization error, which is the Euclidean distance

between the centre-of-mass (COM) of reconstruction and ground truth location which was measured using a CBCT. It can be seen that the localization errors of the ground truth and underestimated reconstructions are vastly different, whereas the ground truth and overestimated reconstructions are similar. This is due to the ground truth location of the tumor used in this example being shallow and a larger difference in error would be expected if the ground truth location was deeper within the animal. The second metric used is the full-width-half-maximum (FWHM) distance, which is the largest distance between reconstructed nodes at half the maximum value. As can be seen, both the under and overestimated reconstructions show a FWHM that is larger than the ground truth value. The third and fourth metrics used are maximum and total reconstructed intensity. If using an underestimation of optical properties, it can be seen that the reconstruction has a maximum intensity that is close to the ground truth, whilst having a much larger total intensity. On the other hand, using an overestimation of optical properties gives a total intensity with is close to the ground truth whilst giving a much lower maximum intensity. All of these calculated metrics show the importance of using accurate optical properties when carrying out tomographic imaging, as they all represent significant values that are taken into account in biological studies.

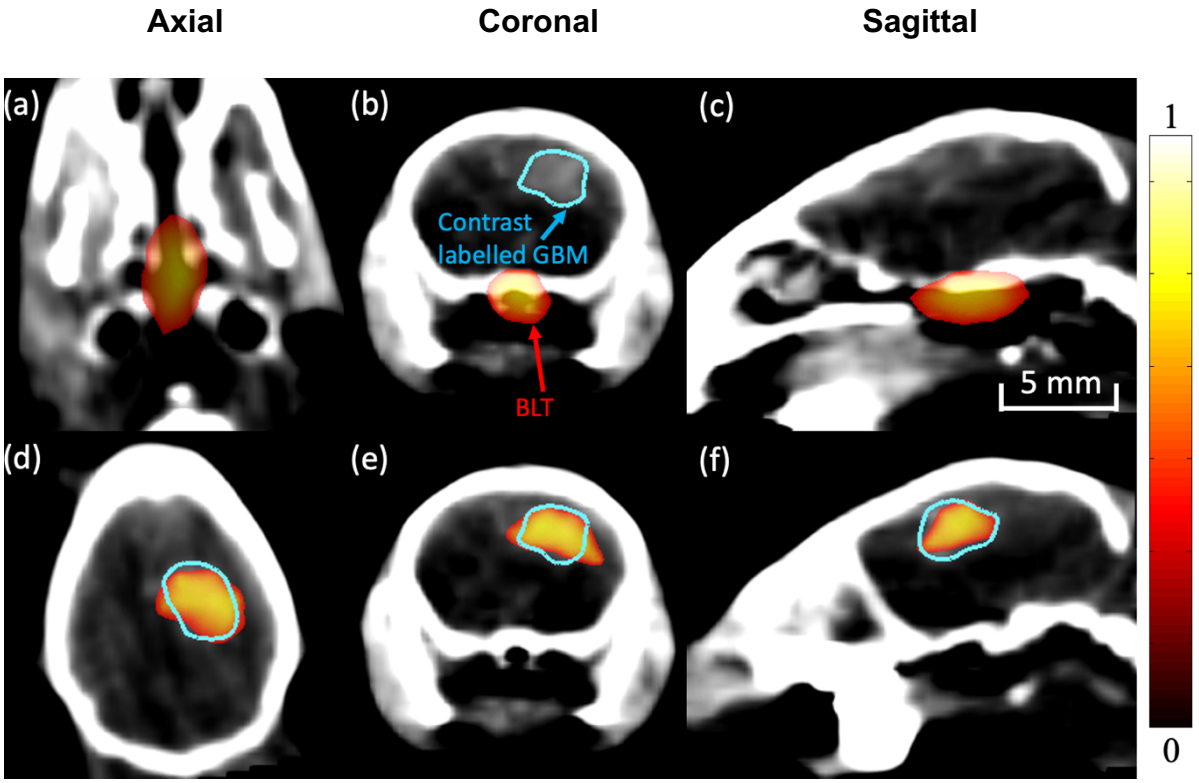

Figure 8.4. 3D tomographic reconstructions (normalized) of bioluminescence GBM model using (a-c) optical parameters using an underestimated assumption (0.05 mM cTHb) and (d-f) using an overestimation of underlying optical parameters (0.2 mM cTHb). The blue contour shows contrast labelled GBM.

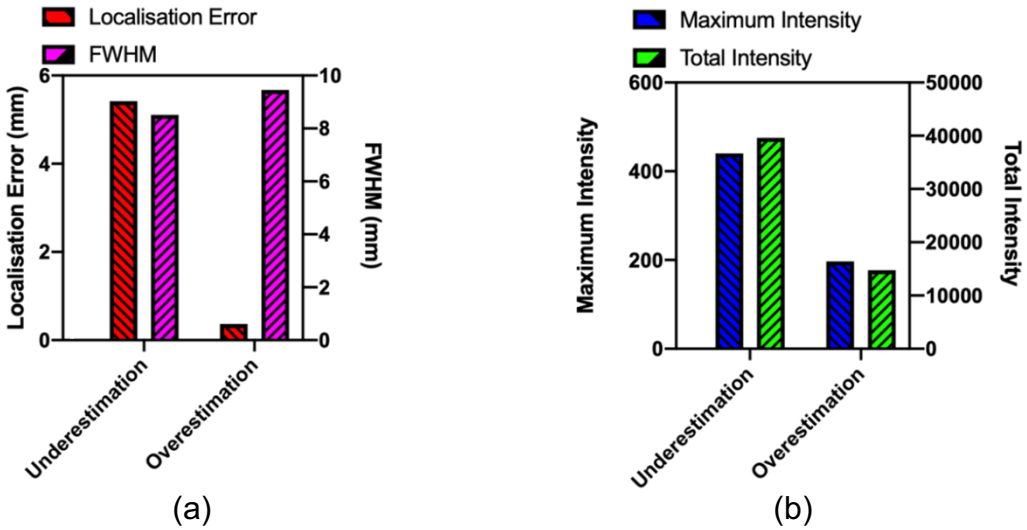

Figure 8.5. Calculated values of localization error, FWHM, maximum intensity and total intensity based on differing assumptions of optical properties.

To allow the use of BLT without the need to assume the underlying optical properties of the animal through the use of a second imaging modality, an algorithm was developed to use the knowledge of the emission spectrum of the bioluminescent source to employ an iterative method of optimizing optical properties whilst simultaneously localizing the source accurately. The theoretical details of this algorithm and its use on simulated data has previously been outlined [244]; it works by choosing an initial 'estimate of optical properties, which can also be guided by literature or prior knowledge. BLT is carried out with the initial 'estimate' and the reconstruction is taken as any recovered spatial point above half of the maximum intensity. These points are then set as a new source location and diffuse optical tomography (DOT) is carried out to recover optical properties that best match the data, which are then used again for BLT and the process is repeated iteratively until the algorithm converges and the projection error, which is the error between the measured data and modelled data has been minimized, the so-called minimization algorithm.

To show the benefit of applying this algorithm to real experimental data, it is used on the same GBM mouse model, above. The algorithm is initialized using starting 'estimate' of cTHb of 0.05 mM and 0.2 mM, which represents the under and overestimates in Figure 8.4. Figures 8.6 (a-c) shows the final iteration of the algorithm when using both starting points, which closely resembles the reconstruction achieved with 'ground truth' optical properties. Figure 8.6(d) shows the projection error calculated at each iteration of the algorithm and it can be seen that both initial estimates converge to the same error. Figure 8.6(e) shows the calculated localization error of the tomographic reconstruction at each iteration and is shown that both starting points result in a localization error of ~ 0.87 mm, which is similar if not better than values

stated in literature using ‘gold’ standard methods to obtain optical properties. Figures 8.6 (f-g) show the calculated FWHM and total intensity recovered at each iteration, which converge on 2.8 mm and 9868 counts respectively. Finally, figure 8.6(h) shows the average concentration of total hemoglobin calculated at each iteration. This calculated cTHb converges to 0.145 mM assuming 70% oxygen saturation across the entire animal.

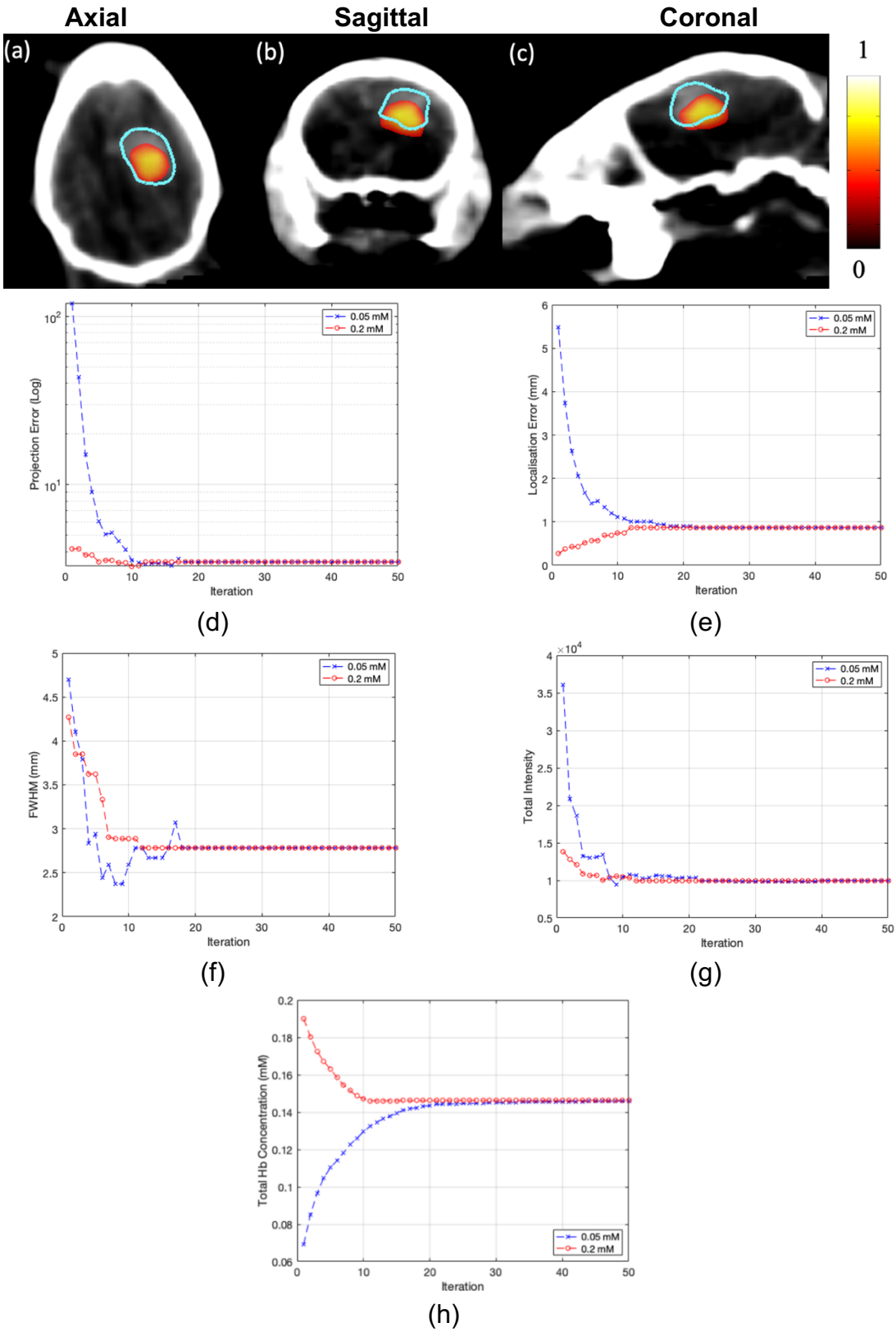

Figure 8.6. Reconstructions of the GBM mouse model and analysis. (a-c) Final reconstruction using the multi-variant optimization algorithm. (d) Projection error versus iteration for low and high initial cTHb, (e) COM localization error, (f) FWHM distance, (g) total intensity and (h) calculated cTHb of tissue.

In order to further demonstrate the ability of the optimization algorithm on more complex models, it was next applied to two mice with a self-luminous light source implanted in the pancreas. The light sources are visible in CBCT image, and thus are used as the ground truth to assess accuracy. These mice differ from the GBM example such that the whole animal was imaged, resulting in a much larger reconstruction space (~40000 nodes) and hence greater numbers of unknowns. Figure 8.7 represents the normalized topographic images collected at 650 nm for each of the light source-implanted mice with each case the bioluminescent source being at a different depth and location.

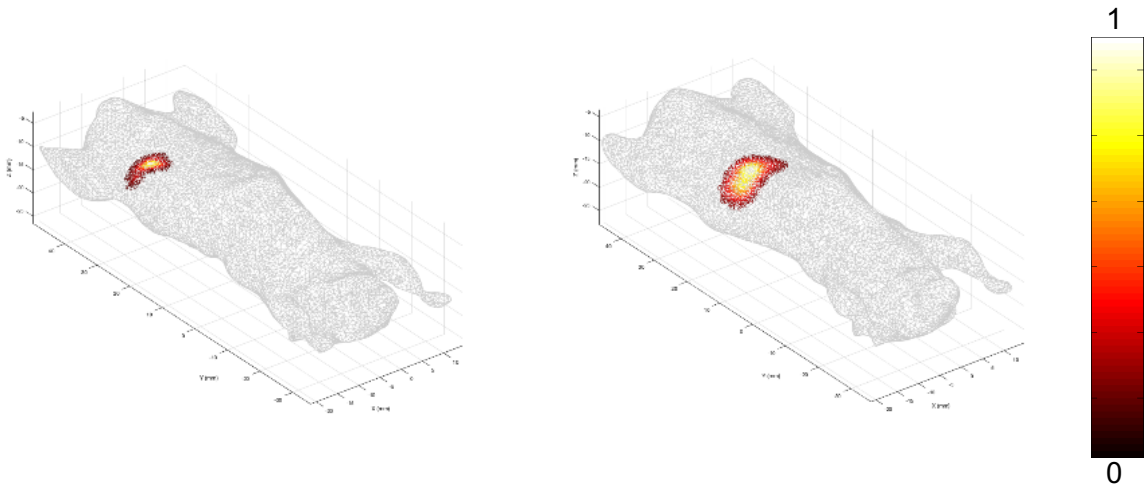

(a) (b)

Figure 8.7. Normalized 3D surface fluence rates at 650 nm for two mice with self-luminous light source implanted in pancreas.

For each case the surface fluence rate data was collected at three wavelengths (610 nm, 630 nm and 650 nm) and then processed through the optimization algorithm using an initial ‘estimate’ of 0.05 mM for cTHb. The algorithm ran for 50 iterations for each case and typically converged to a solution before all iterations were complete. Figure 8.8 displays the tomographic reconstructions for the final iteration of each mouse.

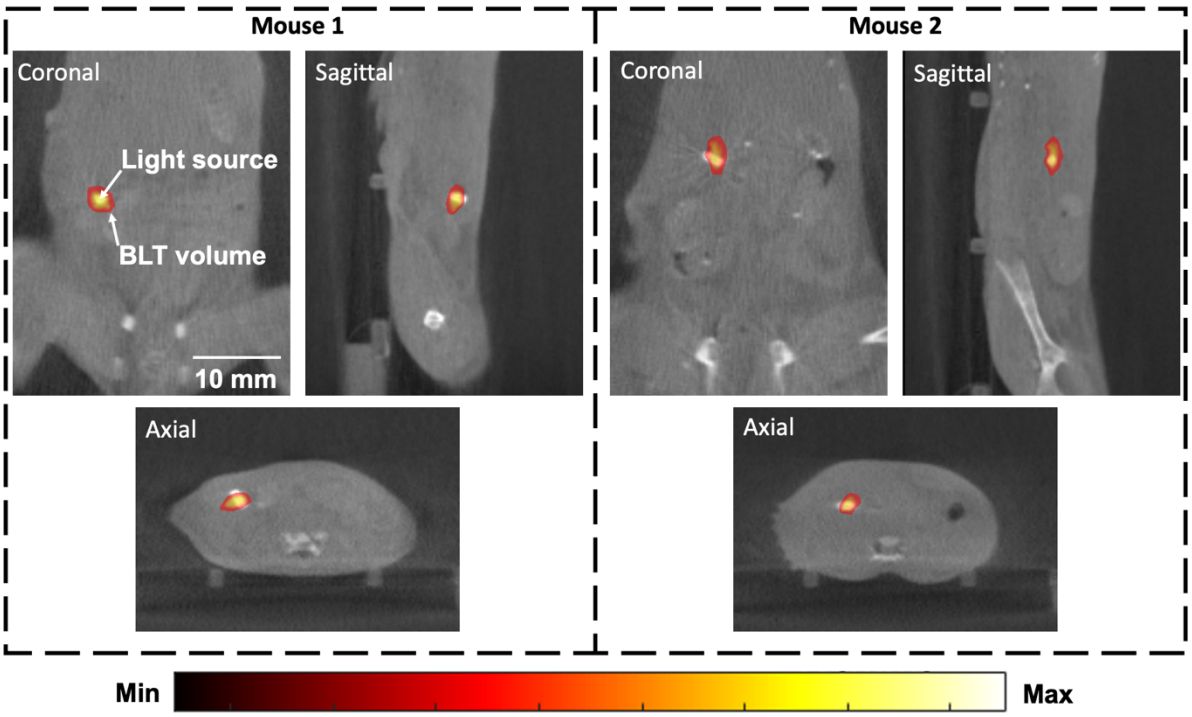

Figure 8.8. 3D tomographic final iteration reconstructions for two mice with light source implanted in pancreas.

To quantify the efficiency and accuracy of the reconstructions, the same metrics as used for the GBM model were utilized and shown in Figure 8.9. Firstly, the localization error of each model was calculated, as compared to the ground truth location, which was found to be <0.7 mm over the two mice. The total and max intensities of each mouse were found to be ~5400 and ~285 respectively and strikingly similar. The FWHM distance of the reconstructed sources across the two mice was <4.5 mm. The calculated concentration of total hemoglobin across both mice was found to be 0.1121 mM and 0.1151 mM.

Table 8.1 The reconstructed cTHb, COM localization error, total intensity, maximum intensity and FWHM from the initial and final reconstructions for the mice with light source implanted in pancreas.

Mouse	THb Concentration (mM)	Localization Error (mm)	Total Intensity	Max Intensity	FWHM(mm)
1	0.1121	0.42	5461	287	3.8
2	0.1151	0.69	5327	286	4.5

8.4. Conclusions

This chapter highlights the progression and historical advancements made in Bioluminescence Imaging (BLI) and Tomography (BLT). BLI measures light fluence rates from a bioluminescent source at the surface of the animal to infer the size and location of a tagged source, such as a tumor, within the animal. This is typically done using a single viewpoint and wavelength to create a 2-dimensional image of the light measured at the animal surface but suffers from inaccuracies due to poor localization and viewpoint dependence of light travelling through tissue. These can be improved via multiple viewpoints to allow 3-dimesional images to be created, however source localization remains challenging due to the uniqueness of the problem; multiple source size/location give rise to the same single wavelength data. To add quantitative accuracy these 3D images can be used alongside optimization algorithms utilizing accurate models of light propagation to tomographically reconstruct the 3D spatial distribution of the bioluminescent source. Conventionally to achieve this a multi-modal system is required to estimate the optical properties of the animal (for example diffuse optical tomography), and structural information (by for example CT or MRI). Multi-

spectral data is then required to overcome the non-uniqueness of the solutions as well as computational models to account for the path of light in free-space (animal to detector), increasing data collection and computational time. Advanced optimization algorithms use spectral derivative data, to allow accurate reconstructions whilst not requiring a free-space model, as light at similar wavelengths follow the same path. Finally recent advancements in hardware and imaging systems have allowed quicker and cheaper collection of hyperspectral data, such as those based on compressive sensing.

An algorithm was developed with the aim of achieving better source localization by simultaneously calculating and updating the underlying optical properties and iteratively reconstructing the spatial light distribution, in 3D and shown to achieve good accuracy in simulated data and a tissue-mimicking block phantom [244]. This algorithm has been applied and validated in a set of in-vivo mouse models, including an orthotopic glioblastoma model and two mice with self-luminous light source implanted in pancreas. It is shown that using this optimization algorithm, localization accuracies of <1 mm is obtained on all cases which is similar if not better than current 'gold standard' methods that predict optical properties using a different imaging modality. Application of this novel approach has shown that quantitative BLT is possible without the need for any prior knowledge about optical parameters, whilst achieving good localization accuracies. Simultaneously recovery of chromophore concentrations and optical parameters from the same dataset is possible, with no prior information, other than the spectral absorption spectrum of these absorbing molecules (oxy and deoxy hemoglobin), which can provide important biological information in a vast number of pre-clinical research settings such as radiation oncology, in guiding radiation and

assessing treatment response for important orthotopic tumor models. This proposed and validated algorithm can pave the way for true molecular imaging of both exogenous and indigenous biological tumor characteristics and functionality such as hypoxia.

CHAPTER 9

CONCLUSION AND FUTURE WORK

9.1. Conclusion

Bioluminescent imaging and tomography are important tools that are used within pre-clinical trials to gain a non-invasive insight on biological activity within small animals. This work has presented the development of a novel hyperspectral imaging system based on compressive sensing, with the aims of reducing both the costs and time associated with data collection, whilst improving the capabilities and quantitative accuracy of the modality. Also presented was the development of a novel multi-parameter reconstruction algorithm that combines Diffuse Optical Tomography and BLT to recover optical parameters and source location simultaneously. The main aim of the developed algorithm was to further reduce the cost and time used by BLT by eliminating the need for additional imaging modalities, such as MRI, CT and standalone DOT. As well as this the algorithm can provide true quantitative molecular imaging, with greater accuracy and reliability.

The workflow of the novel system is to employ the technique of compressive sensing to sequentially take random samples of the surface flux from the surface of a small animal due to a bioluminescent light source. Optimisation algorithms are then used to reconstruct the hyperspectral data that is incident from the animal surface. This can be done by taking advantage of the sparsity that is present in the data, allowing for it to be represented by fewer measurements and therefore requiring less time to obtain a

full set of data. Further optimisation algorithms are then used to take the surface fluxes at multiple wavelengths along with an computational model of the animal to tomographically reconstruct the 3D distribution of bioluminescent molecules within the animal. This is done by modelling the transport of light throughout diffuse media, which is the focus of chapter 3. The novel systems functionality is based upon the theory of compressive sensing which has been outlined in chapter 4.

The system was designed first as a proof of concept, utilising a ready built optical system, where the first main aim was to have the capability of capturing random projections of light incident at the surface of a small animal. Once it had been proven that this method was viable, the system was optimised, to improve its sensitivity, by building a custom designed optical engine. Chapter 5 of this work discussed the progression made from initial design of the proof-of-concept system through to the custom designed system. The system was also characterised to allow and correct for any noise and discrepancies, such as the spectral response of the optics or differences in the systems field of view. Chapter 6 presented the first of three journal papers that make up the final three chapters of this thesis. This highlighted initial testing of the novel system using tissue mimicking phantoms to show the effect of number of projections and the fullness of the patterns used of image reconstructions. The capabilities of the system have also been shown, by carrying out tomographic reconstructions using both block and mouse shaped phantoms. Multi-colour tomographic reconstruction was also achieved, demonstrating one of the many advantages using a hyperspectral system based on compressive sensing can bring. This system is one of the first hyperspectral imaging systems utilising compressive

sensing built in the world and has been shown to reduce the time and cost required when obtaining data, making it more accessible than commercial systems.

The second aim of this work was to develop an algorithm that can achieve multi-parameter reconstruction by simultaneously recovering the bioluminescent source distribution and underlying optical properties using the same dataset. This was achieved and presented in chapter 7 of this thesis, which shows the second published journal paper that arose from the work carried out during the project. Chapter 7 showed the application of the novel algorithm on simulated datasets as a proof of concept. This work demonstrated the algorithms' ability to accurately recover both the underlying optical parameters as well localising the bioluminescent source distribution. Therefore, allowing for accurate bioluminescent source reconstruction to be carried out without the need for a priori knowledge of the optical properties. This allows for much cheaper and more accessible bioluminescent tomography to be carried out due to not requiring a multimodal system to measure the optical properties directly. The ability of the novel algorithm was verified further through the use of real murine bioluminescent models, that was kindly provided by the University of Texas Southwestern. Chapter 8 presents the application of the novel algorithm to this experimental data, further proofing the capability of the algorithm to accurately reconstruct bioluminescent light distributions with accuracies of < 1 mm, which is similar if not better than current 'gold standard' methods. This work has shown that is possible to carry out quantitative BLT with no need or prior knowledge of optical parameters. The novel algorithm is one of the first developed of its kind and can benefit a vast number of pre-clinical research settings such as radiation oncology in assessing the treatment responses in different tumour

models. It can also possibly pave the way for true molecular imaging of the important biological characteristics and functionalities of tumours, such as hypoxia.

The work presented in this thesis offers new approaches to both the hardware and software that is used for BLT, allowing for cheaper, more time effective and more accessible imaging. Added capabilities also make the technology developed in this work superior to existing commercial systems allowing for better quantitative accuracy. It is hoped that the work carried out can and has made an important impact to pre-clinical research and possibly make previously unachievable targets achievable.

9.2. Future Work

Although the work presented here as is has vast potential to improve the way BLT is carried out in pre-clinical research, there is huge scope for future work to improve its capability further.

The novel system has many changes that can improve its capability. Firstly, all individual components can be optimised further to maximize the light throughput, in turn improving the SNR and gaining the ability to detect weaker signals. Further improvements include replacing the sensor with a more sensitive sensor, allowing for an additional increase in SNR. To improve the capabilities of the system, extra features could be added, such as a surface capture system to aid in generating an FEM mesh of the small animal that is used in reconstructions. Another improvement would be to add the ability to take multiple views of the small animal. This can be achieved by the addition of mirrors to measure side and bottom views, or through the addition of a device to rotate the animal throughout the imaging process. Although the novel algorithm developed addresses the issue of obtaining the underlying optical properties

of the animal, a method of carrying out hyperspectral DOT is a fairly trivial addition to the system. This can be done by incorporating a method to inject light from a source, such as a laser, into different points on the surface of the animal. The light exiting the animal can then be measured using the same detector setup that is used for taking bioluminescent measurements. Whilst these additions add cost to the system and increase the time required to collect data, they add further functionality that may be desired in some situations. Other improvements to the system include making it capable of carrying out imaging on live animals. To do this the system will require the ability to provide anaesthetic to the animal, so that it remains still during imaging. Another requirement would be for the system to regulate the temperature of the imaging chamber, so that no irregularities in the animal's biological functionality occur due to temperature.

A current limitation of the system is that it has only been applied to fairly simple homogenous tissue mimicking phantoms. In order to further verify the capability of the novel system experiments could be carried out on more complex heterogenous phantoms, which will allow insight into how the system performs when imaging real animals. These phantoms could be increased in complexity sequentially throughout experiments to gain real knowledge on how capable the system is in detecting and reconstructing bioluminescent markers. Once the system has been shown to work with highly complex phantoms, experiments can then be completed for collecting real bioluminescent data from real animal models. This is an important step in the development of the system, as the overall goal of the system is to be used in real pre-clinical studies. Further experiments looking at capturing data from multiple bioluminescent sources of different wavelengths simultaneously is a very interesting

application, which is only made possible through collecting hyperspectral data. Other improvements can be made on the software side of the system, such as optimising reconstruction algorithms to make it faster and more accurate. The graphical user interface can also be improved further to make it both more user friendly and to add any functionality that may be required, such as more adjustability in tomographic reconstruction parameters. If more time was available an accurate instrument response function would be measured that could be applied to collected data to make any measurements taken more precise.

Finally, whilst the proposed novel dual-parameter reconstruction algorithm has shown its capability in reconstructing real bioluminescent markers in real mice tumour models with good accuracy, there are a number of improvements that could be made. One improvement is to add the ability to reconstruct using a region model. In its current form the algorithm reconstructs for optical parameters by finding a global fit, however if this was able to reconstruct using regions of different optical parameters it may gain further quantitative accuracy. Another improvement is to incorporate the spectral derivative method that is currently used in BLT reconstructions into DOT reconstructions, which could further help improve quantitative accuracy of any reconstructions made. To characterise the performance of the novel algorithm a number of experiments could be carried out. An investigation into the accuracy of reconstructions for sources of different depths could be done to assess the ability of the algorithm.

The research area of BLT is a vast collective of people and groups and will only grow through the progression of quantitative accuracy and capabilities of imaging and reconstruction algorithms. This work has presented one of the first applications of a

hyperspectral BLT system based on compressive sensing and a simultaneous dual-parameter recovery algorithm in the world, which together paves the way for massive improvement in the way pre-clinical small animal studies are carried out. It is hoped that scientific advancement in the techniques presented in this work continues and assists biomedical sciences far into the foreseeable future.

LIST OF REFERENCES

1. Guggenheim, J.A., et al., *Multi-modal molecular diffuse optical tomography system for small animal imaging.* Measurement Science and Technology, 2013. **24**(10): p. 105405.

2. Klerk, C.P., et al., *Validity of bioluminescence measurements for noninvasive in vivo imaging of tumor load in small animals.* Biotechniques, 2007. **43**(S1): p. S7-S13, S30.

3. Roura, S., C. Gálvez-Montón, and A. Bayes-Genis, *Bioluminescence imaging: a shining future for cardiac regeneration.* Journal of cellular and molecular medicine, 2013. **17**(6): p. 693-703.

4. Sadikot, R.T. and T.S. Blackwell, *Bioluminescence: imaging modality for in vitro and in vivo gene expression*, in *Advanced Protocols in Oxidative Stress I*. 2008, Springer. p. 383-394.

5. McMillin, D.W., et al., *Tumor cell-specific bioluminescence platform to identify stroma-induced changes to anticancer drug activity.* Nature medicine, 2010. **16**(4): p. 483-489.

6. Choy, G., et al., *Comparison of noninvasive fluorescent and bioluminescent small animal optical imaging.* Biotechniques, 2003. **35**(5): p. 1022-1030.

7. Szentirmai, O., et al., *Noninvasive bioluminescence imaging of luciferase expressing intracranial U87 xenografts: correlation with magnetic resonance imaging determined tumor volume and longitudinal use in assessing tumor growth and antiangiogenic treatment effect.* Neurosurgery, 2006. **58**(2): p. 365-372.

8. Kemper, E., et al., *Development of luciferase tagged brain tumour models in mice for chemotherapy intervention studies.* European Journal of Cancer, 2006. **42**(18): p. 3294-3303.

9. Dehghani, H., S.C. Davis, and B.W. Pogue, *Spectrally resolved bioluminescence tomography using the reciprocity approach.* Medical physics, 2008. **35**(11): p. 4863-4871.

10. Dehghani, H., et al., *Spectrally resolved bioluminescence optical tomography.* Optics letters, 2006. **31**(3): p. 365-367.

11. Taylor, S.L., et al., *Accounting for filter bandwidth improves the quantitative accuracy of bioluminescence tomography.* Journal of biomedical optics, 2015. **20**(9): p. 096001.

12. Guggenheim, J.A., et al., *Quantitative surface radiance mapping using multiview images of light-emitting turbid media.* JOSA A, 2013. **30**(12): p. 2572-2584.

13. Dehghani, H., et al., *Quantitative bioluminescence tomography using spectral derivative data.* Biomedical optics express, 2018. **9**(9): p. 4163-4174.

14. Bruckstein, A.M., D.L. Donoho, and M. Elad, *From sparse solutions of systems of equations to sparse modeling of signals and images.* SIAM review, 2009. **51**(1): p. 34-81.

15. Berkeley, U.o.C. *The Nyquist-Shannon Sampling Theorem*. 2018; Available from: https://ptolemy.berkeley.edu/eecs20/week13/nyquistShannon.html.

16. Eldar, Y.C. and G. Kutyniok, *Compressed sensing: theory and applications*. 2012: Cambridge university press.

17. Duarte, M.F., et al., *Single-pixel imaging via compressive sampling.* IEEE signal processing magazine, 2008. **25**(2): p. 83-91.

18. Lustig, M., D. Donoho, and J.M. Pauly, *Sparse MRI: The application of compressed sensing for rapid MR imaging.* Magnetic Resonance in Medicine: An Official Journal of the International Society for Magnetic Resonance in Medicine, 2007. **58**(6): p. 1182-1195.

19. Farina, A., et al., *Multiple-view diffuse optical tomography system based on time-domain compressive measurements.* Optics letters, 2017. **42**(14): p. 2822-2825.

20. Owrangi, A.M., P.B. Greer, and C.K. Glide-Hurst, *MRI-only treatment planning: benefits and challenges.* Physics in Medicine & Biology, 2018. **63**(5): p. 05TR01.

21. Wolf, G. and N. Abolmaali, *Preclinical molecular imaging using PET and MRI.* Molecular Imaging in Oncology, 2013: p. 257-310.

22. O'farrell, A., et al., *Non-invasive molecular imaging for preclinical cancer therapeutic development.* British journal of pharmacology, 2013. **169**(4): p. 719-735.

23. Fiordelisi, M., et al., *Preclinical molecular imaging for precision medicine in breast cancer mouse models.* Contrast media & molecular imaging, 2019. **2019**.

24. Rabi, I., *The Discovery of NMR*.

25. Belliveau, J., et al., *Functional mapping of the human visual cortex by magnetic resonance imaging.* Science, 1991. **254**(5032): p. 716-719.

26. Ogawa, S., et al., *Brain magnetic resonance imaging with contrast dependent on blood oxygenation.* proceedings of the National Academy of Sciences, 1990. **87**(24): p. 9868-9872.

27. Ogawa, S., et al., *Oxygenation-sensitive contrast in magnetic resonance image of rodent brain at high magnetic fields.* Magnetic resonance in medicine, 1990. **14**(1): p. 68-78.

28. Tognarelli, J.M., et al., *Magnetic resonance spectroscopy: principles and techniques: lessons for clinicians.* Journal of clinical and experimental hepatology, 2015. **5**(4): p. 320-328.

29. Holdsworth, D.W. and M.M. Thornton, *Micro-CT in small animal and specimen imaging.* Trends in Biotechnology, 2002. **20**(8): p. S34-S39.

30. Wathen, C.A., et al., *In vivo X-ray computed tomographic imaging of soft tissue with native, intravenous, or oral contrast.* Sensors, 2013. **13**(6): p. 6957-6980.

31. Ritman, E.L., *Micro-computed tomography—current status and developments.* Annu. Rev. Biomed. Eng., 2004. **6**: p. 185-208.

32. Paulus, M.J., et al., *High resolution X-ray computed tomography: an emerging tool for small animal cancer research.* Neoplasia, 2000. **2**(1-2): p. 62-70.

33. Mukundan Jr, S., et al., *A liposomal nanoscale contrast agent for preclinical CT in mice.* American Journal of Roentgenology, 2006. **186**(2): p. 300-307.

34. Badea, C.T., et al., *Tumor imaging in small animals with a combined micro-CT/micro-DSA system using iodinated conventional and blood pool contrast agents.* Contrast media & molecular imaging, 2006. **1**(4): p. 153-164.

35. Hainfeld, J., et al., *Gold nanoparticles: a new X-ray contrast agent.* The British journal of radiology, 2006. **79**(939): p. 248-253.

36. Cai, Q.-Y., et al., *Colloidal gold nanoparticles as a blood-pool contrast agent for X-ray computed tomography in mice.* Investigative radiology, 2007. **42**(12): p. 797-806.

37. Lee, T.-Y., *Functional CT: physiological models.* Trends in biotechnology, 2002. **20**(8): p. S3-S10.

38. Rowland, D.J. and S.R. Cherry. *Small-animal preclinical nuclear medicine instrumentation and methodology*. in *Seminars in nuclear medicine*. 2008. Elsevier.

39. Chatziioannou, A.F., *Instrumentation for molecular imaging in preclinical research: Micro-PET and Micro-SPECT.* Proceedings of the american thoracic society, 2005. **2**(6): p. 533-536.

40. Fueger, B.J., et al., *Impact of animal handling on the results of 18F-FDG PET studies in mice.* Journal of Nuclear Medicine, 2006. **47**(6): p. 999-1006.

41. Judenhofer, M.S. and S.R. Cherry. *Applications for preclinical PET/MRI*. in *Seminars in nuclear medicine*. 2013. Elsevier.

42. Ferrara, K., R. Pollard, and M. Borden, *Ultrasound microbubble contrast agents: fundamentals and application to gene and drug delivery.* Annu. Rev. Biomed. Eng., 2007. **9**: p. 415-447.

43. Sirsi, S., et al., *Effect of microbubble size on fundamental mode high frequency ultrasound imaging in mice.* Ultrasound in medicine & biology, 2010. **36**(6): p. 935-948.

44. Deshpande, N., A. Needles, and J.K. Willmann, *Molecular ultrasound imaging: current status and future directions.* Clinical radiology, 2010. **65**(7): p. 567-581.

45. Foster, F.S., J. Hossack, and S.L. Adamson, *Micro-ultrasound for preclinical imaging.* Interface focus, 2011. **1**(4): p. 576-601.

46. Beard, P., *Biomedical photoacoustic imaging.* Interface focus, 2011. **1**(4): p. 602-631.

47. Ntziachristos, V., *Clinical translation of optical and optoacoustic imaging.* Philosophical Transactions of the Royal Society A: Mathematical, Physical and Engineering Sciences, 2011. **369**(1955): p. 4666-4678.

48. Treeby, B.E., E.Z. Zhang, and B.T. Cox, *Photoacoustic tomography in absorbing acoustic media using time reversal.* Inverse Problems, 2010. **26**(11): p. 115003.

49. Köstli, K.P., et al., *Temporal backward projection of optoacoustic pressure transients using Fourier transform methods.* Physics in Medicine & Biology, 2001. **46**(7): p. 1863.

50. Xu, M. and L.V. Wang, *Universal back-projection algorithm for photoacoustic computed tomography.* Physical Review E, 2005. **71**(1): p. 016706.

51. Mallidi, S., G.P. Luke, and S. Emelianov, *Photoacoustic imaging in cancer detection, diagnosis, and treatment guidance.* Trends in biotechnology, 2011. **29**(5): p. 213-221.

52. Hu, S. and L.V. Wang, *Photoacoustic imaging and characterization of the microvasculature.* Journal of biomedical optics, 2010. **15**(1): p. 011101.

53. Laufer, J.G., et al., *In vivo preclinical photoacoustic imaging of tumor vasculature development and therapy.* Journal of biomedical optics, 2012. **17**(5): p. 056016.

54. Buehler, A., et al., *Video rate optoacoustic tomography of mouse kidney perfusion.* Optics letters, 2010. **35**(14): p. 2475-2477.

55. Weber, J., P.C. Beard, and S.E. Bohndiek, *Contrast agents for molecular photoacoustic imaging.* Nature methods, 2016. **13**(8): p. 639-650.

56. Yang, X., et al., *Nanoparticles for photoacoustic imaging.* Wiley interdisciplinary reviews: nanomedicine and nanobiotechnology, 2009. **1**(4): p. 360-368.

57. Yuan, Z. and H. Jiang, *Simultaneous recovery of tissue physiological and acoustic properties and the criteria for wavelength selection in multispectral photoacoustic tomography.* Optics Letters, 2009. **34**(11): p. 1714-1716.

58. Razansky, D., et al., *Multispectral opto-acoustic tomography of deep-seated fluorescent proteins in vivo.* Nature photonics, 2009. **3**(7): p. 412-417.

59. Ma, R., et al., *Multispectral optoacoustic tomography (MSOT) scanner for whole-body small animal imaging.* Optics express, 2009. **17**(24): p. 21414-21426.

60. Laufer, J., et al., *Quantitative spatially resolved measurement of tissue chromophore concentrations using photoacoustic spectroscopy: application to the measurement of blood oxygenation and haemoglobin concentration.* Physics in Medicine & Biology, 2006. **52**(1): p. 141.

61. Guggenheim, J.A., et al., *Ultrasensitive plano-concave optical microresonators for ultrasound sensing.* Nature Photonics, 2017. **11**(11): p. 714-719.

62. Chalfie, M., *Green fluorescent protein.* Photochemistry and photobiology, 1995. **62**(4): p. 651-656.

63. Titus, J.A., et al., *Texas red, a hydrophilic, red-emitting flourophore for use with flourescein in dual parameter flow microfluorometric and fluorescence microscopic studies.* Journal of immunological methods, 1982. **50**(2): p. 193-204.

64. Mansfield, J.R., et al., *Autofluorescence removal, multiplexing, and automated analysis methods for in-vivo fluorescence imaging.* Journal of biomedical optics, 2005. **10**(4): p. 041207.

65. McCormack, E., et al., *In vivo optical imaging of acute myeloid leukemia by green fluorescent protein: time-domain autofluorescence decoupling, fluorophore quantification, and localization.* Molecular imaging, 2007. **6**(3): p. 7290.2007. 00016.

66. Wang, G., et al., *Development of the first bioluminescent CT scanner.* Radiology, 2003. **229**(566): p. 0033-8419.

67. Gu, X., et al., *Three-dimensional bioluminescence tomography with model-based reconstruction.* Optics express, 2004. **12**(17): p. 3996-4000.

68. Han, R., et al., *A source reconstruction algorithm based on adaptive hp-FEM for bioluminescence tomography.* Optics Express, 2009. **17**(17): p. 14481-14494.

69. Feng, J., et al., *Three-dimensional bioluminescence tomography based on Bayesian approach.* Optics Express, 2009. **17**(19): p. 16834-16848.

70. Ntziachristos, V., et al., *Fluorescence molecular tomography resolves protease activity in vivo.* Nature medicine, 2002. **8**(7): p. 757-761.

71. Deliolanis, N., et al., *Free-space fluorescence molecular tomography utilizing 360 geometry projections.* Optics letters, 2007. **32**(4): p. 382-384.

72. Hervé, L., et al., *Noncontact fluorescence diffuse optical tomography of heterogeneous media.* Applied optics, 2007. **46**(22): p. 4896-4906.

73. Lin, Y., et al., *Quantitative fluorescence tomography with functional and structural a priori information.* Applied optics, 2009. **48**(7): p. 1328-1336.

74. Liu, F., et al., *A parallel excitation based fluorescence molecular tomography system for whole-body simultaneous imaging of small animals.* Annals of biomedical engineering, 2010. **38**(11): p. 3440-3448.

75. Patwardhan, S.V., et al., *Time-dependent whole-body fluorescence tomography of probe bio-distributions in mice.* Optics Express, 2005. **13**(7): p. 2564-2577.

76. Klose, A.D., et al., *In vivo bioluminescence tomography with a blocking-off finite-difference method and MRI/CT coregistration.* Medical physics, 2010. **37**(1): p. 329-338.

77. Lu, Y., et al., *In vivo mouse bioluminescence tomography with radionuclide-based imaging validation.* Molecular imaging and biology, 2011. **13**(1): p. 53-58.

78. Jan, M.-L., et al., *A three-dimensional registration method for automated fusion of micro PET-CT-SPECT whole-body images.* IEEE transactions on medical imaging, 2005. **24**(7): p. 886-893.

79. Kuo, C., et al., *Three-dimensional reconstruction of in vivo bioluminescent sources based on multispectral imaging.* Journal of biomedical optics, 2007. **12**(2): p. 024007.

80. Chaudhari, A.J., et al., *Hyperspectral and multispectral bioluminescence optical tomography for small animal imaging.* Physics in Medicine & Biology, 2005. **50**(23): p. 5421.

81. Li, C., et al., *A three-dimensional multispectral fluorescence optical tomography imaging system for small animals based on a conical mirror design.* Optics express, 2009. **17**(9): p. 7571-7585.

82. Wang, G., et al., *The first bioluminescence tomography system for simultaneous acquisition of multiview and multispectral data.* International journal of biomedical imaging, 2006. **2006**.

83. Wang, G., et al., *Digital spectral separation methods and systems for bioluminescence imaging.* Optics express, 2008. **16**(3): p. 1719-1732.

84. Liu, J., et al., *In vivo quantitative bioluminescence tomography using heterogeneous and homogeneous mouse models.* Optics express, 2010. **18**(12): p. 13102-13113.

85. Alexandrakis, G., F.R. Rannou, and A.F. Chatziioannou, *Tomographic bioluminescence imaging by use of a combined optical-PET (OPET) system: a computer simulation feasibility study.* Physics in Medicine & Biology, 2005. **50**(17): p. 4225.

86. Naser, M.A. and M.S. Patterson, *Algorithms for bioluminescence tomography incorporating anatomical information and reconstruction of tissue optical properties.* Biomedical optics express, 2010. **1**(2): p. 512-526.

87. Lv, Y., et al., *Experimental study on bioluminescence tomography with multimodality fusion.* International journal of biomedical imaging, 2007. **2007**.

88. Schulz, R.B., et al., *Hybrid system for simultaneous fluorescence and x-ray computed tomography.* IEEE transactions on medical imaging, 2009. **29**(2): p. 465-473.

89. Yang, X., et al., *Combined system of fluorescence diffuse optical tomography and microcomputed tomography for small animal imaging.* Review of Scientific Instruments, 2010. **81**(5): p. 054304.

90. Kepshire, D., et al., *A microcomputed tomography guided fluorescence tomography system for small animal molecular imaging.* Review of Scientific Instruments, 2009. **80**(4): p. 043701.

91. Geng, J., *Structured-light 3D surface imaging: a tutorial.* Advances in Optics and Photonics, 2011. **3**(2): p. 128-160.

92. Basevi, H.R., et al., *Simultaneous multiple view high resolution surface geometry acquisition using structured light and mirrors.* Optics express, 2013. **21**(6): p. 7222-7239.

93. Cao, L. and J. Peter, *Bayesian reconstruction strategy of fluorescence-mediated tomography using an integrated SPECT-CT-OT system.* Physics in Medicine & Biology, 2010. **55**(9): p. 2693.

94. Prout, D., R. Silverman, and A. Chatziioannou, *Detector concept for OPET-A combined PET and optical imaging system.* IEEE transactions on nuclear science, 2004. **51**(3): p. 752-756.

95. Douraghy, A., et al., *FPGA electronics for OPET: a dual-modality optical and positron emission tomograph.* IEEE transactions on nuclear science, 2008. **55**(5): p. 2541-2545.

96. Tennstaedt, A., et al., *Noninvasive multimodal imaging of stem cell transplants in the brain using bioluminescence imaging and magnetic resonance imaging*, in *Imaging and Tracking Stem Cells*. 2013, Springer. p. 153-166.

97. Shapiro, E.M., et al., *In vivo detection of single cells by MRI.* Magnetic Resonance in Medicine: An Official Journal of the International Society for Magnetic Resonance in Medicine, 2006. **55**(2): p. 242-249.

98. Razansky, D. and V. Ntziachristos, *Hybrid photoacoustic fluorescence molecular tomography using finite-element-based inversion.* Medical physics, 2007. **34**(11): p. 4293-4301.

99. James, J., V.M. Murukeshan, and L.S. Woh, *Integrated photoacoustic, ultrasound and fluorescence platform for diagnostic medical imaging-proof of*

concept study with a tissue mimicking phantom. Biomedical optics express, 2014. **5**(7): p. 2135-2144.

100. Deng, Z., et al., *In Vivo Bioluminescence Tomography Center of Mass-Guided Conformal Irradiation.* International Journal of Radiation Oncology* Biology* Physics, 2020. **106**(3): p. 612-620.

101. Deng, Z., et al. *In vivo bioluminescence tomography-guided radiation research platform for pancreatic cancer: an initial study using subcutaneous and orthotopic pancreatic tumor models*. in *Optics and Ionizing Radiation*. 2020. International Society for Optics and Photonics.

102. Han, W., et al., *An integrated solution and analysis of bioluminescence tomography and diffuse optical tomography.* Communications in numerical methods in engineering, 2009. **25**(6): p. 639-656.

103. Zhang, Q., et al., *Quantitative bioluminescence tomography guided by diffuse optical tomography.* Optics express, 2008. **16**(3): p. 1481-1486.

104. Tan, Y. and H. Jiang, *Diffuse optical tomography guided quantitative fluorescence molecular tomography.* Applied optics, 2008. **47**(12): p. 2011-2016.

105. Pekar, J., *Multispectral bioluminescence tomography with x-ray CT spatial priors*. 2011.

106. Yan, H., et al., *A gantry-based tri-modality system for bioluminescence tomography.* Review of Scientific Instruments, 2012. **83**(4): p. 043708.

107. Gulsen, G., et al., *Combined diffuse optical tomography (DOT) and MRI system for cancer imaging in small animals.* Technology in cancer research & treatment, 2006. **5**(4): p. 351-363.

108. Lin, Y., et al., *Tumor characterization in small animals using magnetic resonance-guided dynamic contrast enhanced diffuse optical tomography.* Journal of biomedical optics, 2011. **16**(10): p. 106015.

109. Lin, Y., et al., *A photo-multiplier tube-based hybrid MRI and frequency domain fluorescence tomography system for small animal imaging.* Physics in Medicine & Biology, 2011. **56**(15): p. 4731.

110. Liu, M., et al., *In vivo pentamodal tomographic imaging for small animals.* Biomedical optics express, 2017. **8**(3): p. 1356-1371.

111. Wang, L.V. and H.-i. Wu, *Biomedical optics: principles and imaging*. 2012: John Wiley & Sons.

112. Firbank, M., *The design, calibration and usage of a solid scattering and absorbing phantom for near infra red spectroscopy*. 1994: University of London, University College London (United Kingdom).

113. Taroni, P., et al., *In vivo absorption and scattering spectroscopy of biological tissues.* Photochemical & Photobiological Sciences, 2003. **2**(2): p. 124-129.

114. Scientific, T., *The Molecular Probes Handbook: A Guide to Fluorescent Probes and Labelling Technologies*. 11 ed. Vol. 1. 2010: Life Technologies. 1076.

115. Donnert, G., C. Eggeling, and S.W. Hell, *Major signal increase in fluorescence microscopy through dark-state relaxation.* Nature methods, 2007. **4**(1): p. 81-86.

116. Cullander, C., *Imaging in the far-red with electronic light microscopy: Requirements and limitations.* Journal of microscopy, 1994. **176**(3): p. 281-286.

117. Georgakoudi, I., et al., *NAD (P) H and collagen as in vivo quantitative fluorescent biomarkers of epithelial precancerous changes.* Cancer research, 2002. **62**(3): p. 682-687.

118. Weagle, G., et al., *The nature of the chromophore responsible for naturally occurring fluorescence in mouse skin.* Journal of Photochemistry and Photobiology B: Biology, 1988. **2**(3): p. 313-320.

119. Zhao, H., et al., *Emission spectra of bioluminescent reporters and interaction with mammalian tissue determine the sensitivity of detection in vivo.* Journal of biomedical optics, 2005. **10**(4): p. 041210.

120. Prescher, J.A. and C.H. Contag, *Guided by the light: visualizing biomolecular processes in living animals with bioluminescence.* Current opinion in chemical biology, 2010. **14**(1): p. 80-89.

121. Branchini, B.R., et al., *Red-emitting luciferases for bioluminescence reporter and imaging applications.* Analytical biochemistry, 2010. **396**(2): p. 290-297.

122. Haskell, R.C., et al., *Boundary conditions for the diffusion equation in radiative transfer.* JOSA A, 1994. **11**(10): p. 2727-2741.

123. Ripoll, J., *Derivation of the scalar radiative transfer equation from energy conservation of Maxwell's equations in the far field.* JOSA A, 2011. **28**(8): p. 1765-1775.

124. Klose, A.D., V. Ntziachristos, and A.H. Hielscher, *The inverse source problem based on the radiative transfer equation in optical molecular imaging.* Journal of Computational Physics, 2005. **202**(1): p. 323-345.

125. Klose, A.D. and E.W. Larsen, *Light transport in biological tissue based on the simplified spherical harmonics equations.* Journal of Computational Physics, 2006. **220**(1): p. 441-470.

126. Wang, L. and S.L. Jacques, *Monte Carlo modeling of light transport in multi-layered tissues in standard C.* The University of Texas, MD Anderson Cancer Center, Houston, 1992: p. 4-11.

127. Ntziachristos, V., *Concurrent diffuse optical tomography, spectroscopy and magnetic resonance imaging of breast cancer*. 2000: University of Pennsylvania.

128. Fishkin, J.B., E. Gratton, and W.W. Mantulin. *Diffusion of intensity modulated near-infrared light in turbid media*. in *Time-Resolved Spectroscopy and Imaging of Tissues*. 1991. International Society for Optics and Photonics.

129. Patterson, M.S., E. Schwartz, and B.C. Wilson. *Quantitative reflectance spectrophotometry for the noninvasive measurement of photosensitizer concentration in tissue during photodynamic therapy*. in *Photodynamic Therapy: Mechanisms*. 1989. International Society for Optics and Photonics.

130. Dehghani, H., et al., *Near infrared optical tomography using NIRFAST: Algorithm for numerical model and image reconstruction.* Communications in numerical methods in engineering, 2009. **25**(6): p. 711-732.

131. Cong, W., et al. *A practical method to determine the light source distribution in bioluminescent imaging*. in *Developments in X-Ray Tomography IV*. 2004. International Society for Optics and Photonics.

132. Zacharopoulos, A.D., et al., *Three-dimensional reconstruction of shape and piecewise constant region values for optical tomography using spherical harmonic parametrization and a boundary element method.* Inverse Problems, 2006. **22**(5): p. 1509.

133. Srinivasan, S., et al., *A boundary element approach for image-guided near-infrared absorption and scatter estimation.* Medical Physics, 2007. **34**(11): p. 4545-4557.

134. Hielscher, A.H., A.D. Klose, and K.M. Hanson, *Gradient-based iterative image reconstruction scheme for time-resolved optical tomography.* IEEE Transactions on medical imaging, 1999. **18**(3): p. 262-271.

135. Schweiger, M. and S.R. Arridge, *The Toast++ software suite for forward and inverse modeling in optical tomography.* Journal of biomedical optics, 2014. **19**(4): p. 040801.

136. Arridge, S. *TOAST++ in DOT Homepage*. 2020; Available from: www.web4.cs.ucl.ac.uk/research/vis/toast/.

137. Ren, S., et al., *Molecular optical simulation environment (MOSE): a platform for the simulation of light propagation in turbid media.* PloS one, 2013. **8**(4): p. e61304.

138. Jermyn, M., et al., *Fast segmentation and high-quality three-dimensional volume mesh creation from medical images for diffuse optical tomography.* Journal of biomedical optics, 2013. **18**(8): p. 086007.

139. Dehghani, H., *NIRFAST Homepage.* 2018.

140. Dehghani, H., et al., *Numerical modelling and image reconstruction in diffuse optical tomography.* Philosophical Transactions of the Royal Society A: Mathematical, Physical and Engineering Sciences, 2009. **367**(1900): p. 3073-3093.

141. Boas, D.A., et al., *Imaging the body with diffuse optical tomography.* IEEE signal processing magazine, 2001. **18**(6): p. 57-75.

142. Pogue, B.W., et al., *Instrumentation and design of a frequency-domain diffuse optical tomography imager for breast cancer detection.* Optics express, 1997. **1**(13): p. 391-403.

143. McBride, T.O., et al., *Spectroscopic diffuse optical tomography for the quantitative assessment of hemoglobin concentration and oxygen saturation in breast tissue.* Applied optics, 1999. **38**(25): p. 5480-5490.

144. Culver, J., et al., *Three-dimensional diffuse optical tomography in the parallel plane transmission geometry: Evaluation of a hybrid frequency domain/continuous wave clinical system for breast imaging.* Medical physics, 2003. **30**(2): p. 235-247.

145. Srinivasan, S., et al., *Interpreting hemoglobin and water concentration, oxygen saturation, and scattering measured in vivo by near-infrared breast tomography.* Proceedings of the National Academy of Sciences, 2003. **100**(21): p. 12349-12354.

146. Carpenter, C.M., et al., *Image-guided optical spectroscopy provides molecular-specific information in vivo: MRI-guided spectroscopy of breast cancer hemoglobin, water, and scatterer size.* Optics letters, 2007. **32**(8): p. 933-935.

147. Boas, D.A., A.M. Dale, and M.A. Franceschini, *Diffuse optical imaging of brain activation: approaches to optimizing image sensitivity, resolution, and accuracy.* Neuroimage, 2004. **23**: p. S275-S288.

148. Culver, J.P., et al., *Volumetric diffuse optical tomography of brain activity.* Optics letters, 2003. **28**(21): p. 2061-2063.

149. Eggebrecht, A.T., et al., *A quantitative spatial comparison of high-density diffuse optical tomography and fMRI cortical mapping.* Neuroimage, 2012. **61**(4): p. 1120-1128.

150. Hebden, J.C., et al., *Imaging changes in blood volume and oxygenation in the newborn infant brain using three-dimensional optical tomography.* Physics in Medicine & Biology, 2004. **49**(7): p. 1117.

151. Hielscher, A.H., *Optical tomographic imaging of small animals.* Current opinion in biotechnology, 2005. **16**(1): p. 79-88.

152. Xu, Y., et al., *Imaging of in vitro and in vivo bones and joints with continuous-wave diffuse optical tomography.* Optics Express, 2001. **8**(7): p. 447-451.

153. Pham, T.H., et al., *Broad bandwidth frequency domain instrument for quantitative tissue optical spectroscopy.* Review of scientific instruments, 2000. **71**(6): p. 2500-2513.

154. Hielscher, A.H., et al., *Frequency-domain optical tomographic imaging of arthritic finger joints.* IEEE transactions on medical imaging, 2011. **30**(10): p. 1725-1736.

155. Hebden, J.C., et al., *Three-dimensional time-resolved optical tomography of a conical breast phantom.* Applied Optics, 2001. **40**(19): p. 3278-3287.

156. Arridge, S.R. and M. Schweiger, *A gradient-based optimisation scheme for optical tomography.* Optics Express, 1998. **2**(6): p. 213-226.

157. Levenberg, K., *A method for the solution of certain non-linear problems in least squares.* Quarterly of applied mathematics, 1944. **2**(2): p. 164-168.

158. Cheong, W.-F., S.A. Prahl, and A.J. Welch, *A review of the optical properties of biological tissues.* IEEE journal of quantum electronics, 1990. **26**(12): p. 2166-2185.

159. Penrose, R. *A generalized inverse for matrices*. in *Mathematical proceedings of the Cambridge philosophical society*. 1955. Cambridge University Press.

160. Arridge, S.R. and M. Schweiger, *Photon-measurement density functions. Part 2: Finite-element-method calculations.* Applied Optics, 1995. **34**(34): p. 8026-8037.

161. Arridge, S.R., *Optical tomography in medical imaging.* Inverse problems, 1999. **15**(2): p. R41.

162. Tikhonov, A.N., et al., *Numerical methods for the solution of ill-posed problems*. Vol. 328. 2013: Springer Science & Business Media.

163. Lu, W., D. Lighter, and I.B. Styles, *L 1-norm based nonlinear reconstruction improves quantitative accuracy of spectral diffuse optical tomography.* Biomedical optics express, 2018. **9**(4): p. 1423-1444.

164. Srinivasan, S., et al. *Validation of hemoglobin and water molar absorption spectra in near-infrared diffuse optical tomography*. in *Optical Tomography and Spectroscopy of Tissue V*. 2003. International Society for Optics and Photonics.

165. Culver, J.P., et al., *Diffuse optical tomography of cerebral blood flow, oxygenation, and metabolism in rat during focal ischemia.* Journal of cerebral blood flow & metabolism, 2003. **23**(8): p. 911-924.

166. Wilson, T. and J.W. Hastings, *Bioluminescence.* Annual review of cell and developmental biology, 1998. **14**(1): p. 197-230.

167. Wang, G., et al., *In vivo mouse studies with bioluminescence tomography.* Optics Express, 2006. **14**(17): p. 7801-7809.

168. Wang, G., Y. Li, and M. Jiang, *Uniqueness theorems in bioluminescence tomography.* Medical physics, 2004. **31**(8): p. 2289-2299.

169. Cong, A.X. and G. Wang, *Multispectral bioluminescence tomography: methodology and simulation.* International Journal of Biomedical Imaging, 2006. **2006**.

170. Chen, T., et al. *How small should pixel size be?* in *Sensors and Camera Systems for Scientific, Industrial, and Digital Photography Applications*. 2000. SPIE.

171. Holst, G.C., *CCD arrays, cameras, and displays.* 1998.

172. Davenport, M.A., et al., *Introduction to compressed sensing.* preprint, 2011. **93**(1): p. 2.

173. Baraniuk, R.G., *Compressive sensing [lecture notes].* IEEE signal processing magazine, 2007. **24**(4): p. 118-121.

174. Candès, E.J., J. Romberg, and T. Tao, *Robust uncertainty principles: Exact signal reconstruction from highly incomplete frequency information.* IEEE Transactions on information theory, 2006. **52**(2): p. 489-509.

175. Baraniuk, R., et al., *A simple proof of the restricted isometry property for random matrices.* Constructive Approximation, 2008. **28**(3): p. 253-263.

176. Baron, D., et al., *Distributed compressed sensing.* 2005.

177. Donoho, D.L., *Compressed Sensing*. 2004: Department of Statistics, Stanford University.

178. Lee, H., et al., *Efficient sparse coding algorithms.* Advances in neural information processing systems, 2006. **19**.

179. Tamir, M. *What's a good way to provide intuition as to why the lasso (L1 regularization) results in sparse weight vectors?* 2014; Available from: https://www.quora.com/What's-a-good-way-to-provide-intuition-as-to-why-the-lasso-L1-regularization-results-in-sparse-weight-vectors.

180. Rudin, L.I., S. Osher, and E. Fatemi, *Nonlinear total variation based noise removal algorithms.* Physica D: nonlinear phenomena, 1992. **60**(1-4): p. 259-268.

181. Chan, T.F. and C.-K. Wong, *Total variation blind deconvolution.* IEEE transactions on Image Processing, 1998. **7**(3): p. 370-375.

182. Boykov, Y., O. Veksler, and R. Zabih, *Fast approximate energy minimization via graph cuts.* IEEE Transactions on pattern analysis and machine intelligence, 2001. **23**(11): p. 1222-1239.

183. Geman, D. and G. Reynolds, *Constrained restoration and the recovery of discontinuities.* IEEE Transactions on pattern analysis and machine intelligence, 1992. **14**(3): p. 367-383.

184. Geman, D. and C. Yang, *Nonlinear image recovery with half-quadratic regularization.* IEEE transactions on Image Processing, 1995. **4**(7): p. 932-946.

185. Wang, Y., et al., *A new alternating minimization algorithm for total variation image reconstruction.* SIAM Journal on Imaging Sciences, 2008. **1**(3): p. 248-272.

186. Yang, J., Y. Zhang, and W. Yin, *A fast TVL1-L2 minimization algorithm for signal reconstruction from partial Fourier data*. 2008.

187. Yang, J., et al., *A fast algorithm for edge-preserving variational multichannel image restoration.* SIAM Journal on Imaging Sciences, 2009. **2**(2): p. 569-592.

188. Yang, J., Y. Zhang, and W. Yin, *An efficient TVL1 algorithm for deblurring multichannel images corrupted by impulsive noise.* SIAM Journal on Scientific Computing, 2009. **31**(4): p. 2842-2865.

189. Chambolle, A., *An algorithm for total variation minimization and applications.* Journal of Mathematical imaging and vision, 2004. **20**(1): p. 89-97.

190. Li, C., *Compressive sensing for 3D data processing tasks: applications, models and algorithms*. 2011.

191. Candes, E. and J. Romberg, *l1-magic: Recovery of sparse signals via convex programming.* URL: www. acm. caltech. edu/l1magic/downloads/l1magic. pdf, 2005. **4**: p. 14.

192. Boyd, S., et al., *Convex Optimization*. 2004: Cambridge University Press.

193. Courant, R., *Variational methods for the solution of problems of equilibrium and vibrations.* Lecture notes in pure and applied mathematics, 1994: p. 1-1.

194. Hestenes, M.R., *Multiplier and gradient methods.* Journal of optimization theory and applications, 1969. **4**(5): p. 303-320.

195. Powell, M.J., *A method for nonlinear constraints in minimization problems.* Optimization, 1969: p. 283-298.

196. Peaceman, D.W. and J. Rachford, Henry H, *The numerical solution of parabolic and elliptic differential equations.* Journal of the Society for industrial and Applied Mathematics, 1955. **3**(1): p. 28-41.

197. Barzilai, J. and J.M. Borwein, *Two-point step size gradient methods.* IMA journal of numerical analysis, 1988. **8**(1): p. 141-148.

198. Zhang, H. and W.W. Hager, *A nonmonotone line search technique and its application to unconstrained optimization.* SIAM journal on Optimization, 2004. **14**(4): p. 1043-1056.

199. Bioucas-Dias, J.M. and M.A. Figueiredo, *A new TwIST: two-step iterative shrinkage/thresholding algorithms for image restoration.* IEEE Transactions on Image processing, 2007. **16**(12): p. 2992-3004.

200. Becker, S., J. Bobin, and E.J. Candès, *NESTA: A fast and accurate first-order method for sparse recovery.* SIAM Journal on Imaging Sciences, 2011. **4**(1): p. 1-39.

201. Li, C., et al., *An efficient augmented Lagrangian method with applications to total variation minimization.* Computational Optimization and Applications, 2013. **56**(3): p. 507-530.

202. Basevi, H.R., et al., *Compressive sensing based reconstruction in bioluminescence tomography improves image resolution and robustness to noise.* Biomedical optics express, 2012. **3**(9): p. 2131-2141.

203. Figueiredo, M.A., R.D. Nowak, and S.J. Wright, *Gradient projection for sparse reconstruction: Application to compressed sensing and other inverse problems.* IEEE Journal of selected topics in signal processing, 2007. **1**(4): p. 586-597.

204. Dehghani, H., et al., *Application of spectral derivative data in visible and near-infrared spectroscopy.* Physics in Medicine & Biology, 2010. **55**(12): p. 3381.

205. Takhar, D., et al. *A new compressive imaging camera architecture using optical-domain compression*. in *Computational Imaging IV*. 2006. International Society for Optics and Photonics.

206. Sampsell, J. *An overview of the digital micromirror device (DMD) and its application to projection displays*. in *Society for Information Display International Symposium Digest of Technical Paper, 1993*. 1993.

207. Dey, N., et al., *Developing residential wireless sensor networks for ECG healthcare monitoring.* IEEE Transactions on Consumer Electronics, 2017. **63**(4): p. 442-449.

208. van Sloun, R., et al., *Compressed sensing for ultrasound computed tomography.* IEEE Transactions on Biomedical Engineering, 2015. **62**(6): p. 1660-1664.

209. Pagidipati, N.J. and T.A. Gaziano, *Estimating deaths from cardiovascular disease: a review of global methodologies of mortality measurement.* Circulation, 2013. **127**(6): p. 749-756.

210. Buzug, T.M., *Computed tomography*, in *Springer handbook of medical technology*. 2011, Springer. p. 311-342.

211. Yu, H., et al., *Compressive sensing–Based interior tomography: Preliminary clinical application.* Journal of computer assisted tomography, 2011. **35**(6): p. 762.

212. Edelman, R.R., *The history of MR imaging as seen through the pages of radiology.* Radiology, 2014. **273**(2S): p. S181-S200.

213. Ye, J.C., *Compressed sensing MRI: a review from signal processing perspective.* BMC Biomedical Engineering, 2019. **1**(1): p. 1-17.

214. Geethanath, S., et al., *Compressed sensing MRI: a review.* Critical Reviews™ in Biomedical Engineering, 2013. **41**(3).

215. Lustig, M., et al., *Compressed sensing MRI.* IEEE signal processing magazine, 2008. **25**(2): p. 72-82.

216. Buxton, R.B., *Introduction to functional magnetic resonance imaging: principles and techniques*. 2009: Cambridge university press.

217. Forman, C., et al., *Compressed sensing: a paradigm shift in MRI.* MAGNETOM Flash, 2016. **66**: p. 9-13.

218. Pruessmann, K.P., et al., *SENSE: sensitivity encoding for fast MRI.* Magnetic Resonance in Medicine: An Official Journal of the International Society for Magnetic Resonance in Medicine, 1999. **42**(5): p. 952-962.

219. Griswold, M.A., et al., *Generalized autocalibrating partially parallel acquisitions (GRAPPA).* Magnetic Resonance in Medicine: An Official Journal of the International Society for Magnetic Resonance in Medicine, 2002. **47**(6): p. 1202-1210.

220. Liu, J., et al. *Dynamic cardiac MRI reconstruction with weighted redundant Haar wavelets*. in *ISMRM*. 2012.

221. Vincenti, G., et al., *Compressed sensing single–breath-hold CMR for fast quantification of LV function, volumes, and mass.* JACC: Cardiovascular Imaging, 2014. **7**(9): p. 882-892.

222. Edgar, M.P., G.M. Gibson, and M.J. Padgett, *Principles and prospects for single-pixel imaging.* Nature photonics, 2018: p. 1.

223. Ochoa, M., et al., *Assessing patterns for compressive fluorescence lifetime imaging.* Optics letters, 2018. **43**(18): p. 4370-4373.

224. Rousset, F., et al., *Time-resolved multispectral imaging based on an adaptive single-pixel camera.* Optics express, 2018. **26**(8): p. 10550-10558.

225. Pian, Q., et al., *Compressive hyperspectral time-resolved wide-field fluorescence lifetime imaging.* Nature photonics, 2017. **11**(7): p. 411.

226. Cheraghchi, M., V. Guruswami, and A. Velingker, *Restricted isometry of Fourier matrices and list decodability of random linear codes.* SIAM Journal on Computing, 2013. **42**(5): p. 1888-1914.

227. Guggenheim, J.A., et al., *Time resolved diffuse optical spectroscopy with geometrically accurate models for bulk parameter recovery.* Biomedical optics express, 2016. **7**(9): p. 3784-3794.

228. Sloane, N.J. and M. Harwit, *Masks for Hadamard transform optics, and weighing designs.* Applied optics, 1976. **15**(1): p. 107-114.

229. Candes, E.J., *The restricted isometry property and its implications for compressed sensing.* Comptes rendus mathematique, 2008. **346**(9-10): p. 589-592.

230. Guggenheim, J.A., *Multi-modal diffuse optical tomography and bioluminescence tomography system for preclinical imaging*. 2014, University of Birmingham.

231. Taylor, S., et al. *Importance of free space modelling on quantitative non-contact imaging*. in *Biomedical Optics*. 2014. Optical Society of America.

232. Alexandrakis, G., F.R. Rannou, and A.F. Chatziioannou, *Effect of optical property estimation accuracy on tomographic bioluminescence imaging: simulation of a combined optical–PET (OPET) system.* Physics in Medicine & Biology, 2006. **51**(8): p. 2045.

233. Cong, W., et al., *Practical reconstruction method for bioluminescence tomography.* Optics Express, 2005. **13**(18): p. 6756-6771.

234. Feng, J., et al., *An optimal permissible source region strategy for multispectral bioluminescence tomography.* Optics Express, 2008. **16**(20): p. 15640-15654.

235. Allard, M., et al., *Combined magnetic resonance and bioluminescence imaging of live mice.* Journal of biomedical optics, 2007. **12**(3): p. 034018.

236. Jayet, B., S.P. Morgan, and H. Dehghani, *Incorporation of an ultrasound and model guided permissible region improves quantitative source recovery in bioluminescence tomography.* Biomedical optics express, 2018. **9**(3): p. 1360-1374.

237. Srinivasan, S., et al., *Spectrally constrained chromophore and scattering near-infrared tomography provides quantitative and robust reconstruction.* Applied optics, 2005. **44**(10): p. 1858-1869.

238. Dogdas, B., et al., *Digimouse: a 3D whole body mouse atlas from CT and cryosection data.* Physics in medicine & biology, 2007. **52**(3): p. 577.

239. Zhu, Q., et al., *A three-dimensional finite element model and image reconstruction algorithm for time-domain fluorescence imaging in highly scattering media.* Physics in Medicine & Biology, 2011. **56**(23): p. 7419.

240. James, A.G., et al., *Multi-modal molecular diffuse optical tomography system for small animal imaging.* Measurement Science and Technology, 2013. **24**(10): p. 105405.

241. Bentley, A., J.E. Rowe, and H. Dehghani, *Single pixel hyperspectral bioluminescence tomography based on compressive sensing.* Biomedical Optics Express, 2019. **10**(11): p. 5549-5564.

242. Xu, X., et al., *Quantitative Bioluminescence Tomography-guided Conformal Irradiation for Pre-clinical Radiation Research.* Int J Radiat Oncol Biol Phys, 2021.

243. Zhang, B., et al., *Bioluminescence tomography–Guided radiation therapy for preclinical research.* International Journal of Radiation Oncology* Biology* Physics, 2016. **94**(5): p. 1144-1153.

244. Bentley, A., J.E. Rowe, and H. Dehghani, *Simultaneous diffuse optical and bioluminescence tomography to account for signal attenuation to improve source localization.* Biomedical Optics Express, 2020. **11**(11): p. 6428-6444.

245. Yang, Y., et al., *Systematic calibration of an integrated x-ray and optical tomography system for preclinical radiation research.* Med Phys, 2015. **42**(4): p. 1710-20.

246. Zhang, B., et al. *Multi-projection bioluminescence tomography guided system for small animal radiation research platform (SARRP)*. in *Multimodal Biomedical Imaging XI*. 2016. International Society for Optics and Photonics.